Quantum transport in voltage-biased Josephson junctions

Baptiste Lamic

THÈSE

Pour obtenir le grade de

DOCTEUR DE L'UNIVERSITÉ GRENOBLE ALPES

École doctorale : PHYS - Physique
Spécialité : Physique Théorique
Unité de recherche : PHotonique, ELectronique et Ingéniérie QuantiqueS

Transport quantique dans des jonctions Josephson polarisées en tension

Quantum transport in voltage-biased Josephson junctions

Présentée par :

Baptiste LAMIC

Direction de thèse :

Julia MEYER PROFESSEURE DES UNIVERSITES, Université Grenoble Alpes	Directrice de thèse
Manuel HOUZET INGENIEUR HDR, Université Grenoble Alpes	Co-directeur de thèse

Rapporteurs :

MICHAEL WIMMER
Professeur associé, Delft University of Technology
CRISTINA BENA
Ingénieur HDR, CEA CENTRE DE PARIS-SACLAY

Thèse soutenue publiquement le **15 décembre 2022**, devant le jury composé de :

MICHAEL WIMMER Professeur associé, Delft University of Technology	Rapporteur
CRISTINA BENA Ingénieur HDR, CEA CENTRE DE PARIS-SACLAY	Rapporteure
MEYDI FERRIER Maître de conférences HDR, UNIVERSITE PARIS- SACLAY	Examinateur
FRANCK BALESTRO Professeur des Universités, UNIVERSITE GRENOBLE ALPES	Président
REGIS MELIN Directeur de recherche, CNRS DELEGATION ALPES	Examinateur
MARKUS HOLZMANN Directeur de recherche, CNRS DELEGATION ALPES	Examinateur

À tous ceux qui mont donnée goût aux sciences.

Abstract

This work aims to extend the comprehension of the out-of-equilibrium transport in Josephson junctions by both analytical and numerical methods. More specifically, it focuses on the Josephson radiation of a junction formed by a spin degenerate single level quantum dot connected to two superconducting leads. Such a junction hosts discrete sub-gap states whose energy depends periodically on the superconducting phase difference across the junction, they are the so-called Andreev bound states. Because of the energy dependence of the quantum dot transmission, these states are completely detached from the quasiparticle continuum and any finite detuning of the quantum dot from resonance conditions opens a second gap at the Fermi energy. The superconducting current flowing through the junction is proportional to the derivative of the junction energy with respect to the phase difference. Crucially, it depends on the Andreev bound states occupation. When a constant voltage is set across the junction, the phase difference oscillates at the Josephson frequency, which is proportional to the applied voltage. Thus, a voltage bias can induce non-adiabatic changes of the Andreev bound states occupation. To investigate the consequences of this dynamics, we proposed a stochastic model of the Andreev bound states occupation that permits to analytically evaluate the current through the junction and its fluctuations. It predicted the existence of a parameter regime where the Josephson radiation is fractional. While those results provided analytical insights into the junction behaviour, strong assumptions were required. Thus, we turned to a microscopic description that models the system as a non-interacting quantum dot hosting a unique spin degenerate level which is tunnel coupled to two BCS superconducting leads. The current is then deduced from the full Green function, which is obtained by solving the Dyson equation. We developed a novel method to solve this equation in the time domain. Its complexity is $\mathcal{O}(N\log(N))$ in both operation and memory, where the time axis has been discretized into N time steps. By contrast, the usual time domain method requires $\mathcal{O}(N^3)$ operations and $\mathcal{O}(N^2)$ bytes of memory to solve the Dyson equation. This new method is not restrained in any way to the study of Josephson junctions, it can be used to solve any Dyson equations.

Résumé

Ces travaux visent à étendre la compréhension du transport quantique hors équilibre dans des jonctions Josephson polarisées en tension, aussi bien par des méthodes analytiques que numériques. En particulier, nous avons étudié le rayonnement Josephson d'une jonction formée par une boite quantique connectée à deux fils supraconducteurs. Dans une telle jonction, les états liés d'Andreev sont toujours détachés des continuums de part et d'autre du gap supraconducteur. Tout écart de la boite quantique à la condition de résonance induit l'ouverture d'un second gap au niveau de Fermi. Sous l'effet de la tension de polarisation, des transitions non-adiabatiques peuvent avoir lieu entre ces différents états discrets. Pour comprendre l'effet de cette dynamique sur le courant et la radiation Josephson, nous proposons un modèle stochastique de celle-ci. Nous en déduisons des expressions analytiques des différentes observables paramétrisées par les probabilités de transition des processus non-adiabatiques. Ce modèle prédit l'existence d'un régime de paramètres où le rayonnement Josephson est fractionnel. Bien que ces résultats aient fourni un aperçu analytique du comportement de la jonction, il repose sur des hypothèses fortes. Notamment, tout effet de cohérence quantique est négligé, de même que l'effet de l'environnement. Nous nous sommes donc tournés vers un modèle microscopique de la jonction décrit dans le formalisme des champs hors équilibre. La boite quantique est modélisée par un unique état discret connecté par effets tunnel à deux supraconducteurs BCS. La fonction de Green complète est obtenue en résolvant l'équation de Dyson dans le domaine temporel. A cette occasion, nous avons développé une nouvelle méthode de résolution de cette équation de complexité $\mathcal{O}(N\log(N))$ en temps et en mémoire, avec N le nombre de points de discrétisation de l'axe temporel. Alors que les méthodes usuelles nécessitent $\mathcal{O}(N^3)$ opérations et $\mathcal{O}(N^2)$ octets de mémoire pour résoudre cette même équation. Ce nouvel algorithme n'est restreint en aucune façon à la simulation de jonctions Josephson.

Contents

Introduction

In recent years, several research groups have proudly announced reaching the quantum supremacy regime in both superconducting devices [1] and photonic systems [2, 3]. Other platforms, such as Rydberg atoms [4] and semiconductor qubits [5, 6], are expected to attain the same performance level in the coming years. Even if any claim of quantum supremacy must be taken with caution, these results demonstrate the excellent level in the design, fabrication, and control of coherent quantum systems enabled by modern technologies. Nowadays, some of the quantum systems have already reached the commercialization phase, one can cite for instance quantum sensors [7, 8], quantum amplifiers [9], or quantum cryptographic solutions [10, 11]. However, most of the research effort is still at the fundamental physics level. In order to deepen our understanding of novel quantum physics, one has to be able to fabricate and measure devices with a fast turnaround, which requires efficient and potent simulation tools.

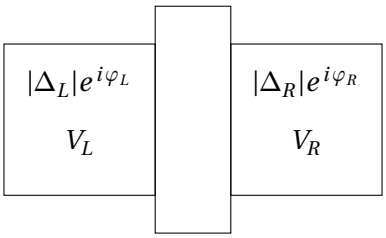

Figure I.1: Schematic of a Josephson junction. The left and right superconductors are characterized by their superconducting gap amplitude $|\Delta_{L/R}|$ and phase $\varphi_{L/R}$. $V_{L/R}$ are the left and right electric potential. They are separated by a non-superconducting barrier.

When we focus on solid state devices, the most ubiquitous component is certainly the Josephson junction, which is formed by two superconducting leads connected by a non-superconducting element, which is called the weak link, see fig. I.1. The core of their phenomenology is captured by the Josephson relations [12]

$$I(\varphi) = \frac{2e}{\hbar}\frac{\mathrm{d}E_J(\varphi)}{\mathrm{d}\varphi}, \qquad \frac{\mathrm{d}\varphi}{\mathrm{d}t} = \frac{2eV}{\hbar} \tag{1}$$

where $\varphi = \varphi_L - \varphi_R$ is the phase difference across the junction, $E_J(\varphi)$ is the junction energy, $V = V_L - V_R$ is the voltage bias, e the elementary charge and $\hbar$ the reduced Planck constant. This junction forms the building block of superconducting quantum processors, magnetic field sensors, or quantum limited amplifiers. Despite their common use, they are still subject of fundamental research explorations.

In the simplest form of Josephson junctions, the weak link is a piece of metal or insulator of length L, we refer to this device as a superconductor-normal-superconductor (SNS) junction. As the excitations within the energy gap are trapped in the weak link, the junctions host discrete states known as the Andreev bound states (ABSs). Their number per conduction channel depends on the length of the weak link

compared to its the coherence length $\xi = \hbar v_F/\pi|\Delta|$ [13], where v_F is the Fermi velocity in the weak link and $2|\Delta|$ is the size of the superconducting gap. In the short junction limit, $L \ll \xi$, each channel hosts only two particle symmetric ABSs of energy $E_\pm(\varphi)$, see fig. I.2, given by

$$\frac{E_\pm}{|\Delta|} = \pm\sqrt{1 - T\sin\left(\varphi/2\right)}, \tag{2}$$

where T is the transmission probability of the weak-link at the Fermi energy E_F. The junction energy is the sum of the contribution of each ABS, such that

$$E_J(\varphi) = n_+ E_+(\varphi) + n_- E_-(\varphi), \tag{3}$$

where $n_\pm \in \{0,1\}$ are the state occupations. Thus, the current flowing though the junction depend on this occupation. At low temperature $T \ll \Delta$ and thermal equilibrium, only the state E_- is occupied, thus the DC Josephon current is

$$I_J(\varphi) = \frac{2e}{\hbar}\frac{\mathrm{d}E_-(\varphi)}{\mathrm{d}\varphi}. \tag{4}$$

By applying a constant voltage bias V across the junction, the superconducting phase difference φ will oscillate at the Josephson frequency $\omega_J = 2eV/\hbar$, which in turn can induce a Landau-Zener transition at $\varphi = 0$ with a probability

$$p_\pi = \exp\left(-\frac{\pi\Delta}{eV}(1-T)\right). \tag{5}$$

Because of this non-adiabatic process, the state occupations are time dependant. Yet, in SNS junctions, the ABSs are in contact with the continuum of states at $\varphi = 0 \mod 2\pi$, see fig. I.2, meaning that the junction energy is forced to be 2π-periodic in the phase difference. It results in an oscillation of the current at the Josephson frequency ω_J, the corresponding electromagnetic signal is the Josephson radiation [14].

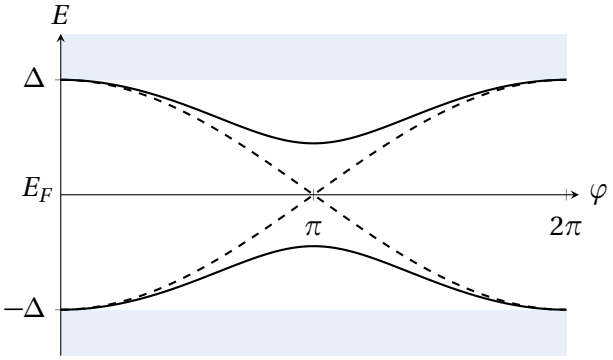

Figure I.2: Spectrum of a short SNS junction. *Solid lines:* ABS spectrum of a junction of transmission probability $T = 0.8$. *Dashed lines:* ABS spectrum of a perfectly transmiting junction ($T = 1$). The light blue rectangles are the continuum outside the superconducting gap. In presence of backscattering, the ABSs anti-cross at the Fermi energy. At thermal equilibrium, only the states below the Fermi energy are occupied.

More recently, the Josephson radiation spectrum of a junction composed of topological superconductors has drawn much attention. A topological superconductor is a superconductor whose wave function cannot be continuously deformed into a combination of atomic ones. In particular, Majorana bound states are expected to form at the extremity of spinless p-wave superconductor [15]. When forming a Josephson junction using such superconducting leads, the Majorana end modes hybridize to form ABS which energy is 4π-periodic in the superconducting phase difference. An experimental signature of such a periodicity would be a fractional Josephson radiation, that is a Josephson radiation at frequency $\omega_J/2$ [16–19].

Yet, other kind of junctions may display a non-conventional Josephson radiation. Let's consider a junction made of a spin-degenerate single-level quantum dot (QD) that is contacted to two superconducting leads. Its Andreev spectrum has been analysed both in the presence and absence of Coulomb interaction [20–22].

In particular, in presence of a strong Coulomb interaction, and when the QD has a non-zero spin, a many-body state forms at the Fermi energy, this is the Kondo effect. Its associate energy scale is the Kondo temperature T_K, [22, 23]. This pinned state enhances the device transmission at the Fermi energy. In the strong Kondo regime $|\Delta| \ll T_K$, as well as in the absence of interactions when the QD level witdth Γ induced by the coupling to the leads is large compared to superconducting gap $|\Delta| \ll \Gamma$, the junction accommodates two particle-hole symmetric ABSs denoted $|+\rangle$ and $|-\rangle$, [24]. Their energies are

$$E_{\pm}(\varphi) = \pm\,|\Delta|\sqrt{T_0\cos^2(\varphi/2) + R_\pi \sin^2(\varphi/2)}, \tag{6}$$

where $R_\pi \equiv 1 - T_\pi$ is the reflection probability of the device in the normal state at the Fermi energy and T_0 is an effective transmission probability. Introducing the partial level widths $\Gamma_{L/R}$ due to the coupling to the left and right leads, and ϵ_0 the position of dot level, we can write

$$T_\pi = \frac{\Gamma_L\Gamma_R}{((\Gamma_L+\Gamma_R)/2)^2 + \epsilon_0^2}. \tag{7}$$

Thus, when the junction is not symmetric $\Gamma_L \neq \Gamma_R$, or the QD level not at the Fermi energy, the ABSs are anti-crossing at the Fermi energy. $R_0 \equiv 1 - T_0$ is of order $(\Delta/T_K)^2 \ll 1$ in the Kondo regime and $(\Delta/\Gamma)^2 \ll 1$ in absence of interactions. As the ABSs are detached from the continuum, see fig. I.3, the energies $E(\varphi)$ of these junctions are not constrained to be 2π-periodic in the phase difference any more. Hence, the time-dependent phase shift can cause a complex dynamics of the ABSs occupation by inducing non-adiabatic processes. This may result in a change of the Josephson radiation frequency. That is why it is of prime interest to understand the out-of-equilibrium dynamics of conventional junctions to assess the use of fractional Josephson radiations as a probe of topological superconductivity.

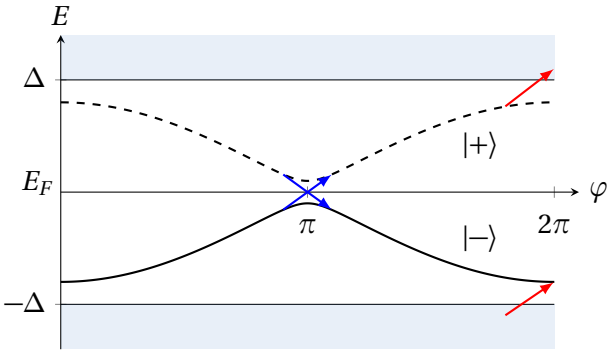

Figure I.3: Spectrum of a slightly dissymmetric S-QD-S junction. The Andreev bound states are fully detached from the continuum. In the presence of a voltage bias, the phase increases with time and non-adiabatic transitions may occur between states $|+\rangle$ and $|-\rangle$ (blues arrows),as well as between state $|+\rangle$ and the continuum at energy $E > \Delta$ or between the continuum at energy $E < -\Delta$ and state $|-\rangle$ (red arrows).

This thesis aims to improve the comprehension of the out-of-equilibrium transport in superconducting junctions by both analytical and numerical methods. We first develop a stochastic model to describe the out-of-equilibrium ABS occupation dynamics in junctions where the ABSs are fully detached from the continuum. This model provides analytical formulas of the DC current and radiation spectrum parametrized by the transition probabilities p_0 and p_π. p_0 is the probability for a non-adiabatic transition between the state $|+\rangle$ and the continuum states with energy $E > |\Delta|$ as well as continuum states of energy $E < -|\Delta|$ with the state $|-\rangle$. Similar model already had some success in the description of both

conventional and topological junctions [25–27]. Yet, they do not reproduce the oscillation in the junction response to an applied voltage caused by interferences between successive non-adiabatic processes [19, 24], and the transition rates still have to be determined from the underlying microscopic model. Plus, there is no clear direction to include the effects of the environment, such as the presence of an electromagnetic cavity around the junction. Thus, we eventually turn to the direct simulation of the microscopic quantum model.

As an open quantum system, the junction can be elegantly analysed in the out-of-equilibrium quantum field formalism [28, 29]. Interestingly, both the non-interacting system and the one in the strong Kondo regime can be described by a non-interacting field theory upon renormalizing the system parameters. The latter case being similar to the description of a metal as a non-interacting gas of electrons through the Fermi liquid theory [23]. Thus, all the system observables can be deduced from the two-point correlation functions, also known as the Green function G

$$G_{p,q}(t,t') \equiv -i \left\langle \mathbf{T_C} \Phi_p(t) \Phi_q^\dagger(t') \right\rangle, \tag{8}$$

where $\Phi_q^\dagger(t')$ creates a particle in state q at time t' and $\Phi_p(t)$ destroys a particle in state p at time t. Within the out-of-equilibrium field theory, these time indices lay on an oriented complex contour. The *complex time ordering* symbol $\mathbf{T_C}$ organizes the operators in front of him according to their positions on this contour. Finally, $\langle\rangle$ is the averaging operator. To evaluate this quantity, we first compute the Green function of the isolated dot $g(t,t')$, the effect of the coupling to the leads is then described by a self-energy term Σ. The full Green function G is therefore the solution of the Dyson equation

$$G(t,t') = g(t,t') + \iint g(t,t_1)\Sigma(t_1,t_2)G(t_2,t')\,\mathrm{d}t_1\,\mathrm{d}t_2. \tag{9}$$

Solving this equation requires an apparently disproportionate amount of computational resources. This triggered our effort to design a new method to solve the general out-of-equilibrium Dyson equation. Usual time domain methods require $\mathcal{O}(N^3)$ operations and $\mathcal{O}(N^2)$ bytes of memory, where N is the number of time steps. In consequence, long-time simulations used to be prohibitively expensive. Yet, by using modern numerical methods adapted to the structure of the Dyson equation and by extending the work of [30], we propose a new algorithm that reaches a complexity of $\mathcal{O}(N\log(N))$ in both time and space.

The manuscript is structured as follows. The chapter 1 and chapter 2 introduce the formalism used in this work, the BCS theory of superconductors and the properties of the usual short Josephson junctions. The chapter 3 exposes a stochastic model of the ABS dynamics in S-QD-S junction biased by a constant voltage. It predicts the existence of a parameter regime where the Josephson radiation is fractional. To validate this first approach, we turned to a microscopic description of the junction in chapter 4. It models the junction as a non-interacting quantum dot which hosts a unique spin degenerate level that interacts through tunnel coupling with two BCS superconducting leads. This model does not explicitly include many-body interactions, even if it may hold for certain interacting systems by using renormalized parameters [24]. Thus, any observable can be deduced from the full Green function which is obtained by solving the Dyson equation in the time domain. The last part of this manuscript addresses thus the numerical resolution of the Dyson equation. The chapter 5 reviews the usual existing algorithms and their limitations. Finally, in the chapter 6 we propose a new algorithm that solves the general out-of-equilibrium Dyson equation in quasi-linear time and space. We conclude this manuscript with some suggestions to extend this work.

CHAPTER 1

Out-of-equilibrium field theory

"Begin at the beginning", the King said gravely, "and go on till you come to the end: then stop."

— Lewis Carroll, *Alice in Wonderland*

The quantum field formalism permits to gracefully deal with open quantum systems, or design approximation methods for interacting problems. In condensed matter physics, this picture is equivalent to the Hamiltonian formulation. The formal connection between these complementary descriptions is done in numerous textbooks [28, 29, 31]. Here we introduce the essential features of the out-of-equilibrium field theory, while disregarding most of the technical aspects. As in classical statistical physics, the central objects of the field theory are the *generating functions*, that are usually called *partition functions*. They compactly represent all the system properties. But, they are generally impossible to evaluate in a closed form. Thus, one has to resort to some approximation strategies.

Generating function *A sequence of numbers a_p can be interpreted as the coefficients of a formal series development of a function $f(x)$. f is said to be the* generating function *of the sequence a_p.*

For instance, the sequence of numbers $1/n!$ can be represented as the coefficients of a power series expansion of $\exp(x)$.

Partition function *In equilibrium statistical physics and field theory all the properties of a system are encoded in its generating function $Z[J_1, J_2, ...]$ which is called the* partition function *or* partition functional.

A functional is a map from a function space to scalars. Thus, when the J_k appearing in the expression $Z[J_1, J_2, ...]$ are functions, we shall call Z the partition *functional*. As an example, let's write the partition function of a classical system that can exchange energy and particles with a thermostat at temperature T

$$Z = \sum_r \exp\left(\frac{\mu N_r - E_r}{k_B T}\right), \tag{1.1}$$

where the sum runs over all the possible configurations of the system, μ is the chemical potential, E_r is configuration energy and N_r is the number of particles. T is the temperature and k_B the Boltzmann constant. The probability to occupy a given state is

$$P(r) = \frac{1}{Z} \exp\left(\frac{\mu N_r - E_r}{k_B T} \right). \tag{1.2}$$

Thus, the average number of particles can be expressed by differentiating Z

$$k_B T \frac{\partial Z}{\partial \mu} = \sum_r \frac{N_r}{Z} \exp\left(\frac{\mu N_r - E_r}{k_B T} \right), \tag{1.3}$$

$$= \langle N \rangle . \tag{1.4}$$

We may access the statistical properties of other observables by inserting fictitious source terms in Z. To compute the average values of an observable $\hat{X}$, one rewrites Z as

$$Z[J_X] = \sum_r \exp\left(\frac{\mu N_r - E_r}{k_B T} + x_r J_X \right), \tag{1.5}$$

where x_r is the value of $\hat{X}$ in the configuration r. Thus, by taking the log-derivative with respect to J_X and setting the source to zero we get

$$\left. \frac{\partial Z}{\partial J_X} \right|_{J_X=0} = \sum_r \frac{x_r}{Z} \exp\left(\frac{\mu N_r - E_r}{k_B T} \right), \tag{1.6}$$

$$= \langle X \rangle . \tag{1.7}$$

The quantum field formalism also expresses the partition functions as a sum on all the system configurations. But in general, the configuration of a continuous system is a field, that is a function. For instance the states of an electron are set by its wavefunction $\psi(\mathbf{r})$. Thus, the sum over the configurations is actually an integration over a function space. The rigorous mathematical construction of this integral is not for the faint-hearted, and raised numerous mathematical difficulties. But we are blessed, these technical issues can generally be overlooked in physical applications. The general partition function of a system defines by the action $S[\bar{\psi}, \psi]$ is

$$Z = \int \mathscr{D}[\bar{\psi}, \psi] e^{\frac{i}{\hbar} S[\bar{\psi}, \psi]}, \tag{1.8}$$

where $\int \mathscr{D}[\bar{\psi}, \psi]$ designates the integration over the configurations space. We insist that in general ψ is not a number nor a vector but a function. To follow the customs, when looking at out-of-equilibrium systems we shall name this object *the generating functional* rather than the partition function, see [28]. The first aim of the present section is to introduce the definitions and concepts that permits to understand and use this equation to study open quantum system. The second objective is to introduce the Keldysh formalism allowing the description of general out-of-equilibrium dynamics.

1.1 Density matrix

Hereafter, we are dealing with systems in an environment. Therefore, their states are not pure wave functions. They are rather statistical mixtures of quantum states. To fully understand the difference, we first consider an observable $\hat{O}$ and a quantum state $|\psi\rangle$ defined as

$$|\psi\rangle = \sum_k a_k |k\rangle , \tag{1.9}$$

where $|k\rangle$ is a basis of the Hilbert space and the coefficients a_k are complex numbers. The expectation value of the observable $\hat{O}$ for the state $\left|\psi\right\rangle$ is written as

$$\left\langle \hat{O} \right\rangle_{|\psi\rangle} \equiv \left\langle \psi \middle| \hat{O} \middle| \psi \right\rangle, \tag{1.10}$$

$$= \sum_{p,q} \bar{a}_p a_q \left\langle p \middle| \hat{O} \middle| q \right\rangle. \tag{1.11}$$

Now let's look at what happens when we consider a statical mixture of the states $|k\rangle$. Let P_k be the probability for the system to be in the state k. Owing to the usual expression of an average, the expectation of O is

$$\left\langle \hat{O} \right\rangle_P = \sum_k P_k \left\langle k \right| \hat{O} \left| k \right\rangle. \tag{1.12}$$

Hence, to describe statistical mixture, we need to introduce a new object: *the density matrix*.

Density matrix *A statistical mixture of quantum states is described by its* density matrix. *For a set of quantum states $\left|\psi_k\right\rangle$ distributed according to the probabilities p_k, the density matrix ρ is defined by*

$$\rho \equiv \sum_k p_k \left|\psi_k\right\rangle\left\langle\psi_k\right|. \tag{1.13}$$

The average value of an observable O is thus provided by

$$\boxed{\langle O \rangle_\rho = \mathrm{Tr}(\rho O).} \tag{1.14}$$

To demonstrate this result, we simply expand the trace over an orthonormal basis $|k\rangle$

$$\mathrm{Tr}(\rho O) = \sum_k \sum_l p_l \left\langle k \middle| \psi_l \right\rangle \left\langle \psi_l \middle| O \middle| k \right\rangle \tag{1.15}$$

$$= \sum_l p_l \left\langle \psi_l \middle| O \middle| \psi_l \right\rangle. \tag{1.16}$$

One may show that the density matrix dynamics follows the Von Neumann equation [28]

$$i\hbar \frac{\mathrm{d}\rho(t)}{\mathrm{d}t} = \big[H(t), \rho(t)\big], \tag{1.17}$$

where H is the Hamiltonian describing the system. In the following section, we formally solved the Von Neumann equation using the Picard iteration method. This transformation then allows the partition function to be written as a field integral.

1.2 Evolution operator

As the Schrödinger equation and by extension the von Neumann equation are linear, the time evolution of the system is described by a linear-operator.

Evolution operator *For a system whose state at every moment is fully characterized by a vector $y(t)$ that undergoes a linear dynamics, the* evolution operator $U(t,t')$ *is the linear map such that*

$$y(t) = U(t,t')y(t'). \tag{1.18}$$

From its definition, it's trivial to demonstrate that an evolution operator verifies the semigroup property

$$U(t,t_1)U(t_1,t')=U(t,t'). \tag{1.19}$$

When the dynamics is described by a linear time-independent differential equation of the form

$$\frac{\mathrm{d}y(t)}{\mathrm{d}t}=Ay(t), \tag{1.20}$$

where A is a matrix. The general solution is $y(t)=e^{A(t-t_0)}y(t_0)$. Thus, we deduce that the evolution operator is

$$U(t,t')=e^{A(t-t')}. \tag{1.21}$$

But we are interested in the out-of-equilibrium regime, and thus our differential equation will be time-dependent. Hence, we shall consider the case:

$$\frac{\mathrm{d}y(t)}{\mathrm{d}t}=A(t)y(t). \tag{1.22}$$

By using Picard iterations we can build a formal representation of the corresponding evolution operator. The idea of Picard iteration is to write

$$\begin{aligned}
y(t) &= y(t_0)+\int_{t_0}^{t} y'(t)\mathrm{d}t && (1.23)\\
&= y(t_0)+\int_{t_0}^{t} A(t_1)y(t_1)\mathrm{d}t_1 && (1.24)\\
&= y(t_0)+\int_{t'}^{t} A(t_1)\left(\int_{t_0}^{t_1} A(t_2)y(t_2)\mathrm{d}t_2+y(t_0)\right)\mathrm{d}t_1 && (1.25)\\
&= y(t_0)+\int_{t'}^{t} A(t_1)y(t_0)\mathrm{d}t_1+\int_{t_0}^{t}\int_{t_0}^{t_1} A(t_1)A(t_2)y(t_2)\mathrm{d}t_2\mathrm{d}t_1. && (1.26)
\end{aligned}$$

Continuing the iterations, we get that, for $t\geq t_0$,

$$y(t)=\lim_{n\to\infty}\sum_{k=0}^{n}\int\!\!\cdots\!\!\int_{t_k\geq\ldots\geq t_0} A(t_k)A(t_{k-1})\cdots A(t_1)y(t_0)\mathrm{d}t_k\mathrm{d}t_{k-1}\cdots\mathrm{d}t_1. \tag{1.27}$$

As $A(t_k)$ has no reason to commute, the product orders are important. Thus it is customary to introduce the *time ordering* **T** and anti-time ordering $\tilde{\mathbf{T}}$ symbols.

Time-ordering and antitime-ordering symbols *Considering a set of time dependant operators* $\{A_k(t_k)\}_k$ *we define the* time ordering symbol **T** *and* the anti-time ordering symbol $\tilde{\mathbf{T}}$ *by their actions on the operator products*

$$\begin{aligned}
\mathbf{T}\{A_1(t_1)A_2(t_2)\cdots A_n(t_n)\} &= \sum_{\sigma}\epsilon(\sigma)\left(\prod_{j=1}^{n-1}\Theta(t_{\sigma_k}-t_{\sigma_{k+1}})\right)A_{\sigma_1(t_{\sigma_1})}A_{\sigma_2(t_{\sigma_2})}\cdots A_{\sigma_n(t_{\sigma_n})}, && (1.28)\\
\tilde{\mathbf{T}}\{A_1(t_1)A_2(t_2)\cdots A_n(t_n)\} &= \sum_{\sigma}\epsilon(\sigma)\left(\prod_{j=1}^{n-1}\Theta(t_{\sigma_{k+1}}-t_{\sigma_k})\right)A_{\sigma_1(t_{\sigma_1})}A_{\sigma_2(t_{\sigma_2})}\cdots A_{\sigma_n(t_{\sigma_n})}, && (1.29)
\end{aligned}$$

where the sum runs on all the permutations of length n and $\epsilon(\sigma)$ *account for the symmetry under exchange of the operators acting at different points in time, see below, and* Θ *is the Heaviside function.*

Put in simple words, the time ordering $\mathbf{T}$ rearranges a product to ensure that the operators appear in ascending time order from right to left and $\tilde{\mathbf{T}}$ organizes them in decreasing time order from right to left. The statistic factor $\epsilon(\sigma)$ permits to preserve the relevant symmetries under exchange of operators acting at different moments in time:

$$\epsilon \equiv \begin{cases} 1 & \text{for bosonic operators} \\ \text{sign of the permutation} & \text{for fermionic operators} \end{cases} \tag{1.30}$$

Bosonic and fermionic operators *The bosonic or fermionic nature of a set of operators $\{A_k(t_k)\}_k$ does not refer to the physical objects they describe, but uniquely to their properties under exchange. Products of bosonic operators acting at the same moment in time commute, while fermionic operators anticommute:*

$$\textit{For bosonic operators: } \forall (k,k'),\ t_k = t_{k'} \implies A_k(t_k)A_{k'}(t_{k'}) = A_{k'}(t_{k'})A_k(t_k) \tag{1.31}$$

$$\textit{For fermionic operators: } \forall (k,k'),\ t_k = t_{k'} \implies A_k(t_k)A_{k'}(t_{k'}) = -A_{k'}(t_{k'})A_k(t_k) \tag{1.32}$$

A product of fermionic creation operators can thus be a bosonic operator. In particular the full Hamiltonian is a bosonic operator. Let's get back to the expression of the evolution operator, inserting a time ordering symbol, we get

$$\int\!\!\cdots\!\!\int_{t_k \geq \ldots \geq t_0} A(t_k)\cdots A(t_1)y(t_0)\,\mathrm{d}t_k\cdots\mathrm{d}t_1 = \frac{1}{n!}\mathbf{T}\int_{t_0}^{t}\int_{t_0}^{t}\cdots\int_{t_0}^{t}\prod_{j=1}^{k}A(t_j)y(t_0). \tag{1.33}$$

Thus, the evolution operator can be written as

$$U(t,t') = \sum_{k=0}^{\infty}\frac{1}{n!}\mathbf{T}\int_{t_0}^{t}\int_{t_0}^{t_1}\cdots\int_{t'}^{t_n}\prod_{k=1}^{n}A(t_k). \tag{1.34}$$

The above expression is formally recast into

$$U(t,t') = \mathbf{T}\exp\left\{\int_{t'}^{t}A(t_1)\,\mathrm{d}t_1\right\}. \tag{1.35}$$

The Schrödinger equation 1.36 describes the evolution of an isolated quantum system. It is a linear differential equation

$$\boxed{H\left|\psi\right\rangle = i\hbar\frac{\mathrm{d}}{\mathrm{d}t}\left|\phi\right\rangle.} \tag{1.36}$$

We may write the associated evolution operator as

$$\boxed{\text{For } t \geq t',\ U(t,t') = \mathbf{T}\exp\left\{-\frac{i}{\hbar}\int_{t'}^{t}H(t_1)\,\mathrm{d}t_1\right\}.} \tag{1.37}$$

As $U(t,t')$ must preserve the norm of the wave vector, it is a unitary matrix : $U^{-1}(t,t') = U^{\dagger}(t,t')$. By applying its semigroup property, we have

$$U(t',t)U(t,t') = \mathbb{1}. \tag{1.38}$$

Thus,

$$U^\dagger(t,t') = U(t',t). \tag{1.39}$$

And $U^\dagger(t,t')$ can be expressed using the *reverse time ordering* $\tilde{\mathbf{T}}$ as

$$\boxed{\text{For } t \geq t',\ U^\dagger(t,t') = \tilde{\mathbf{T}} \exp\left\{ \frac{i}{\hbar} \int_{t'}^{t} H(t_1)\,\mathrm{d}t_1 \right\}.} \tag{1.40}$$

Or said otherwise

$$\boxed{\text{For } t \leq t',\ U(t,t') = \tilde{\mathbf{T}} \exp\left\{ -\frac{i}{\hbar} \int_{t'}^{t} H(t_1)\,\mathrm{d}t_1 \right\}.} \tag{1.41}$$

From the definition of the density matrix, we immediately deduce that

$$\rho(t) = U(t,t')\rho(t')U^\dagger(t,t'). \tag{1.42}$$

Thus, the expectation value of an observable $\hat{O}$ at time t can be expressed knowing the evolution operator and the density matrix at time t' as

$$\begin{aligned} \left\langle \hat{O} \right\rangle(t) &= \mathrm{Tr}\left\{ U(t,t')\rho(t')U^\dagger(t,t')\hat{O} \right\}, & (1.43)\\ &= \mathrm{Tr}\left\{ U(t,t')\rho(t')U(t',t)\hat{O} \right\}. & (1.44) \end{aligned}$$

To have a more elegant formula, we use the invariance of the trace under cyclic permutations

$$\left\langle \hat{O} \right\rangle(t) = \mathrm{Tr}\left\{ U(t',t)\hat{O}U(t,t')\rho(t') \right\}. \tag{1.45}$$

Hence, it is possible to evaluate the expectation value of an operator at time t, while only knowing the density matrix only at time t'. To do this, one first evaluates the operator $U(t',t)\hat{O}U(t,t')$ which describes a forward evolution in time from t' to t followed by the effect of the operator O and finally a backward evolution in time from t to t'. Thus, if one can approximate the density matrix at time t' and the evolution operator $U(t,t')$, one can access the operator statistics. It turns out that this strategy is often more efficient than the direct evaluation of the density matrix [28, 29]. When studying systems at the thermal equilibrium, it is possible to avoid the backward evolution, and its technical issues [28]. Unfortunately, we are interested in the out-of-equilibrium regime. Therefore, we introduce a closed time loop which allows distinguishing a time $\overrightarrow{t}$ associated with a forward evolution and another time $\overleftarrow{t}$ associated with a backward evolution.

1.3 Closed time contour

To paraphrase [28], we need to free time from the time axis, so that it is possible to define a closed time contour often call the *Keldysh contour*. While one may explicitly consider a loop in the complex plane, we will not fall for it, as we just need to extend times t with a contour index $\pm$. So that a time on the Keldysh contour is designated by its projection on the time axis, *i.e.* its *real time*, and by its direction. The points on the Keldysh contour are ordered by their position on the contour. Points of the forward branch C^+ are set earlier than those on the backward branch C^-. The points on the forward branch are time ordered, while those of the backward branch are anti-time ordered. We then introduce the evolution operator U_C on this contour. It evolves a state vector following the contour direction. Thus, for $t < t'$ the operator $U_C(t,t')$ has to do a partial revolution around the contour. Introducing the *Keldysh time ordering symbol* $\mathbf{T_C}$ one may show that the contour evolution operator has the following expression [28]

$$U_C(t,t') = \mathbf{T_C} \exp\left\{ -\frac{i}{\hbar} \int_{t'}^{t} H(t_1)\,\mathrm{d}t_1 \right\}. \tag{1.46}$$

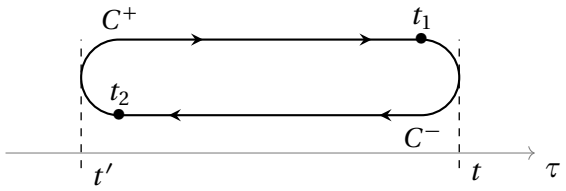

Figure 1.1: Representation of the Keldysh contour between times t' and t. By construction times laying on the forward branch C^+ are set before times laying on the backward branch C^-, thus $t_2 > t_1$.

The eq. (1.45) is almost unchanged

$$\left\langle \hat{O} \right\rangle(t) = \mathrm{Tr}\left\{ U_C(t',t)\hat{O}U_C(t,t')\rho(t') \right\}. \tag{1.47}$$

We stretch the Keldysh contour from $-\infty$ to ∞. The time t at which we evaluate the expectation of

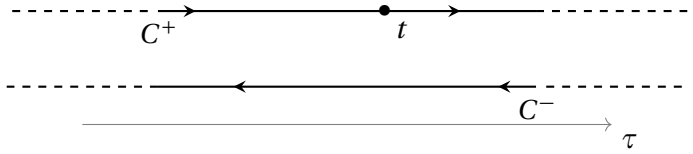

Figure 1.2: The Keldysh contour is stretched to overlap the whole real line.

an observable now resides either on the forward branch or on the backward branch. In both case, its expression is :

$$\left\langle \hat{O} \right\rangle(t) = \mathrm{Tr}\left\{ U_C(-\infty,t)\hat{O}U_C(t,-\infty)\rho(-\infty) \right\}. \tag{1.48}$$

Finally, a first expression of the partition function is

$$\boxed{Z = \mathrm{Tr}\, U_C(-\infty^-,-\infty^+)\rho(-\infty)} \tag{1.49}$$

Where $U_C(-\infty^-,-\infty^+)$ has to be understood as an evolution around the full Keldysh contour starting at $-\infty$ on the forward branch and stopping at $-\infty$ on the backward branch. By construction $U_C(-\infty,-\infty) = \mathbb{1}$ as the backward evolution compensates exactly the forward evolution, and thus $Z = 1$. Yet, we can add to the Hamiltonian H a perturbation $\hat{O}\delta(t - t_{\hat{O}})\eta$ where $t_{\hat{O}}$ is on the contour. Now, the backward evolution does not exactly compensate the forward evolution. The partition function can be differentiated with respect to the source term η, thereby we recover the expectation value of $\hat{O}$.

$$i\hbar \left.\frac{\partial Z[\eta]}{\partial \eta}\right|_{\eta=0} = \left\langle \hat{O} \right\rangle(t_{\hat{O}}). \tag{1.50}$$

Constructing the field integral for fermionic particles requires introducing the anti-commutative algebra of the Grassmann variables.

1.4 Grassmann variables

The anti-commutativity of fermionic operators imposes to build an anti-commutating and associative algebra known as a Grassmann algebra. Its elements are the Grassmann numbers or variables. It is induced by a set of generators θ_i that satisfies

$$\boxed{\{\theta_i, \theta_j\} = 0} \tag{1.51}$$

where the bracket $\{,\}$ is the anti-commutator. The set of all the non-zero products $\{\theta_\alpha, \theta_\beta, \ldots, \theta_\alpha\theta_\beta, \theta_\beta\theta_\alpha, \ldots\}$ of generators form a base of this space. Hereafter, we will always consider an even number of generators. Thus, we can arbitrarily group them in pairs. Elements of pairs are said to be conjugate to each other. This permits to define the conjugation operator $\eta \to \bar{\eta}$ that associates to a Grassmann variable its conjugate. This operation is distributive over the sum and satisfies the following properties

$$\overline{\eta_\alpha, \ldots \eta_\beta} = \bar{\eta}_\beta, \ldots \bar{\eta}_\alpha \tag{1.52a}$$

$$\overline{c\,\eta} = \bar{c}\,\bar{\eta} \quad \text{with} \quad c \in \mathbb{C} \tag{1.52b}$$

$$\bar{\bar{\eta}} = \eta \tag{1.52c}$$

The anti-commutation relation imposes that for any Grassmann number η we have $\eta^2 = 0$. Thus, the most general one variable polynomial function is

$$f(\eta) = a_0 + a_1\eta, \tag{1.53}$$

and the more general bivariate polynomial is

$$f(\eta, \bar{\eta}) = a_0 + a_1\eta + a_2\bar{\eta} + a_3\eta\bar{\eta}, \tag{1.54}$$

with a_k some complex numbers. In particular, we have

$$e^{\eta+\bar{\eta}} = 1 + \eta + \bar{\eta}, \tag{1.55}$$

where the exponential is defined from its Taylor series. The field integral formalism requires the definition of integration and differentiation of Grassmann functions.

Berezin integrals

The Berezin integrals define an integration over Grassmann numbers suitable for quantum field formalism. It is the linear operation that is defined by

$$\int 1\,\mathrm{d}\eta \equiv 0 \tag{1.56}$$

$$\int \eta\,\mathrm{d}\eta \equiv 1 \tag{1.57}$$

To uniquely define the integration when several variables appear, we need to add the following rules: *before performing the integration the integrated variable is moved to the left of the integrand.* Thus, we have:

$$\int \eta\bar{\eta}\,\mathrm{d}\bar{\eta} = -\eta \tag{1.58}$$

The differentiation with a respect to a Grassmann number is identical to integration:

$$\frac{\partial}{\partial\eta} \equiv \int \mathrm{d}\eta \tag{1.59}$$

We shall notice that the Berezin integral is invariant by translation of the integrand. This concludes the presentation of Grassmann algebra, we now turn to the construction of the *coherent states*.

1.5 Coherent states

The coherent states are defined as the eigenvectors of the destruction operator a. They satisfy :

$$a\,|\alpha\rangle = \alpha\,|\alpha\rangle \tag{1.60}$$

Which implies that:

$$\langle\alpha|\,a^\dagger = \bar{\alpha}\,\langle\alpha| \tag{1.61}$$

1.5.1 Coherent bosonic state

For a bosonic state associate to the creation and destruction operators $a^\dagger$ and a, the coherent states are the eigenvector of a. Considering a state $|\alpha\rangle$ defined as

$$|\alpha\rangle = \sum_{n=0}^{\infty} a_n |n\rangle, \tag{1.62}$$

we have

$$a|\alpha\rangle = \sum_{n=1}^{\infty} a_n \sqrt{n} |n-1\rangle. \tag{1.63}$$

Hence, if $\alpha|\alpha\rangle = a|\alpha\rangle$ for some complex α, we deduce that:

$$\alpha a_n = \sqrt{n+1} a_{n+1}, \tag{1.64}$$

solving this recurrence, we got

$$a_n = \frac{\alpha}{\sqrt{n!}}. \tag{1.65}$$

We finally deduce the form of the bosonic coherent states

$$|\alpha\rangle \propto \sum_n \frac{\alpha^n a^\dagger}{\sqrt{n!}} |n\rangle \tag{1.66}$$

$$= \lambda e^{\alpha a^\dagger} |0\rangle. \tag{1.67}$$

Where λ is a normalization constant that we fix by imposing $\langle\alpha|\alpha\rangle = 1$, finally:

$$\boxed{|\alpha\rangle = e^{-\frac{\bar{\alpha}\alpha}{2} + \alpha a^\dagger} |0\rangle} \tag{1.68}$$

1.5.2 Coherent fermionic states

When constructing the coherent fermionic states associated to the destruction operator a, the relation $a|\eta\rangle = \eta|\eta\rangle$ must hold. Yet, as $a^2 = 0$, we have the constraint:

$$\eta^2 = 0 \tag{1.69}$$

Thus, the only eigenvalue in $\mathbb{C}$ is 0. More useful states can be formed by considering eigenvalues in the set of Grassmann numbers. They automatically fulfil eq. (1.69). Decomposing the wave vector as $|\eta\rangle = \alpha_0|0\rangle + \alpha_1|1\rangle$, with α_i in the set of Grassmann numbers, we deduce from the eigenvector equation that

$$\eta(\alpha_0|0\rangle + \alpha_1|1\rangle) = \alpha_1|0\rangle, \tag{1.70}$$

and as for the bosonic coherent state, we supplement this first equation with the normalization condition:

$$\langle\eta|\eta\rangle = 1 \tag{1.71}$$

We finally deduce that :

$$|\eta\rangle = \left(1 - \frac{\bar{\eta}\eta}{2}\right)|0\rangle + \eta|1\rangle \tag{1.72}$$

This last expression can be recast in the same form as the bosonic coherent state:

$$\boxed{|\eta\rangle = e^{-\frac{\bar{\eta}\eta}{2} + \eta a^\dagger} |0\rangle} \tag{1.73}$$

1.5.3 Properties of coherent states

The coherent states will be used to parametrize the field configuration. This is possible as they form a complete set [31], *id est*

$$\mathbb{1} = \int_\alpha |\alpha\rangle \langle\alpha|, \tag{1.74}$$

where in the bosonic case, the above relation holds for the measure on $\mathbb{C}$ define by

$$\int_{\alpha\in\mathbb{C}} f(\alpha) \equiv \iint f(x+iy)\frac{dx\,dy}{\pi}. \tag{1.75}$$

Yet, they are not orthogonal

$$\langle\alpha|\beta\rangle = e^{\bar\alpha\beta - \frac{1}{2}\left(\bar\alpha\alpha+\bar\beta\beta\right)}, \tag{1.76}$$

The trace of an operator $\hat O$ can be expressed as:

$$\mathrm{Tr}\,\hat O = \int_\alpha \langle\alpha|\,\hat O\,|\alpha\rangle \tag{1.77}$$

But the essential property of the coherent states comes directly from their definition as eigenvectors of destruction operators. For any product of a and $a^\dagger$ in *normal order* we have

$$\boxed{\forall (p,q)\in\mathbb{N}^2 : \quad \langle\alpha|\left(a^\dagger\right)^p a^q |\beta\rangle = \bar\alpha^p \beta^q \langle\alpha|\beta\rangle} \tag{1.78}$$

Normal order *A product of creation and destruction operators is* normal ordered *when all the creation operators appear on the left of the destruction operators.*

Thus if we consider a second quantization Hamiltonian $\hat H$ written in normal order. It is a multivariate polynomial in the creation and destruction operators. Let's denote this formal polynomial as

$$H\left[\bar X_k, X_k\right] = \sum_k h_k \bar X_k X_k, \tag{1.79}$$

so that $H\left[a_k^\dagger, a_k\right] = H$. By use of eq. (1.78) we have the following correspondence between Hamiltonians, and more generally any operators written in normal order, and coherent states

$$\bigotimes_l \langle\alpha_l|\,\hat H\,|\beta_l\rangle = H\left[\bar\alpha_l, \beta_l\right]\langle\alpha|\beta\rangle, \tag{1.80}$$

where the tensor product run over all the creation operator indices. This correspondence between operators and coherent state coupled with eq. (1.74) will permit to build the field integral.

1.6 Field integral

We consider a system governed by the normal-ordered second quantization Hamiltonian $H(t)$, with t living on the Keldysh contour, which extends from t_0 to t_f. We discretize the Keldysh contour on $2N$ segments $[t_{k-1}, t_k]_{k=1,\dots,2N}$ of algebraic length Δt_k:

$$\Delta t_k \equiv t_k - t_{k-1} \tag{1.81}$$

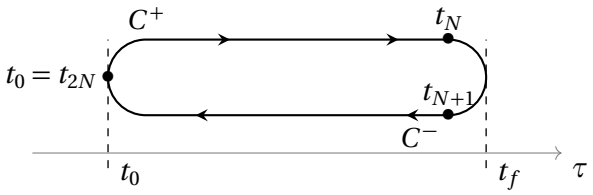

That is, Δt_k is negative on the backward branch. Thus, we can decompose the evolution operator on the contour as follows

$$U_C(t_i, t_f) = \prod_{k=1}^{2N} U_C(t_k, t_{k-1}), \tag{1.82}$$

and insert between each evolution the resolution of identity

$$\int_{\Phi(t_k)} |\Phi(t_k)\rangle \langle\Phi(t_k)| = \mathbb{1}, \tag{1.83}$$

where $|\Phi(t_k)\rangle$ is the tensor product of the coherent states associated to each destruction operator at time t_k

$$|\Phi(t_k)\rangle = \bigotimes_l |\alpha_l(t_k)\rangle, \tag{1.84}$$

Thus, we got:

$$U_C(t_{2N}, t_0) = \int\cdots\int_{\Phi(t_1),\ldots,\Phi(t_{2N-1})} U_C(t_{2N}, t_{2N-1}) |\Phi(t_{2N-1})\rangle \prod_{k=2}^{2N-1} \left\{\langle\Phi(t_k)| U_C(t_k, t_{k-1}) \left|\Phi^\dagger(t_{k-1})\right\rangle\right\} \langle\Phi(t_1)| U_C(t_1, t_0) \tag{1.85}$$

By developing the evolution operator to the first order in the time increment, we got:

$$U_C(t_k, t_{k-1}) \approx \exp\left(1 - \frac{i\Delta t_k}{\hbar} \hat{H}(t_{k-1}) + \mathcal{O}\left(\Delta t_k^2\right)\right) \tag{1.86}$$

Combining this last equation with eq. (1.80) we have

$$\begin{aligned}
\langle\Phi(t_k)| U_C(t_k, t_{k-1}) |\Phi(t_{k-1})\rangle &\approx e^{1 - \frac{i\Delta t_k}{\hbar} H(t_{k-1}, \Phi^\dagger(t_k), \Phi(t_{k-1})) + \mathcal{O}\left(\Delta t_k^2\right)} \langle\Phi(t_k)|\Phi(t_{k-1})\rangle & (1.87)\\
&\approx e^{-\frac{i\Delta t_k}{\hbar} H(t_{k-1}, \Phi^\dagger(t_k), \Phi(t_{k-1}))} e^{\Phi^\dagger(t_k)\Phi(t_{k-1}) - \frac{1}{2}\left(\Phi^\dagger(t_k)\Phi(t_k) + \Phi(t_{k-1})\Phi(t_{k-1})\right)} & (1.88)\\
&\approx e^{-\frac{i\Delta t_k}{\hbar} H(t_{k-1}, \Phi^\dagger(t_k), \Phi(t_{k-1})) + \frac{1}{2}\left\{\left(\Phi^\dagger(t_k) - \Phi^\dagger(t_{k-1})\right)\Phi(t_{k-1}) - \Phi^\dagger(t_k)\left(\Phi(t_k) - \Phi(t_{k-1})\right)\right\}} & (1.89)
\end{aligned}$$

Thus, defining the discretized action as

$$S\left[\Phi^\dagger(t_k), \Phi(t_k)\right] = \sum_k \frac{\hbar}{2i} \left\{\left(\Phi^\dagger(t_k) - \Phi^\dagger(t_{k-1})\right)\Phi(t_{k-1}) - \Phi^\dagger(t_k)\left(\Phi(t_k) - \Phi(t_{k-1})\right)\right\} - \Delta t_k H(t_{k-1}, \Phi^\dagger(t_k), \Phi(t_{k-1})), \tag{1.90}$$

We can rewrite the evolution operator as

$$U_C(t_{2N}, t_0) \underset{\Delta t_k \to 0}{=} \int\cdots\int_{\Phi(t_1),\ldots,\Phi(t_{2N-1})} e^{\frac{i}{\hbar} S\left[\Phi^\dagger(t_k), \Phi(t_k)\right]} \tag{1.91}$$

To finally form the correlation function, we have to introduce the initial density matrix, and the trace.

$$Z \underset{\Delta t_k \to 0}{=} \mathrm{Tr} \int\cdots\int_{\Phi(t_1),\ldots,\Phi(t_{2N-1})} e^{\frac{i}{\hbar} S\left[\Phi^\dagger(t_k), \Phi(t_k)\right]} \rho(t_0) \tag{1.92}$$

By adding another resolution of the identity in front of the density matrix, and taking the trace by use of eq. (1.77), we have

$$Z \underset{\substack{\Delta t_k \to 0 \\ \Phi(t_0),\ldots,\Phi(t_{2N})}}{=} \int\!\cdots\!\int \langle \Phi(t_{2N})| \, e^{\frac{i}{\hbar} S\left[\Phi^\dagger(t_k),\Phi(t_k)\right]} |\Phi(t_0)\rangle \langle \Phi(t_0)| \, \rho(t_0) |\Phi(t_{2N})\rangle \,. \tag{1.93}$$

We are getting close to the expected result. The last step is to take the continuum limit. Therefore, we introduce the differential operator ∂_t defined by

$$\partial_t \Phi \equiv \lim_{\Delta t \to \infty} \frac{\Phi(t) - \Phi(t - \delta t)}{\delta t}. \tag{1.94}$$

This operator is equivalent to usual derivatives for complex valued functions. Finally, we extend the definition of the Hamiltonian to the Keldysh contour by

$$H(t^\pm) \equiv \pm H(t), \tag{1.95}$$

with t^+, t^- designing times on the forward, respectively backward, branch. With these definitions at hand, we write a first form of the continuous action

$$S[\Phi^\dagger, \Phi] = \int_C \frac{\hbar}{2i} \left(\partial_t \Phi^\dagger(t) \Phi(t) - \Phi^\dagger(t) \partial_t \Phi(t) \right) - H(t, \Phi^\dagger(t), \Phi(t)) \, \mathrm{d}t. \tag{1.96}$$

Where $\int_C$ is the integration over the Keldysh contour. With this first form of the action, the partition function is *almost* in its final form

$$Z = \int \mathscr{D}[\Phi^\dagger, \Phi] \left\langle \Phi(t_f) \right| e^{\frac{i}{\hbar} S[\Phi^\dagger, \Phi]} |\Phi(t_0)\rangle \langle \Phi(t_0)| \, \rho(t_0) \left| \Phi(t_f) \right\rangle, \tag{1.97}$$

where the integration measure $\int \mathscr{D}[\Phi^\dagger, \Phi]$ is defined as

$$\int \mathscr{D}[\Phi^\dagger, \Phi] = \lim_{N \to \infty} \int\!\cdots\!\int_{\Phi(t_0),\ldots,\Phi(t_{2N})} . \tag{1.98}$$

To derive the usual expression of the partition function in the field formalism, we shall include the initial correlations described by $\rho(t_0)$ in the definition of the action. To do so, we write the new action as $S = S_0 + S_{\text{int}}$. Where S_0 is a quadratic form and includes the initial correlations. This corresponds to a splitting of the Hamiltonian into $H_0 + H_{\text{int}}$ with the unique constraint that H_0 should be quadratic in the creation and destruction operators, id est it can be recast into

$$H_0(t) = \sum_{p,q} h_{p,q} a_p^\dagger a_q + \bar{h}_{p,q} a_q^\dagger a_p, \tag{1.99}$$

where the $h_{p,q}$ are complex numbers. Such a Hamiltonian H_0 is said to be non-interacting as each term $a_p^\dagger a_q$ can be interpreted as the propagation from the mode q to the mode p. The quadratic part of the action can be written as

$$S_0[\Phi^\dagger, \Phi] = \int_c \Phi^\dagger(t) g^{-1}(t) \Phi(t) \mathrm{d}t., \tag{1.100}$$

where g^{-1} is for the moment the kernel of the quadratic form. Thus, S_{int} is deduced from H_{int} by the following relation.

$$S_{\text{int}} = -\int_C H_{\text{int}}(t, \Phi^\dagger(t), \Phi(t)) \, \mathrm{d}t, \tag{1.101}$$

With this new definition of the action, we finally have

$$\boxed{Z = \int \mathscr{D}[\Phi^\dagger, \Phi] e^{\frac{i}{\hbar} S[\Phi^\dagger, \Phi]}.} \tag{1.102}$$

In the following section we shall identify g^{-1} with the inverse of the one particle correlation function, also known as *Green function*, associates to the problem define by H_0 and the initial density matrix $\rho(t_0)$.

1.7 Green functions

Let's consider a quadratic Hamiltonian H defined as

$$H(t)=\sum_{p,q} h_{p,q}a_p^\dagger a_q + \bar{h}_{p,q}a_q^\dagger a_p. \tag{1.103}$$

The corresponding partition function augmented by two sources terms $\bar{\eta}$ and η is

$$Z_0[\eta^\dagger,\eta]=\int \mathscr{D}[\Phi^\dagger,\Phi]e^{\frac{i}{\hbar}\int_C \Phi^\dagger(t)g^{-1}(t)\Phi(t)+\eta(t)^\dagger\Phi(t)+\Phi(t)^\dagger\eta(t)\,\mathrm{d}t} \tag{1.104}$$

Considering the results from section 1.2, one may show the following relation

$$\left.\frac{\delta Z_0}{\delta\eta_q(t')\delta\eta_p^\dagger(t)}\right|_{\eta,\eta^\dagger=0} = \frac{-1}{\hbar^2}\left\langle \mathbf{T_C}\Phi_p(t)\Phi_q^\dagger(t')\right\rangle, \tag{1.105}$$

where $\Phi(t)$ denotes both the field configuration and the destruction operator acting at time t, in the same manner $\Phi^\dagger(t)$ stands for the operator creating a particle at time t and the conjugate field configuration. Using the same notation for both object should not bring any difficulties, as they appear in very different contexts. When the action is quadratic, as here, the relations for Gaussian integral in appendix A permit to carry out the integration. One obtain

$$Z_0[\eta^\dagger,\eta]=\det\left(g^{-1}/i\hbar\right)^{\pm 1}\, e^{\frac{-i}{\hbar^2}\iint_C \eta^\dagger(t_1)g(t_1,t_2)\eta(t_2)\mathrm{d}t_1\mathrm{d}t_2} \tag{1.106}$$

where $g(t,t')$ is solution of $g\cdot g^{-1}=\hbar$, thus we absorb a $\hbar$ in the definition of g. The determinant of a functional linear operator is the limit of the determinants of the discretized operators and the sign $+$ and $-$ are respectively for fermionic and bosonic fields. As we are working on the Keldysh contour we still have the normalization condition $Z[0,0]=1$. Hence, the above relation simplifies to

$$Z_0[\eta^\dagger,\eta]=e^{\frac{-i}{\hbar^2}\iint_C \eta^\dagger(t_1)g(t_1,t_2)\eta(t_2)\mathrm{d}t_1\mathrm{d}t_2} \tag{1.107}$$

Finally taking the functional derivative of the above relation, we have

$$\boxed{g_{p,q}(t,t')=-i\left\langle \mathbf{T_C}\Phi_p(t)\Phi_q^\dagger(t')\right\rangle} \tag{1.108}$$

This function g is the contour ordered one particle Green function. The name of this correlation function come from its properties for non-interacting systems. From eq. (1.108) and the properties of the density matrix, one can show [28] that the inverse of the free Green function g^{-1} is

$$\boxed{g^{-1}(\mathbf{r},t)=\left(i\hbar\frac{\partial}{\partial t}-h(\nabla_\mathbf{r},\mathbf{r},t)\right)} \tag{1.109}$$

Where $h(\nabla_\mathbf{r},\mathbf{r},t)$ is the local Hamiltonian. Thus, the contour ordered Green function of a non-interacting system g satisfies

$$\boxed{g^{-1}(\mathbf{r},t)g\left(\mathbf{r},t,\mathbf{r}',t'\right)=\hbar\delta\left(\mathbf{r}-\mathbf{r}'\right)\delta\left(t-t'\right)} \tag{1.110}$$

Thus, g is a Green function as defined in applied mathematics textbooks, see [32], where Green functions are usually defined as follows. Considering a linear equation of the form:

$$\mathscr{L}\,y(\mathbf{r},t)=0 \tag{1.111}$$

Where $\mathscr{L}$ is a linear operator defining the problem and $y(\mathbf{r})$ is the unknown. The associated Green function is a *distribution* $G(\mathbf{r},t,\mathbf{r}',t')$ that solves the equation

$$\mathscr{L}G\left(\mathbf{r},t,\mathbf{r}',t'\right)=\delta\left(\mathbf{r}-\mathbf{r}'\right)\delta\left(t-t'\right) \tag{1.112}$$

The Green functions describe how an excitation propagates through time and space. In particular, once the Green functions are known, the non-homogeneous equation

$$\mathscr{L}y(\mathbf{r},t)=f(\mathbf{r},t), \tag{1.113}$$

is formally solved by

$$y(\mathbf{r},t)=\int G\left(\mathbf{r},t,\mathbf{r}',t'\right)f\left(\mathbf{r}',t'\right)\mathrm{d}\mathbf{r}'\mathrm{d}\mathbf{t}'. \tag{1.114}$$

One may think of the Green functions as operators acting on elements of the Hilbert space. Thus, we naturally introduce algebra operations that extend those on finite dimensional matrices.

1.7.1 Integral operator algebra

Here, we will not discuss the involved topic of linear operators on infinite or even continuous space, but simply introduce some notations useful in the following. In general, the operators we meet can be expressed as linear integral operators. That is, the action of a linear map $\mathscr{A}$ on a vector $f_q(t,\mathbf{r})$ is expressed as

$$\mathscr{A}(f_q(t,\mathbf{r}))\equiv\sum_k\iint\mathrm{d}\mathbf{r}'\mathrm{d}t'A_{p,k}(t,\mathbf{r},t',\mathbf{r}')f_k(t',\mathbf{r}'), \tag{1.115}$$

where $A_{p,k}(t,\mathbf{r},t',\mathbf{r}')$ is the integral kernel of the map $\mathscr{A}$. It is similar to the description of a finite dimensional linear map by a matrix, and following this similarity, we introduce the product of kernel as follows. For two kernels $A_{p,q}(t,\mathbf{r},t',\mathbf{r}')$ and $B_{p,q}(t,\mathbf{r},t',\mathbf{r}')$, we define their product as

$$(AB)_{p,q}(t,\mathbf{r},t',\mathbf{r}')\equiv\sum_k\iint\mathrm{d}\mathbf{r_1}\mathrm{d}t_1A_{p,k}(t,\mathbf{r},t_1,\mathbf{r_1})B_{k,q}(t_1,\mathbf{r}_1,t',\mathbf{r}'), \tag{1.116}$$

The transposition A^T of a kernel is defined as

$$A^T_{p,q}(t,\mathbf{r},t',\mathbf{r}')\equiv A_{q,p}(t',\mathbf{r}',t,\mathbf{r}). \tag{1.117}$$

Its hermitian conjugate is defined in the same way

$$A^\dagger_{p,q}(t,\mathbf{r},t',\mathbf{r}')\equiv\bar{A}_{q,p}(t',\mathbf{r}',t,\mathbf{r}). \tag{1.118}$$

We say that an operator is local in time, or instantaneous, when its kernel has the form

$$A_{p,k}(t,\mathbf{r};t',\mathbf{r}')=A_{p,k}(t,\mathbf{r},\mathbf{r}')\delta(t-t'). \tag{1.119}$$

A kernel $A_{p,k}(t,\mathbf{r};t',\mathbf{r}')$ is said to be stationary when it can be written as

$$A_{p,k}(t,\mathbf{r};t',\mathbf{r}')=A_{p,k}(t-t',\mathbf{r};\mathbf{r}') \tag{1.120}$$

With these conventions at hand, we can introduce the whole family of Green functions that appears in out-of-equilibrium quantum field theory.

1.7.2 Usual Green functions

Field theory generalizes the definition of Green functions to all the correlation functions [28, 29] such as the following *two-particles* Green functions

$$G_{4,3,2,1}(t_4,x_4;t_3,x_3;t_2,x_2;t_1,x_1)=\left\langle \psi_4(t_4,x_4)\psi_3(t_3,x_3)\psi_2^\dagger(t_2,x_2)\psi_1^\dagger(t_1,x_1)\right\rangle. \tag{1.121}$$

We will mainly be interested in the *one-particle* Green functions, that is the ones that are formed by a unique product of creation and destruction operators. The time ordered G_T and the anti-time ordered $G_{\tilde{T}}$ Green function are defined as

$$G_T(x,t,x',t')\equiv -i\left\langle \mathbf{T}\big(\psi(t,x)\psi^\dagger(t',x')\big)\right\rangle, \tag{1.122a}$$
$$G_{\tilde{T}}(x,t,x',t')\equiv -i\left\langle \tilde{\mathbf{T}}\big(\psi(t,x)\psi^\dagger(t',x')\big)\right\rangle. \tag{1.122b}$$

The lesser $G^<(x,t,x',t')$ and greater $G^>(x,t,x',t')$ Green functions are defined as

$$G^<(x,t,x',t')\equiv \mp i\left\langle \psi^\dagger(t',x')\psi(t,x)\right\rangle, \tag{1.123a}$$
$$G^>(x,t,x',t')\equiv -i\left\langle \psi(t,x)\psi^\dagger(t',x')\right\rangle, \tag{1.123b}$$

where the upper sign is for bosons, and the lower one for fermions. In non interacting systems, they solve the following equations

$$g^{-1}(\mathbf{r},t)g^<\big(\mathbf{r},t,\mathbf{r}',t'\big) = 0 \tag{1.124a}$$
$$g^{-1}(\mathbf{r},t)g^>\big(\mathbf{r},t,\mathbf{r}',t'\big) = 0 \tag{1.124b}$$

Some Green functions are defined as combinations of the previous ones. Such as the retarded G^R and advanced G^A Green functions

$$G^R(x,t,x',t')\equiv \theta(t-t')\big(G^>(x,t,x',t')-G^<(x,t,x',t')\big) \tag{1.125a}$$
$$G^A(x,t,x',t')\equiv -\theta(t'-t)\big(G^>(x,t,x',t')+G^<(x,t,x',t')\big) \tag{1.125b}$$

Retarded and advanced Green function are related by

$$G^A=\big(G^R\big)^\dagger \tag{1.126}$$

Finally, the Keldysh Green function is defined as

$$G^K\equiv\big(G^>(x,t,x',t')+G^<(x,t,x',t')\big) \tag{1.127}$$

1.7.3 Thermal equilibrium Green function

In thermal equilibrium, the Green functions are stationary. Thus, they are naturally represented in the energy domain

$$G(t) = \int_{-\infty}^{\infty}\frac{dE}{2\pi\hbar}G(E)e^{-\frac{iEt}{\hbar}} \tag{1.128}$$
$$G(E) = \int_{-\infty}^{\infty}\mathrm{d}tG(t)e^{\frac{itE}{\hbar}} \tag{1.129}$$

We can deduce all the Green functions from the retarded component [28], in particular the kinetic Green function of a fermionic system satisfies

$$G^K(E)\underset{\text{fermion}}{=}\Big(G^R(E)-G^{R^\dagger}(E)\Big)\tanh\left(\frac{E}{2k_BT}\right). \tag{1.130}$$

While for bosons its verifies

$$G^K(E) \underset{\text{boson}}{=} \Big(G^R(E) - G^{R^\dagger}(E)\Big)\coth\Big(\frac{E}{2k_BT}\Big). \tag{1.131}$$

The retarded and advanced Green functions of a system describes by a quadratic Hamiltonian H whose modes are $|\lambda\rangle$ with energies ϵ_λ reads

$$g^R(E) \underset{0<\eta\ll 1}{=} \sum_\lambda \frac{|\lambda\rangle\langle\lambda|}{E+i\eta-\epsilon_\lambda}, \tag{1.132a}$$

$$g^A(E) \underset{0<\eta\ll 1}{=} \sum_\lambda \frac{|\lambda\rangle\langle\lambda|}{E-i\eta-\epsilon_\lambda}, \tag{1.132b}$$

where $\eta/\hbar$ is an infinitesimal relaxation rate that ensures the proper definition of the Fourier transform. In latter chapters, these expressions will be our starting point to evaluate the free Green functions. Before closing this chapter, we shall introduce the real-time formulation of the out-of-equilibrium quantum field formalism.

1.8 Real time representation

When leaving the abstract description of the out-of-equilibrium theory to study specific problems, the manipulation of time indices laying on a closed contour is rather annoying. Thus, we supplement the field configurations by a Keldysh index : $\Phi \to \Phi^\pm$. So that, $\Phi^+(t)$ and $\Phi^-(t)$ are the forward and backward branch configurations at *real time* t. The partition function takes the form

$$Z = \int \mathscr{D}[\Phi^{+^\dagger},\Phi^+,\Phi^{-^\dagger},\Phi^-]e^{\frac{i}{\hbar}S[\Phi^{+^\dagger},\Phi^+,\Phi^{-^\dagger},\Phi^-]} \tag{1.133}$$

The integration measure $\mathscr{D}[\Phi^{+^\dagger},\Phi^+,\Phi^{-^\dagger},\Phi^-]$ accounts for the proper constraint on the forward and backward fields. Thereafter, we will not keep explicit the numerous fields $\mathscr{D}[\Phi^{+^\dagger},\Phi^+,\Phi^{-^\dagger},\Phi^-] \to \mathscr{D}[\Phi^\dagger,\Phi]$. The correlation functions are also equipped with a set of Keldysh indices. Hence, the real-time representation $\hat{G}$ of the contour ordered Green function has a matrix structure in the *Keldysh space*

$$G \to \hat{G} \equiv \begin{pmatrix} G^{++} & G^{+-} \\ G^{-+} & G^{--} \end{pmatrix} \tag{1.134}$$

The blocks of the real time Green function $G^{\pm\pm}$ can be identified with previously defined Green functions

$$\begin{pmatrix} G^{++} & G^{+-} \\ G^{-+} & G^{--} \end{pmatrix} = \begin{pmatrix} G & G^< \\ G^> & \tilde{G} \end{pmatrix} \tag{1.135}$$

A rotation in the Keldysh space permit to cancel redundant information and provide a more meaningful representation. Considering the matrix

$$L = \frac{1}{\sqrt{2}}\big(1 - i\tau_y\big), \tag{1.136}$$

where τ_y is the second Pauli matrix acting on the Keldysh indices.

$$\tau_2 = \begin{pmatrix} 0 & -i \\ i & 0 \end{pmatrix} \tag{1.137}$$

The field configurations ϕ are transformed according to

$$\begin{pmatrix} \phi_q \\ \phi_c \end{pmatrix} = L \begin{pmatrix} \phi_+ \\ \phi_- \end{pmatrix}, \tag{1.138}$$

where ϕ_q and ϕ_c are called quantum and classical fields as the first vanishes in the classical regime [29]. Upon performing the rotation described by L, we obtain a more efficient representation G_S of $\hat{G}$

$$G_S \equiv L\hat{G}L^\dagger \tag{1.139}$$

As G_S is symmetric for real bosonic field [28], it is sometime called the *symmetric representation*, despite G_S is *not* symmetric in general.

$$G_S = \begin{pmatrix} 0 & G^A \\ G^R & G^K \end{pmatrix}. \tag{1.140}$$

The kinetic Green function contains the description of the state occupations, while the retarded and advanced Green functions describe the spectrum of the system and the propagations of excitations. Whether we are considering the representation of the Green function on the real time axis, or its real-time representation, we shall simply denote it by g or G.

Conclusion

In this chapter we have introduced the essential aspect of the out-of-equilibrium field theory. Yet, we did not provide any method to study interacting or open systems. Field theory approach to open systems will be introduced in chapter 4. The next chapter illustrates the mean-field approximation by deriving the BCS theory of superconductors.

CHAPTER 2

Superconducting devices

A superconducting material is characterized by the absence of current dissipation in DC up to a critical current I_C, and by the repulsion of all magnetic fields below the critical field H_C. These properties usually appear at low temperatures. The critical temperature T_C separates the superconducting phase at temperatures below T_C from the normal phase. This phenomenon was discovered in 1911 by H. Kamerlingh Onnes and colleagues at Leiden [33] while measuring the resistivity of mercury cooled by liquid Helium. The initial purpose of this experiment was to develop a thermometer for cryogenic temperatures. While phenomenological models had some success, such as the *London equations* and the *Ginzburg-Landau theory* [13], we had to wait 1956 for the first successful microscopic description of superconductivity by John Bardeen, Leon Neil Cooper and John Robert Schrieffer. The *BCS* theory [34], named after its authors, properly describes the so-called conventional superconductors. By contrast, superconducting materials that do not follow the BCS theory such as high T_C cuprate superconductors are tagged as *unconventional*. In 1962, Josephson published an article where he accurately evaluated the non-dissipative current that flows through a junction formed by an insulator connected to two superconducting leads. He also predicted that when a constant voltage bias V is applied, this current shall oscillate at the pulsation $\omega_J = \frac{2eV}{\hbar}$. The existence of these currents is now known as the DC and AC Josephson effects.

2.1 BCS theory of superconductors

The BCS theory describes how an effective attraction between electrons mediated by phonons induces the collapse of the Fermi sea at low temperature. Here we derive the classical BCS results in the field theory formalism. We recast into the real-time framework the derivations proposed by [29, 35].

2.1.1 A BCS type hamiltonian

We consider an effective Hamiltonian of the form

$$H = H_0 + \gamma \int c_\uparrow^\dagger(\mathbf{r}) c_\downarrow^\dagger(\mathbf{r}) c_\downarrow(\mathbf{r}) c_\uparrow(\mathbf{r})\, \mathrm{d}\mathbf{r}, \tag{2.1}$$

where H_0 is a quadratic Hamiltonian diagonal in spin associated to the Green function g, while a local interaction of strength γ couples particles of opposite spins. The operator $c_s(\mathbf{r})$ destroys an electron of spin s at position $\mathbf{r}$. From eq. (1.101) and eq. (1.100) we deduce the expressions of the actions

$$S_0[\bar\psi, \psi] = \sum_\sigma \iint \bar\psi_\sigma(\mathbf{r}, t) g^{-1}(\mathbf{r}, t) \psi_\sigma(\mathbf{r}, t)\, \mathrm{d}\mathbf{r}\, \mathrm{d}t, \tag{2.2}$$

$$S_{\mathrm{int}}[\bar\psi, \psi] = -\gamma \iint \bar\psi_\uparrow(\mathbf{r}, t) \bar\psi_\downarrow(\mathbf{r}, t) \psi_\downarrow(\mathbf{r}, t) \psi_\uparrow(\mathbf{r}, t)\, \mathrm{d}\mathbf{r}\, \mathrm{d}t, \tag{2.3}$$

where ψ_s is a Grassmann field. Thus, the partition function is

$$Z = \int \mathscr{D}[\bar{\psi},\psi] e^{\frac{i}{\hbar}\left(S_0[\bar{\psi},\psi]+S_{\text{int}}[\bar{\psi},\psi]\right)}. \tag{2.4}$$

The quartic interaction $\iint \bar{\psi}_\uparrow(\mathbf{r},t)\bar{\psi}_\downarrow(\mathbf{r},t)\psi_\downarrow(\mathbf{r},t)\psi_\uparrow(\mathbf{r},t)$ prevents us from exactly integrating the above integral, *id est* it is a many-body problem. Even a small attractive interaction, corresponding to $\gamma<0$, is expected to collapse the Fermi sea, thus a perturbative development in the interaction strength γ is not recommended. Yet, a mean field approximation provides a good description of the superconductor physics. The first step is to introduce a field Δ that describes the configuration of $\psi_\downarrow(\mathbf{r},t)\psi_\uparrow(\mathbf{r},t)$, this is done by a Hubbard-Stratonovich transform. The integration over this new field is then approximated by the saddle-point method.

2.1.2 Hubbard-Stratonovich transform

The complex Gaussian integral in the continuum limit reads as

$$\int \mathrm{d}(\bar{\mathbf{z}},\mathbf{z}) e^{-\mathbf{z}^\dagger \mathbf{A}\mathbf{z}+\mathbf{j}^\dagger\mathbf{z}+\mathbf{z}^\dagger\mathbf{j}'} = \frac{e^{\mathbf{j}^\dagger\mathbf{A}^{-1}\mathbf{j}'}}{\det\{\mathbf{A}\}}, \tag{2.5}$$

where $\mathbf{A}$ is a complex N-dimensional matrix with positive definite Hermitian part, while $\mathbf{j}$ and $\mathbf{j}'$ are arbitrary vectors. With this relation at hand, we introduce a first composite bosonic field $b(\mathbf{r},t)=\psi_\downarrow(\mathbf{r},t)\psi_\uparrow(\mathbf{r},t)$ such that the quartic interaction is rewritten as

$$S_{\text{int}}[\bar{\psi},\psi] = -\gamma \iint \bar{b}(\mathbf{r},t) b(\mathbf{r},t)\,\mathrm{d}\mathbf{r}\,\mathrm{d}t. \tag{2.6}$$

Performing the following substitutions in the above integral

$$\mathbf{j}^\dagger \leftarrow \frac{i\bar{b}}{\hbar}, \quad \mathbf{j}' \leftarrow \frac{ib}{\hbar} \text{ and } \mathbf{A}^{-1} \leftarrow i\gamma\hbar, \tag{2.7}$$

we have

$$e^{\frac{i}{\hbar}S_{\text{int}}[\bar{\psi},\psi]} = e^{\frac{-i\gamma}{\hbar}\iint \bar{b}(\mathbf{r},t)b(\mathbf{r},t)\mathrm{d}\mathbf{r}\,\mathrm{d}t}, \tag{2.8}$$

$$= \int \mathscr{D}\left[\bar{\Delta},\Delta\right] e^{\frac{i}{\hbar}\iint \frac{1}{\gamma}|\Delta|^2+\left(\bar{b}\Delta+b\bar{\Delta}\right)\mathrm{d}\mathbf{r}\,\mathrm{d}t}, \tag{2.9}$$

where Δ is a bosonic field and the determinant has been absorbed in the measure $\mathscr{D}\left[\bar{\Delta},\Delta\right]$. This transformation amounts to replace the electron-electron interaction with an interaction between the electrons and a bosonic field Δ, see fig. 2.1. The interacting part of the action is now expressed as a function of 4 fields $S_{\text{int}}[\bar{\Delta},\Delta,\bar{\psi},\psi]$

$$Z = \int \mathscr{D}[\bar{\Delta},\Delta,\bar{\psi},\psi] e^{\frac{i}{\hbar}\left(S_0[\bar{\psi},\psi]+S_{\text{int}}[\bar{\Delta},\Delta,\bar{\psi},\psi]\right)}. \tag{2.10}$$

We introduce the *Nambu spinor* representation that gathers in the same object the holes and particles degrees of freedom

$$\Psi = \begin{pmatrix}\psi_\uparrow \\ \bar{\psi}_\downarrow\end{pmatrix}, \qquad \Psi^\dagger = \begin{pmatrix}\bar{\psi}_\uparrow & \psi_\downarrow\end{pmatrix}. \tag{2.11}$$

This permits to define the *Gor'kov Green function* acting on Nambu spinors

$$\mathscr{G}^{-1}[\Delta] = \begin{pmatrix} g^{-1} & \Delta \\ \bar{\Delta} & -g^{-1\,T}\end{pmatrix}, \tag{2.12}$$

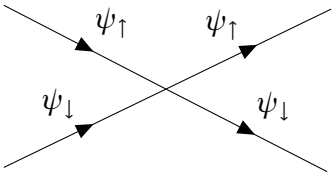

(a) Initial interaction

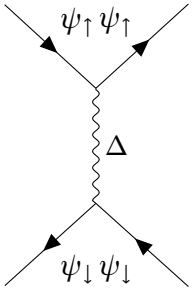

(b) Interaction after bosonization

Figure 2.1: The Hubbard Stratonovich transform replaces the initial electron-electron interaction by an interaction mediated by a bosonic field.

where we emphasize its dependence on the field Δ. Thus, the action can be disguised into a quadratic form

$$S[\bar{\Delta},\Delta,\bar{\psi},\psi]=\frac{i}{\hbar}\iint\frac{1}{\gamma}|\Delta|^2+\bar{\Psi}\mathcal{G}^{-1}[\Delta]\Psi\,\mathrm{d}\mathbf{r}\,\mathrm{d}t. \tag{2.13}$$

To derive this last equation, we use the relation

$$\iint\bar{\psi}_\downarrow g^{-1}\psi_\downarrow\,\mathrm{d}\mathbf{r}\,\mathrm{d}t=-\iint\psi_\downarrow {g^{-1}}^T\bar{\psi}_\downarrow\,\mathrm{d}\mathbf{r}\,\mathrm{d}t, \tag{2.14}$$

this states that the Green function of holes satisfies $g_h^{-1}=-{g^{-1}}^T$. We thus write the partition function as

$$Z=\int\mathscr{D}[\bar{\Delta},\Delta]\int\mathscr{D}[\bar{\Psi},\Psi]e^{\frac{i}{\hbar}\iint\frac{1}{\gamma}|\Delta|^2+\bar{\Psi}\mathcal{G}^{-1}[\Delta]\Psi\,\mathrm{d}\mathbf{r}\,\mathrm{d}t}. \tag{2.15}$$

The integration over the fermionic fields can be carried out using the relation of appendix A

$$\boxed{\int\mathscr{D}\left[\bar{\psi},\psi\right]e^{-\int\bar{\psi}\mathbf{A}\psi}=\det\mathbf{A},} \tag{2.16}$$

where $\mathbf{A}$ is an arbitrary matrix, and the integration is done over Grassmann fields. Thus we have

$$Z=\int\mathscr{D}[\bar{\Delta},\Delta]e^{\frac{i}{\hbar}\iint\frac{1}{\gamma}|\Delta|^2\,\mathrm{d}\mathbf{r}\,\mathrm{d}t+\ln\det\left(-\frac{i}{\hbar}\mathcal{G}^{-1}\left[\bar{\Delta},\Delta\right]\right)}. \tag{2.17}$$

The introduction of the Gor'kov Green function underlines that the field Δ acts as an effective force that couples electrons to holes. It is the result of the interaction of each particle with many others. Thus, one may expect that the field Δ does not deviate much from its average configuration. This suggests developing a mean-field approximation.

2.1.3 Mean field approximation

The mean field approximation amounts to replace the integration over Δ by the value of the integrand at a saddle point of the action, at this point Δ satisfies

$$\frac{\delta S}{\delta\Delta} = 0, \tag{2.18a}$$

$$\frac{\delta S}{\delta\bar{\Delta}} = 0. \tag{2.18b}$$

Using the relation $\ln(\det \mathbf{A}) = \mathrm{tr}(\ln \mathbf{A})$, we obtain

$$\frac{\delta}{\delta\Delta}\left\{\frac{i}{\hbar}\iint\frac{1}{\gamma}|\Delta|^2\,\mathrm{d}\mathbf{r}\,\mathrm{d}t+\mathrm{tr}\ln\left(\frac{1}{i\hbar}\mathscr{G}^{-1}\left[\bar{\Delta},\Delta\right]\right)\right\} = 0, \tag{2.19a}$$

$$\frac{\delta}{\delta\bar{\Delta}}\left\{\frac{i}{\hbar}\iint\frac{1}{\gamma}|\Delta|^2\,\mathrm{d}\mathbf{r}\,\mathrm{d}t+\mathrm{tr}\ln\left(\frac{1}{i\hbar}\mathscr{G}^{-1}\left[\bar{\Delta},\Delta\right]\right)\right\} = 0. \tag{2.19b}$$

These functional derivatives can be evaluated as follows

$$\frac{\delta}{\delta\Delta(\mathbf{r},t)}\left\{\frac{i}{\hbar}\iint\frac{1}{\gamma}|\Delta|^2\,\mathrm{d}\mathbf{r}\,\mathrm{d}t+\mathrm{tr}\ln\left(\frac{1}{i\hbar}\mathscr{G}^{-1}\right)\right\} = \frac{i}{\hbar\gamma}\bar{\Delta}(\mathbf{r},t)+\frac{\delta\,\mathrm{tr}\ln\left(\frac{1}{i\hbar}\mathscr{G}^{-1}\right)}{\delta\Delta(\mathbf{r},t)}. \tag{2.20}$$

Using the relation [29]

$$\frac{\delta\,\mathrm{tr}\,f(A(x))}{\delta x} = \mathrm{tr}\,f'(A)\frac{\delta A(x)}{\delta x}, \tag{2.21}$$

we get

$$\frac{\delta\,\mathrm{tr}\ln\left(\frac{1}{i\hbar}\mathscr{G}^{-1}\right)}{\delta\Delta(\mathbf{r},t)} = \mathrm{tr}\left(\frac{\mathscr{G}}{\hbar}\frac{\delta\mathscr{G}^{-1}}{\delta\Delta(\mathbf{r},t)}\right), \tag{2.22}$$

$$= \frac{1}{\hbar}\mathscr{G}_{21}(\mathbf{r},t;\mathbf{r},t), \tag{2.23}$$

where $\mathscr{G}_{p,q}(\mathbf{r},t;\mathbf{r}',t')$ is the element at indices p,q in the Nambu space of the *Gor'kov Green function*. Once again, we absorbed $\hbar$ in its definition: $\mathscr{G}\cdot\mathscr{G}^{-1} = \hbar$. By the same means, we express $\frac{\delta S}{\delta\bar{\Delta}}$ and we finally deduce the following relations

$$\bar{\Delta}(\mathbf{r},t) = i\gamma\mathscr{G}_{21}(\mathbf{r},t;\mathbf{r},t), \tag{2.24a}$$

$$\Delta(\mathbf{r},t) = i\gamma\mathscr{G}_{12}(\mathbf{r},t;\mathbf{r},t). \tag{2.24b}$$

Upon replacing the Green function by its definition, we get

$$\bar{\Delta}(\mathbf{r},t) = \gamma\left\langle\mathbf{T_C}\bar{\psi}_\downarrow(\mathbf{r},t)\bar{\psi}_\uparrow(\mathbf{r},t)\right\rangle \tag{2.25a}$$

$$\Delta(\mathbf{r},t) = \gamma\left\langle\mathbf{T_C}\psi_\uparrow(\mathbf{r},t)\psi_\downarrow(\mathbf{r},t)\right\rangle \tag{2.25b}$$

As the time ordering operator is applied to symbols that live at the same instant, we can simply drop it, the reader may convince himself by adding a small time increment to one of the time indices and take the limit. We finally get the self-consistent equations

$$\boxed{\bar{\Delta}(\mathbf{r},t) = \gamma\left\langle\bar{\psi}_\downarrow(\mathbf{r},t)\bar{\psi}_\uparrow(\mathbf{r},t)\right\rangle,} \tag{2.26a}$$

$$\boxed{\Delta(\mathbf{r},t) = \gamma\left\langle\psi_\uparrow(\mathbf{r},t)\psi_\downarrow(\mathbf{r},t)\right\rangle.} \tag{2.26b}$$

As we are considering a mean field approximation, the integration over the bosonic field configuration is replaced by the integrand saddle point value, this leads to

$$Z_{\mathrm{MF}} = \int\mathscr{D}[\bar{\Psi},\Psi]e^{\frac{i}{\hbar}\iint\frac{1}{\gamma}|\Delta|^2+\bar{\Psi}\mathscr{G}^{-1}[\Delta]\Psi\,\mathrm{d}\mathbf{r}\,\mathrm{d}t}, \tag{2.27}$$

where Δ is the mean field configuration provided by eq. (2.26). Absorbing the irrelevant constant in the measure, we finally obtain

$$\boxed{Z_{MF} = \int\mathscr{D}[\bar{\Psi},\Psi]e^{\frac{i}{\hbar}\iint\bar{\Psi}\mathscr{G}^{-1}[\Delta]\Psi\,\mathrm{d}\mathbf{r}\,\mathrm{d}t}.} \tag{2.28}$$

This is the partition function of a free theory whose inverse Green function is $\mathscr{G}^{-1}$. Thus, we can define an effective Hamiltonian, see section 1.7

$$\mathscr{H}(\mathbf{r},t)\equiv\begin{pmatrix} H_0(\mathbf{r},t) & \Delta(\mathbf{r},t) \\ \bar{\Delta}(\mathbf{r},t) & -\bar{H}_0(\mathbf{r},t)\end{pmatrix}. \tag{2.29}$$

This is the *Bogoliubov-de Gennes* Hamiltonian which provides a description of excitations in BCS superconductors in a mean-field approximation. The wave function written in the Nambu representation shall be solution of the *Bogoliubov-de Gennes* Hamiltonian

$$\mathscr{H}(\mathbf{r},t)\begin{pmatrix}\psi_\uparrow \\ \psi_\downarrow^\dagger\end{pmatrix}=i\hbar\frac{\mathrm{d}}{\mathrm{d}t}\begin{pmatrix}\psi_\uparrow \\ \psi_\downarrow^\dagger\end{pmatrix}. \tag{2.30}$$

One may think of $-\bar{H}_0$ as the Hamiltonian governing the dynamics of holes. Hence, the above equation describes how electrons of spin up are coupled to holes of spin down by the effective interaction Δ. That induces the superconducting gap. This concludes the derivation of the mean-field approximation of the BCS theory. To practice, let's derive some properties of BCS superconductors from this model.

2.1.4 BCS superconducting gap

We consider the case of a constant and uniform order parameter Δ, in thermal equilibrium. The states of H_0 are $|n\rangle$ of energy ϵ_n

$$H_0=\epsilon_n\left(c_{\uparrow,n}^\dagger c_{\uparrow,n}+c_{\downarrow,n}^\dagger c_{\downarrow,n}\right), \tag{2.31}$$

where $c_{s,n}$ destroys an electron of spin s in the mode n. As Δ is uniform, the effective Hamiltonian is block diagonal in the basis $\{|n\rangle\}$, thus we only have to solve the following small equation

$$\begin{pmatrix}\epsilon_n & \Delta \\ \bar{\Delta} & -\epsilon_n\end{pmatrix}\begin{pmatrix}u_n \\ v_n\end{pmatrix}=E_n\begin{pmatrix}u_n \\ v_n\end{pmatrix}, \tag{2.32}$$

where E_n is the state energy, and u_n, v_n are complex numbers subject to the constraint $|u_n|^2+|v_n|^2=1$. This eigenvector equation is swiftly solved, the energies are

$$E_{n,e/h}=\pm\sqrt{\epsilon_n^2+|\Delta|^2}, \tag{2.33}$$

and the corresponding eigenvector $(u_{n,e/h}, v_{n,e/h})^T$ satisfies [1]

$$\frac{v_{n,e/h}}{u_{n,e/h}}=\left(\epsilon_n+E_{n,e/h}\right)\Delta^{-1}. \tag{2.34}$$

In the limit where $|E|\gg\Delta$, the solutions of positive and negative energies correspond respectively to electrons and holes. So, those solutions are named *electron-like* and *hole-like*. From eq. (2.33) we see that a gap appears at the Fermi level. This gap is in the *excitation spectrum* of the Cooper pair condensate that lays at the Fermi level. It means that a finite amount of energy is required to break a Cooper pair, this protects the condensate from numerous dissipation mechanisms [13]. Upon approximating the density of state in the normal metal by a constant n_F close to the Fermi energy, we can evaluate the density of states in the superconductor in the vicinity of the Fermi energy

$$n(E)=\begin{cases} n_F\frac{|E|}{\sqrt{E^2-|\Delta|^2}} & |E|>|\Delta| \\ 0 & |E|<|\Delta|\end{cases}, \tag{2.35}$$

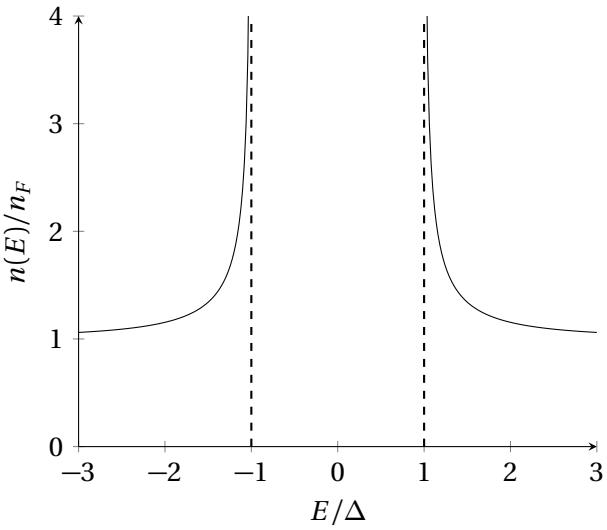

Figure 2.2: BCS density of states in the vicinity of the Fermi energy.

the corresponding spectrum is illustrated in fig. 2.2. By deriving the above formula, one must not double count the spin states: in the Nambu representation, the spin down particles are described as holes, while the spin-up particles are depicted as electrons. In equilibrium eq. (2.26) does not depend on time, once projected on the eigenvector of H_0, we get

$$\Delta(\mathbf{r}) = \gamma \sum_n \left\langle c_{\uparrow,n} c_{\downarrow,n} \right\rangle |w_n(\mathbf{r})|^2, \tag{2.36a}$$

$$\bar{\Delta}(\mathbf{r}) = \gamma \sum_n \left\langle c^\dagger_{\downarrow,n} c^\dagger_{\uparrow,n} \right\rangle |w_n(\mathbf{r})|^2, \tag{2.36b}$$

where $w_n(\mathbf{r})$ is the orbital part of the wave function associated to $c_{s,n}$. These averages cannot be directly evaluated using the Fermi distribution as the eigenvectors of H_0 are not eigenvectors of H. Thus, we introduce $b_{n,e/h}$ as the destruction operators that diagonalize the de Gennes Hamiltonian. They can be expressed as a combination of the initial destruction and creation operators

$$\begin{pmatrix} b_{n,e} \\ b^\dagger_{n,h} \end{pmatrix} = \begin{pmatrix} u_{n,e} & v_{n,e} \\ u_{n,h} & v_{n,h} \end{pmatrix} \begin{pmatrix} c_{\uparrow,n} \\ c^\dagger_{\downarrow,n} \end{pmatrix}. \tag{2.37}$$

With this definition of the new creation and destruction operators, we ensure that the energies of corresponding excitations are positive. Thereafter, we call those particles bogoliubon. They follow the Fermi statistic. Thus, their thermal distribution is set by the Fermi function $f_T(E)$. The matrix that appears in the above equation is formed by the normalized eigenvectors of a hermitian matrix, thus it is a unitary. One may recast it into

$$\mathbf{P} \equiv \begin{pmatrix} u_{n,e} & v_{n,e} \\ u_{n,h} & v_{n,h} \end{pmatrix} = \begin{pmatrix} u_n & v_n \\ -\bar{v}_n & \bar{u}_n \end{pmatrix}, \tag{2.38}$$

where we define $u_n \equiv u_{n,e}$ and $v_n \equiv v_{n,e}$. Thus, we have

$$\begin{pmatrix} c_{\uparrow,n} \\ c^\dagger_{\downarrow,n} \end{pmatrix} = \mathbf{P}^\dagger \begin{pmatrix} b_{n,e} \\ b^\dagger_{n,h} \end{pmatrix}. \tag{2.39}$$

We thus deduce that

$$\Delta(r) = \gamma \bar{u}_n v_n \left(1 - \left\langle b^\dagger_{n,e} b_{n,e} \right\rangle - \left\langle b^\dagger_{n,h} b_{n,h} \right\rangle\right) |w_n(\mathbf{r})|^2. \tag{2.40}$$

[1] Be careful, this definition of the coefficients $u_{n,e/h}$ and $v_{n,e/h}$ differs from the one used in *Introduction to superconductivity* by Michael Tinkham [13]

This can be expressed using the Fermi distribution

$$\Delta(r) = \gamma \sum_n \bar{u}_n v_n \big(1-2f_T(E_n)\big)|w_n(\mathbf{r})|^2, \tag{2.41a}$$

$$= -\gamma \sum_n \frac{\Delta(r)}{2E_n} \tanh\left(\frac{E_n\beta}{2}\right). \tag{2.41b}$$

This equation is usually recast as

$$\frac{1}{\gamma} = -\sum_n \frac{\tanh\big(E_n\beta/2\big)}{2E_n}. \tag{2.42}$$

To go further, let's consider the case of a clean bulk material. The modes of H_0 are thereby plane waves which are characterized by their wave-vector $\mathbf{k}$, thus we have

$$\frac{1}{\gamma} = -\int \frac{n(\mathbf{k})\mathrm{d}\mathbf{k}}{2E_\mathbf{k}} \tanh\left(\frac{E_\mathbf{k}\beta}{2}\right), \tag{2.43}$$

where $n(\mathbf{k})$ is the normal density of states. The main parameter to describe a BCS superconductor is the critical temperature T_C. We evaluate it by setting $\Delta = 0$. Upon approximating the normal density of states by its value at the Fermi energy n_F, we have

$$\frac{1}{n_F\gamma} = -\int_0^{\hbar\omega_c\beta_c/2} \frac{\tanh(x)}{x}\,\mathrm{d}x, \tag{2.44}$$

where n_F is the normal density of states at the Fermi energy, ω_c is a cut-off depending on the microscopic details and $\beta_c = 1/k_B T_C$. In classical BCS superconductor, we have $\omega_c \sim \omega_D$ with ω_D the Debye frequency. The integral can be evaluated exactly [13]

$$\int_0^{\hbar\omega_c\beta_c/2} \frac{\tanh(x)}{x}\,\mathrm{d}x = \ln\left(\frac{2e^{\gamma_E}\beta_c\hbar\omega_c}{\pi}\right) \approx \ln\big(1.13\beta_c\hbar\omega_c\big), \tag{2.45}$$

where γ_E is the Euler constant. We finally have the expression of the critical temperature T_c

$$\boxed{k_B T_c \approx 1.13\hbar\omega_c \exp\left(\frac{1}{\gamma n_F}\right).} \tag{2.46}$$

The critical temperature is directly accessible by experiment , and it permits to characterize the temperature dependence of the gap [13]. Close to T_C the gap equation admits an approximate solution

$$\frac{\Delta(T)}{\Delta(0)} \approx 1.74\sqrt{1-\frac{T}{T_c}} \text{ for } T \approx T_C. \tag{2.47}$$

Now that we have introduced the BCS superconductivity we can turn to a description of the Josephson effect.

2.2 Josephson junctions

A dissipation less current can flow at equilibrium between superconductors separated by a non-superconducting material if this weak link permits a phase coherent transport of charges, see fig. 2.3. Devices designed to harness this effect are called Josephson junctions. The Josephson relations [13, 36–38] capture the essential of their physics.

$$\boxed{I(\varphi) = \frac{2e}{\hbar}\frac{\mathrm{d}E_J(\varphi)}{\mathrm{d}\varphi}, \qquad \frac{\mathrm{d}\varphi}{\mathrm{d}t} = \frac{2eV}{\hbar}} \tag{2.48}$$

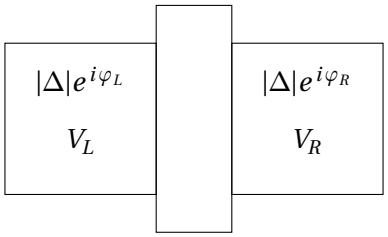

Figure 2.3: Schematic of a Josephson junction. The superconducting leads are connected by a non-superconducting element designed as the *weak ink*

.

Where $\varphi = \varphi_L - \varphi_R$ is the phase difference across the junction, $E_J(\varphi)$ is the junction energy and $V = V_L - V_R$ is the voltage bias. As the barrier is usually not gaped at the Fermi energy, excitation within the superconducting energy gap are trapped in the barrier, they form the Andreev bound states (ABSs). In junction shorter the coherence length, $\xi = \frac{\hbar v_F}{\pi|\Delta|}$ with v_F the Fermi velocity in the weak-link, the system energy is fixed by occupation of the ABSs. ξ reflects the size of the Cooper pair [13]. Hereafter, we introduce the microscopic reflection mechanism that permits the formation of those states and we derive the spectrum of a typical junction whose barrier is either a non-superconducting metal (SNS junction) or a quantum dot (SQDS junction). We then discuss the out-of-equilibrium properties of these devices.

2.2.1 Andreev reflections

Andreev reflections appear at the interface between a superconductor and a metal. Incident particles on the interface coming from the normal side of the junction at energy within the gap have to bound to a particle of opposed spin to form a Cooper pair, as there is no single particle state available. Hence, the incident particle is reflected as its antiparticle of opposite spin while a cooper pair forms in the superconductor. The overall process results in the effective transfer of twice the electronic charge. This process is captured by the Bogoliubov de Gennes eq. (2.29). We consider a one dimensional infinite lead that is described by the following stationary equation

$$\begin{pmatrix} H_0(x) & \Delta(x) \\ \bar{\Delta}(x) & -\bar{H}_0(x) \end{pmatrix} \begin{pmatrix} u(x) \\ v(x) \end{pmatrix} = E \begin{pmatrix} u(x) \\ v(x) \end{pmatrix}, \tag{2.49}$$

The normal state Hamiltonian is

$$H_0 = -\frac{\hbar^2}{2m}\frac{\mathrm{d}^2}{\mathrm{d}x^2} \tag{2.50}$$

where m is the effective mass of electrons. The order parameter Δ satisfies $\Delta(x) = |\Delta|e^{i\varphi}\Theta(-x)$, where Θ is the Heaviside function and φ is the phase of the superconducting order parameter, see fig. 2.4. As previously, the order parameter being constant on each part of the real line, the equation restricted to the normal or superconducting part is block diagonal in the plane wave basis $w_k(x) = e^{ikx}$

$$-\frac{\hbar^2}{2m}\frac{\mathrm{d}}{\mathrm{d}x} w_k(x) = \epsilon_k w_k(x) \tag{2.51}$$

Thereafter, we will consider only excitations close to the Fermi surface, thus the dispersion relation is $k(E) = k_F + E/\hbar v_F$, with v_F is the Fermi velocity $v_F = \sqrt{2E_F/m}$. At energy E, in the normal metal a left propagating electron and a right propagating hole are respectively described by

$$\psi_e^{\leftarrow}(x>0) = \begin{pmatrix} 1 \\ 0 \end{pmatrix} e^{-i(k_F + E/\hbar v_F)x} \tag{2.52a}$$

$$\psi_h^{\rightarrow}(x>0) = \begin{pmatrix} 0 \\ 1 \end{pmatrix} e^{i(k_F - E/\hbar v_F)x} \tag{2.52b}$$

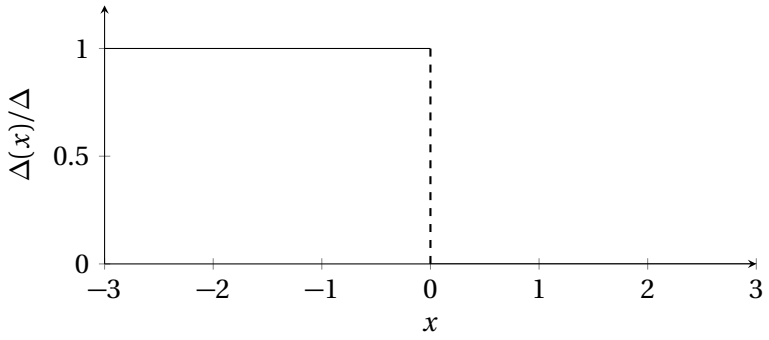

Figure 2.4: Order parameter profile

While the superconductor does not admit propagating modes within the gap, we can build an evanescent solution. It amounts to replace ϵ_n in eq. (2.33) and eq. (2.34) by $i\epsilon$, ϵ must be positive to ensure that the corresponding wave-function vanishes. Hence, we have

$$\psi_s(x<0)=\begin{pmatrix}u\\v\end{pmatrix}e^{x\frac{\sqrt{\Delta^2-E^2}}{\hbar v_F}} \tag{2.53}$$

We can now evaluate how an incoming electron is reflected by matching the wave function at $x=0$

$$\psi_e^{\leftarrow}(0)+r_A\psi_h^{\rightarrow}(0)=\psi_s(0) \tag{2.54}$$

$$\Leftrightarrow\begin{pmatrix}1\\0\end{pmatrix}+r_A\begin{pmatrix}0\\1\end{pmatrix}=\begin{pmatrix}u\\v\end{pmatrix}. \tag{2.55}$$

Thus the reflection coefficient is

$$r_{A,e}(|E|<|\Delta|,\varphi)=e^{-i\varphi}\left(\frac{E}{|\Delta|}-i\frac{\sqrt{|\Delta|^2-E^2}}{|\Delta|}\right) \tag{2.56}$$

$$\chi(E)=-\arccos\left(\frac{E}{|\Delta|}\right)-\varphi. \tag{2.57}$$

The same procedure can be used to evaluate the reflection coefficient for incoming holes, it leads to $r_{A,h}(E,\varphi)=r_{A,e}(E,-\varphi)$. Thus, we define $r_A\equiv r_{A,e}$. This expression can be analytically prolonged for all value of E [38]. The coefficient r_A is plot on section 2.2.1.

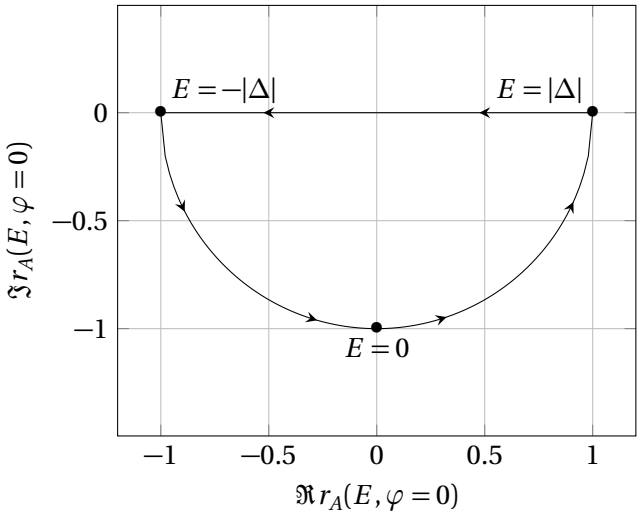

Figure 2.5: Real and imaginary part of the Andreev reflection coefficient at $\varphi = 0$.

2.2.2 Andreev bound states

From the above description of the Andreev reflection, it appears that an interface between a superconducting lead and a normal region acts like a perfectly reflecting mirror for sub-gap excitations of the normal region. Hence, a Josephson junction formed by two of such interfaces is an electronic equivalent of Fabry-Perot cavity. As a result, resonances form. They are the *Andreev bounds states*. Or said otherwise, the quasiparticles are trapped, thus discreet bound states form. Considering two superconductors of order parameter $\Delta_{L/R} = |\Delta| e^{i\varphi_{L/R}}$, that are connected by a perfectly transmitting weak-link much shorter than its coherence length. An electron is first reflected into a hole at an interface and back in an electron at the other. Thus, through a cycle in the cavity, particles acquire a phase χ

$$\chi = \pm\varphi - 2\arccos\left(\frac{E}{|\Delta|}\right) \tag{2.58}$$

Where $\varphi = \varphi_R - \varphi_L$, while $+$ and $-$ respectively correspond to left moving and right moving electrons. As we are considering only excitation close to the Fermi surface, the propagation phase cancel out. A resonance appears when the accumulated phase is a multiple of 2π. Thus, bound states energies solve the equation

$$\mp\varphi - 2\arccos\left(\frac{E_{\rightleftarrows}}{|\Delta|}\right) = 0 \mod 2\pi. \tag{2.59}$$

The junction spectrum is shown on fig. 2.6, its expression is

$$E_{\rightleftarrows} = \mp|\Delta|\cos\left(\frac{\varphi}{2}\right)\operatorname{sgn}\left\{\sin\left(\frac{\varphi}{2}\right)\right\}, \tag{2.60}$$

where states of energy $E_{\rightarrow}$ contributes to current from the left to the right leads, while $E_{\leftarrow}$ correspond to a current in the opposite direction. This might be seen by evaluating the current associate to the occupation of each state. From the Josephson equation we have

$$I_{\rightleftarrows} = \frac{2e}{\hbar}\frac{\mathrm{d}E_{\rightleftarrows}}{\mathrm{d}\varphi} = \pm\frac{e|\Delta|}{\hbar}\left|\sin(\varphi/2)\right|, \tag{2.61}$$

this current are plotted on fig. 2.7. Those bound states cross perfectly at the Fermi energy when $\varphi = \pi \mod 2\pi$. They are in contact with the continuum at $\varphi = 0 \mod 2\pi$. Any backscattering induces a hybridization of the different Andreev bounds states that results in the opening of a gap at $\varphi = \pi \mod 2\pi$. To describe the fate of Andreev bound states in the presence of scattering, we first need to introduce the scattering formalism.

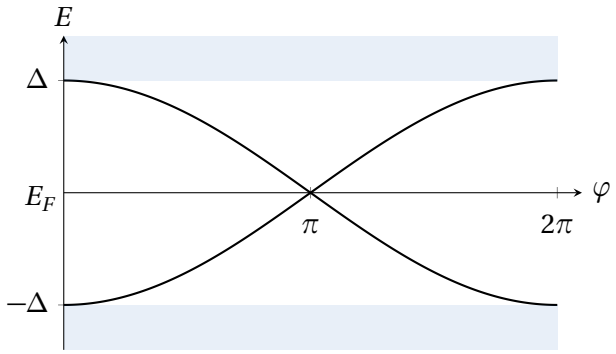

Figure 2.6: Spectrum of a short Josephson junction in the absence of scattering in the weak link. At $\varphi = \pi$ there is a perfect crossing.

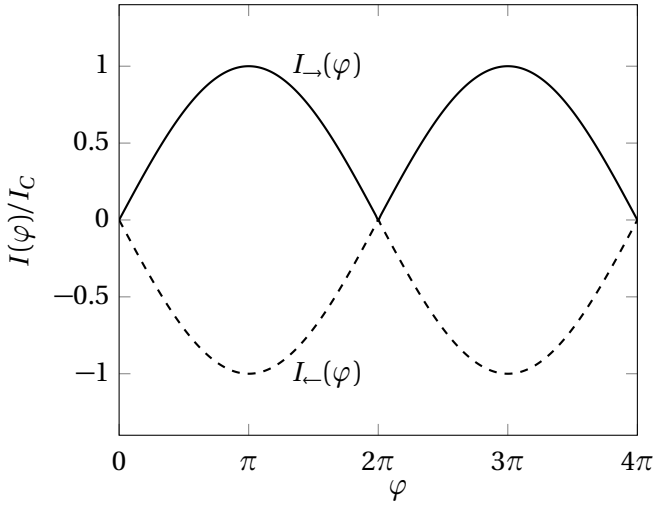

Figure 2.7: Current associated to each bound state in a perfectly ballistic junction.

2.2.3 Scattering formalism

Coherent transport in non-interacting stationary systems can be depicted in terms of scattering matrices, in a manner similar to the description of microwave hardware. Considering a scattering center connected to leads that support well-defined propagating modes at energy E, $\psi_n^{\text{in}}(E)$ and $\psi_n^{\text{out}}(E)$ designate modes propagating toward and outward the scatterer, respectively. They are normalized so that current probabilities are equal. An incident wave packet Ψ_{in} can be decomposed into those modes

$$\Psi_{\text{in}}(E) = \sum_n a_n(E)\psi_n^{\text{in}}(E), \tag{2.62}$$

while the scattered wave packet reads as

$$\Psi_{\text{out}}(E) = \sum_n b_n(E)\psi_n^{\text{out}}(E). \tag{2.63}$$

The scattering matrix $\mathbf{S}$ links the amplitudes of the outgoing modes to the incoming ones

$$\boxed{b_n = \sum_m S_{n,m} a_m} \tag{2.64}$$

This relation between the incoming and outcoming modes is pictured by fig. 2.8. The elastic scattering process must conserve the probability flow at each energy, thus the scattering matrix is unitary $\mathbf{S}^\dagger(E)\mathbf{S}(E) = \mathbb{1}$. It can be expressed in terms of retarded and advanced Green functions using the Fisher-Lee relation

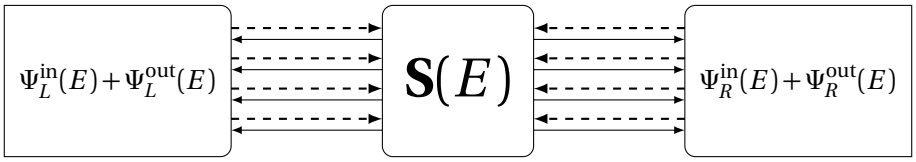

Figure 2.8: The scattering matrix describes how a nanostructure scatters the incoming modes, pictured by dashed arrows, among all the outgoing modes, represented by solid lines. Here we represent only two leads L and R, but a scattering matrix can represent more general structures.

[39].

$$s_{n,m} = -\delta_{m,n} + i\hbar \sum_{p,q} \sqrt{v_n v_m} \iint \chi_n(y_p) G^R_{pq} \chi_m(y_q) \mathrm{d}y_p \mathrm{d}y_q, \tag{2.65}$$

where χ_m are the transverse mode wave-functions, y_p are the coordinate along the surfaces at which the scattering amplitudes are evaluated, v_n are the modes velocities. The scattering formalism provide a very simple way to describe non-interacting structure at equilibrium. The scattering matrix of quantum devices can easily be numerically evaluated using open source tool such as Kwant [40].

2.2.4 SNS junctions

In its simplest form, a Josephson junction is made of two superconductors connected together by a piece of metal or insulator of length L. By modelling the weak link as a scattering centre, it can be described within the scattering formalism.

2.2.4.1 Spectrum of SNS junctions

We suppose that the scattering events that occur within the weaklink conserve the particle spin and does not depend on it. Thus, it is described by a scattering matrix $\mathbf{S_M}(E)$ which is block diagonal in the Nambu indices. The holes scattering matrix $\mathbf{S_h}$ can be deduced from the electrons scattering matrix $\mathbf{S_e}$ by the relation

$$\mathbf{S_h}(E) = \bar{\mathbf{S}}_\mathbf{e}(-E). \tag{2.66}$$

This expression is justified by handwavy arguments in [38], it can be swiftly derived by considering the expression of the scattering matrix in terms of Greens functions eq. (2.65). We further suppose that the particles spend a very short time t_D in the weak link, *id est* $t_D|\Delta| \ll h$. Thus, by virtue of time energy uncertainty relation, its scattering matrix is energy independent on the scales we consider. By the same consideration, the remaining superconducting coupling can be disregard in the link, the interested reader may again have a look at [38]. Up to properly selecting the basis, we can suppose that the different channels are independent [26], thus we can consider one channel at a time. Finally, we suppose that the system is symmetric under time reversal, this implies $\mathbf{S_e} = \mathbf{S_e}^T$. Once the symmetry constraint is combine with the

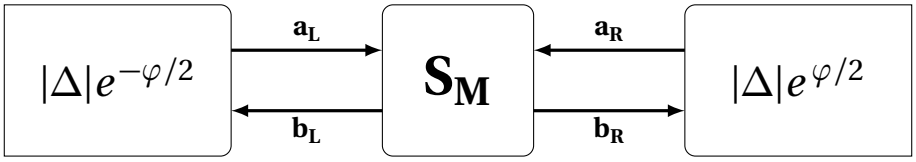

Figure 2.9: $\mathbf{a_L}$ and $\mathbf{a_R}$ are the wave functions amplitudes before scattering by the weak link, they both comport an electron and a hole part. In the same way, $\mathbf{b_L}$ and $\mathbf{b_R}$ are the amplitudes before reflection by the superconductors.

unitarity of the scattering matrix, one obtain the following parametrization

$$\mathbf{S_e} = \begin{pmatrix} -ir & t \\ t & -ir \end{pmatrix}, \tag{2.67}$$

where the parameters $(r,t) \in \mathbb{C}^2$ satisfy

$$\begin{cases} |r|^2 + |t|^2 &= 1 \\ \arg r &= \arg t \mod \pi \end{cases}. \tag{2.68}$$

The relation describing the scattering by the weak link is thus

$$\begin{pmatrix} \mathbf{b_e} \\ \mathbf{b_h} \end{pmatrix} = \begin{pmatrix} \mathbf{S_e} & 0 \\ 0 & \bar{\mathbf{S}}_\mathbf{e} \end{pmatrix} \begin{pmatrix} \mathbf{a_e} \\ \mathbf{a_h} \end{pmatrix}. \tag{2.69}$$

Thus, we define the scattering matrix of the weak link as

$$\mathbf{S_M} \equiv \begin{pmatrix} \mathbf{S_e} & 0 \\ 0 & \bar{\mathbf{S}}_\mathbf{e} \end{pmatrix}, \tag{2.70}$$

see fig. 2.9. The conversion of electrons into holes is described by the scattering block $\mathbf{s_{he}}$, the opposite process is described by $\mathbf{s_{eh}}$.

$$\mathbf{s_{he}} = \begin{pmatrix} e^{i\chi_L} & 0 \\ 0 & e^{i\chi_R} \end{pmatrix}, \quad \mathbf{s_{he}} = \begin{pmatrix} e^{i\tilde{\chi}_L} & 0 \\ 0 & e^{i\tilde{\chi}_R} \end{pmatrix}, \tag{2.71}$$

where $\chi_{L/R} = -\varphi_{L/R} - \arccos\left(\frac{E}{|\Delta|}\right)$. The full Andreev reflection scattering matrix is:

$$\mathbf{S_A} = \begin{pmatrix} 0 & \mathbf{s_{eh}} \\ \mathbf{s_{he}} & 0 \end{pmatrix} \tag{2.72}$$

The full cavity scattering matrix $\mathbf{S}$ is thus

$$\mathbf{S_{SNS}} = \mathbf{S_A S_M} \tag{2.73}$$

The resonant modes are solution of the equation

$$\mathbf{S_{SNS}} \mathbf{a} = \mathbf{a} \tag{2.74}$$

Thus, the Andreev bound states spectrum is solution of the equation

$$\det\{\mathbf{S_{SNS}}(E) - \mathbb{1}\} = 0 \tag{2.75}$$

This conducts to

$$\frac{E}{|\Delta|} = \pm\sqrt{1 - T\sin\left(\varphi/2\right)^2} \tag{2.76}$$

where $T \equiv |t|^2$ is the channel transmission in the normal state. Hence, any finite amount of backscattering induces an anti-crossing at the Fermi energy, see fig. 2.10. The size of the energy gap between the Andreev states is

$$\delta_E = 2\Delta\sqrt{1-T} \tag{2.77}$$

The full spectrum of a multi-channels junction is the sum of the spectrum of each channel. The ABS spectrum contains enough information to evaluate the current flowing thought a short junction biased by voltage V. Let's first consider the very low voltage regime : $e|V| \ll \eta\hbar \ll |\Delta|$, where η is the relaxation rate toward equilibrium. In this regime the states occupations are given by the thermal distribution. This is the adiabatic regime.

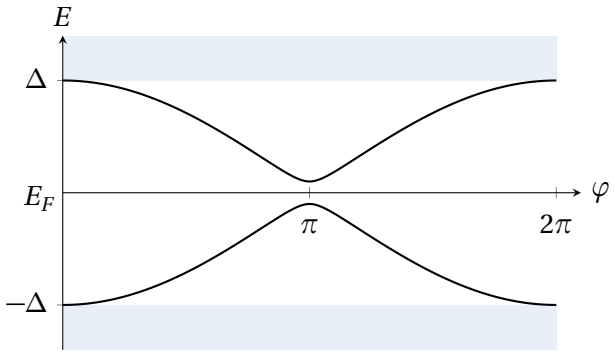

Figure 2.10: Spectrum of a short junction in presence of backscattering at $T = 0.99$.

2.2.4.2 Adiabatic regime

For the sake of clarity, we consider hereafter the single channel case. At thermal equilibrium and low temperature $k_B T \ll \Delta$, only the state $|-\rangle$ which lays below the Fermi level is occupied. Hence, the junction energy is $E_J(\varphi) = E_-(\varphi)$. Using the Josephson relation eq. (2.48), we get the expression of the current going through a channel

$$I_J(\varphi) = \frac{2e}{\hbar}\frac{\mathrm{d}E_-(\varphi)}{\mathrm{d}\varphi}, \tag{2.78}$$

when the weak link is perfectly transparent, the phase current relation is discontinuous, but any backscattering smooths it, see fig. 2.11. In the adiabatic limit, the current through the junction is provided by $I_J(\varphi(t))$. While the phase difference follows

$$\varphi(t) = \frac{2eVt}{\hbar} + \varphi(0). \tag{2.79}$$

As $E_-(\varphi)$ is 2π-periodic, this results in radiation at the Josephson pulsation $\omega_J = \frac{2eV}{\hbar}$ and its harmonics. In this regime there is no DC current flowing through the junction. This is the usual *AC Josephson effect*. For larger voltage biased $e|V| \gg \eta\hbar$ the effect of the relaxation is negligible. The charge transport across

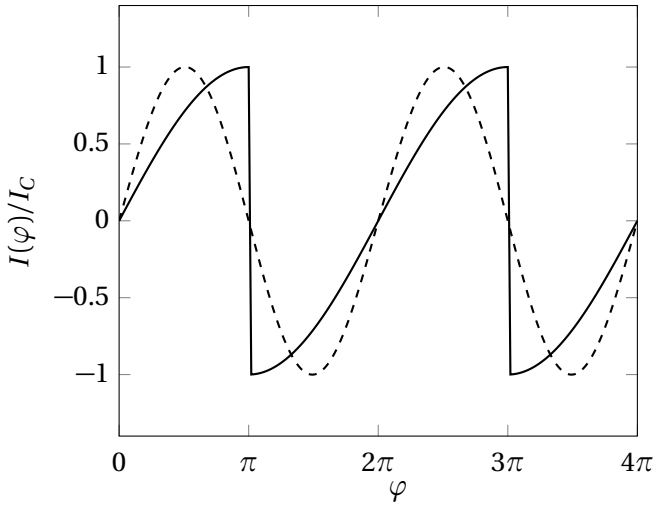

Figure 2.11: Josephson current at equilibrium for $T \ll \Delta$ normalized by the junction critical current I_C. The dashed line correspond a junction of low transmission ($T = 0.1$), the solid line correspond to a perfectly transparent junction ($T = 1$).

the junction is described by the multiple Andreev reflection (MAR) [41].

2.2.4.3 Multiple Andreev Reflection

The applied voltage accelerates the quasiparticles within the weaklink. They gain a bit of energy at each cycle through the cavity until they escape the energy gap after k reflections, see fig. 2.12. These multiple Andreev reflections are responsible for the sub-gap structure $e|V| < |\Delta|$ of the differential conductance $\mathrm{d}V/\mathrm{d}I$: peaks appear at $V = \frac{2\Delta}{en}$ with $n \in \mathbb{Z}$. Indeed, each time $V = \frac{2\Delta}{en}$ a new path formed by $n-1$ reflection opens as depicted on fig. 2.12. It also provides a quantitative description of the current at higher voltage, including the affine part of the $I-V$ characteristic at $eV \gg \Delta$. While the MAR description of the

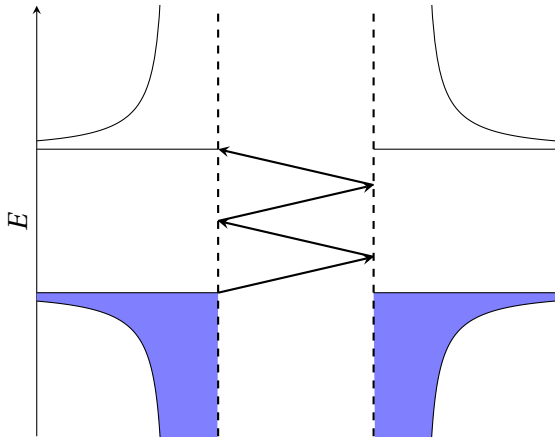

Figure 2.12: When a voltage bias is applied across the junction the electrons propagating in a certain direction are accelerated. Upon Andreev reflection they transformed into holes with are also gaining energy while travelling in the opposite direction. At each of these cycles the quasiparticles gain an energy $2eV$. Thus, a quasiparticle from the edge of the continuum below the Fermi energy require $eV/2\Delta$ reflection to escape the weak-link.

current flowing through a junction is very general, it does not provide a small closed form expression of the current, even for the simple SNS junctions. In the low voltage limit, when $|V| \ll |\Delta|$, as the number of reflections is large, the states of the junction can be described by the occupation of the Andreev bounds states which change under the effect of non-adiabatic processes induced by the rapid phase shift.

2.2.4.4 Quasi-adiabatic regime of SNS junctions

The Andreev bound states occupations can be described using a stochastic model. At $\varphi = 0 \mod 2\pi$ the bound states merge with the continuum, see fig. 2.10, thus the lower state is empty while the higher one is occupied. Until $\varphi = \pi \mod 2\pi$ nothing is expected to change, if we neglect all relaxation mechanisms and other parasitic effects. At $\varphi = \pi$ a Landau-Zener transition is induced by the phase shift with a probability p_π set by the following relation, see [25]

$$p_\pi = \exp\left(-\frac{\pi\Delta}{eV}(1-T)\right). \tag{2.80}$$

Hence, at each cycle of the phase, either the transition does not happen , and the current cancel out, either an effective charge q_* is transferred

$$q_* \equiv \frac{2e}{\hbar}\int_0^{2\pi/\omega_J}\left(\Theta(\pi-\varphi(t))\frac{\mathrm{d}E_-(\varphi)}{\mathrm{d}t} + \Theta(\varphi(t)-\pi)\frac{\mathrm{d}E_+(\varphi)}{\mathrm{d}t}\right)\mathrm{d}t, \tag{2.81}$$

where we set $\varphi(0) = 0$.This expression can be simplified into

$$q_* = \frac{1}{V}\int_0^{2\pi}\left|\frac{\mathrm{d}E_-(\varphi)}{\mathrm{d}t}\right|\mathrm{d}\varphi, \tag{2.82}$$

In the limit $1-T \ll 1$, we have

$$\boxed{q_* = \frac{2|\Delta|}{V}}. \tag{2.83}$$

The divergence of the effective charge results from the coherent transport occurring within the junction. Regardless of whether a Landau-Zener transition occurs, the initial state of the occupations is restored when the ABS merges back into the continuum at $\varphi = 2\pi$. Thus, the fundamental frequency of the Josephson radiation is ω_J despite the non-adiabatic processes. From the above discussion, it appears that the low frequency charge transfer is a binomial process. Thus, we can swiftly evaluate the low frequency current noise. Considering a time $\delta_t = \frac{2n\pi}{\omega_J}$, the probability that k effective charges cross the junction is set by

$$P(k) = \binom{n}{k} p_\pi^k (1-p_\pi)^{n-k} \tag{2.84}$$

where the binomial coefficient is

$$\binom{n}{k} \equiv \frac{k!}{k!(n-k)!}. \tag{2.85}$$

Therefore, the charge flow statistics are provided by

$$N_{\delta_t} = n p_\pi, \quad \sigma^2_{N,\delta_t} = n p_\pi (1-p_\pi), \tag{2.86}$$

Nowadays, it is possible to measure the low-frequency noise and current flowing through a single channel Josephson junction [42, 43]. This corresponds to measure the direct current I_{DC} and its variance σ_I^2 defined as

$$I_{DC} \equiv \lim_{\delta_t \to +\infty} \left\langle \int_0^{\delta_t} \frac{I(t)}{\delta_t} \mathrm{d}t \right\rangle \tag{2.87}$$

$$\sigma_I^2 \equiv \lim_{\delta_t \to +\infty} \left\langle \int_0^{\delta_t} \left(\frac{I(t)}{\delta_t} \right)^2 \mathrm{d}t \right\rangle - I_{DC}^2 \tag{2.88}$$

Within our model of a highly transparent SNS junction, we have

$$I_{DC} = q_* p_\pi \tag{2.89}$$

$$\sigma_I^2 = q_*^2 p_\pi (1-p_\pi) \tag{2.90}$$

Fano factor *Considering a random variable w of mean μ_w and variance σ_w^2 its Fano factor is defined as*

$$F_w = \frac{\sigma_w^2}{\mu_w}. \tag{2.91}$$

Thus, by measuring the Fano factor F^* one obtains the effective charge

$$F_* = \frac{\sigma_I^2}{I_{DC}} = \left(1-p_\pi\right) \frac{2\Delta}{V}. \tag{2.92}$$

Hence, at low voltage $V \ll (1-T)\pi\Delta/e$, the transition probability p_π vanishes. Yet, the Fano factor, that is the ratio of the noise power to the average current, diverges as V^{-1}. This results from the interplay between the coherent transport in the junction building up a large effective charge and the stochastic dynamics

induced by the Landau-Zener transitions. We shall emphasize that this formula does not hold at extremely low voltage, where other mechanisms such as relaxations interfere [25, 44, 45]. The normalized Fano factor $F = F_*/q_*$ permits to analyse the statistic of charge transfers. When the Landau-Zener probability is very small $p_\pi \ll 1$, the successive charge transfers are uncorrelated. Thus, they are described by a Poisson process and the normalized Fano factor is equal to unit ($F = 1$), whereas in the opposite limit, when $1 - p_\pi \ll 0$, the transfers are fully deterministic.

This concludes the overview of the short SNS junctions. In the following, we will consider a junction in which the normal metal weaklink is replaced by a quantum dot and will describe the spectrum of such a junction.

2.2.5 SQDS junctions

We consider a junction made of a spin-degenerate single-level quantum dot that is contacted to two superconducting leads. Its Andreev spectrum has been analysed both in the presence and absence of Coulomb interaction [20–22]. Let us first start with the non-interacting situation. As in the case of SNS junction, the junction accommodates two particle-hole symmetric ABSs denoted $|+\rangle$ and $|-\rangle$. By trapping the quasiparticle in the dot, we restore the energy dependence of the scattering matrices. Thus, the link between the superconductors is now described by the matrix $\mathbf{S_{QD}}$

$$\mathbf{S_{QD}} = \begin{pmatrix} \mathbf{S_e}(E) & 0 \\ 0 & \bar{\mathbf{S}}_\mathbf{e}(-E) \end{pmatrix}, \quad \mathbf{S_e} = \begin{pmatrix} -ir(E) & t(E) \\ t(E) & -ir(E) \end{pmatrix}, \tag{2.93}$$

Thus, the junction spectrum is solution of the equation

$$\det\left\{\mathbf{S_A(E)S_{QD}}(E) - \mathbb{1}\right\} = 0. \tag{2.94}$$

Without any additional assumption about the form of the coefficients, we derive a first equation

$$\cos(\zeta(E)) + \cos(\varphi)|t(-E)t(E)| + \sqrt{|r(-E)r(E)|} = 0, \tag{2.95}$$

where

$$\zeta(E) = \arg t(E) - \arg t(-E) + 2\arcsin(E/|\Delta|). \tag{2.96}$$

Hence, close to the Fermi energy, this equation reduces to the one obtained for the SNS junction

$$\frac{E_\pm(\varphi)}{|\Delta|} \approx \pm\sqrt{1 - |t(0)|^2 \sin^2(\varphi/2)} \quad \text{at } \phi \approx \pi. \tag{2.97}$$

To further investigate the Andreev bound states spectrum of this junction, we need the scattering matrix of the non-interacting quantum dot. Let $r_{\mathrm{R/L}}$ and $t_{\mathrm{R/L}}$ be the transmission and reflection coefficients associated to the tunnelling from the right and left leads in normal state to the quantum-dot, we suppose that they do not depend on the energy. We also introduce the phase shift $\chi(E)$ induced by travelling through the dot. To evaluate the whole transmission, let's consider a wave at energy E travelling from left to right. It can follow different paths which differ by the numbers of reflections that occur within the quantum dot. The particle first has to cross the left barrier, this is associated to the coefficient t_L. Then it travels back and forth across the quantum dot, at each round trip, its amplitude gains a factor $r_\mathrm{L} r_\mathrm{R} \exp(2i\chi(E))$. Finally, it crosses the right barrier. By summing coherently all these processes, we obtain the junction transmission $t(E)$

$$t(E) = t_\mathrm{L} t_\mathrm{R} e^{i\chi(E)} \sum_{k=0}^{\infty} \left[r_\mathrm{L} r_\mathrm{R} \exp(2i\chi(E))\right]^k \tag{2.98}$$

$$= \frac{t_\mathrm{L} t_\mathrm{R} e^{i\chi(E)}}{1 - r_\mathrm{L} r_\mathrm{R} e^{2i\chi(E)}}. \tag{2.99}$$

Upon absorbing the reflection phase shifts in the definition of $\chi(E)$, so that $r_{\mathrm{R/L}} \in \mathbb{R}^+$, the transmission probability $T = |t|^2$ can be cast as

$$T = \frac{T_{\mathrm{L}} T_{\mathrm{R}}}{1 + R_{\mathrm{L}} R_{\mathrm{R}} - 2\sqrt{R_{\mathrm{L}} R_{\mathrm{R}}} \cos\big(2\chi(E)\big)}, \tag{2.100}$$

where $T_{\mathrm{L/R}} = |t_{\mathrm{L/R}}|^2$ and $R_{\mathrm{L/R}} = |r_{\mathrm{L/R}}|^2$ are the transmission and reflection probabilities associated to the tunnel coupling. Following [38], we may focus on a single resonance at energy ϵ_0 and develop the phase shift as

$$\chi(E) = \frac{E - \epsilon_0}{2W}, \tag{2.101}$$

where W is of the magnitude of the distance between successive resonances. By developing $T(E)$ around ϵ_0 we finally obtain

$$T = \frac{\Gamma_{\mathrm{L}} \Gamma_{\mathrm{R}}}{((\Gamma_{\mathrm{L}} + \Gamma_{\mathrm{R}})/2)^2 + (E - \epsilon_0)^2}, \tag{2.102}$$

where we defined the tunnelling rate $\Gamma_{L/R}/\hbar \equiv W\, T_{\mathrm{L/R}}/\hbar$. The quantum-dot transmission around a resonance has thus a Lorentzian shape of energy width $\Gamma_L + \Gamma_R$ and amplitude $4\Gamma_{\mathrm{L}}\Gamma_{\mathrm{R}}/(\Gamma_{\mathrm{L}} + \Gamma_{\mathrm{R}})^2$. Hence, when the junction is symmetric, *i.e.* when $\Gamma_L = \Gamma_R$, the transmission at resonance is perfect. By inserting the expression of $r(E)$ and $t(E)$ in eq. (2.95) one obtains the following equation, see [46]

$$\Omega(E) + \Gamma E^2 \sqrt{|\Delta^2| - E^2} = 0, \tag{2.103}$$

where $\Omega(E)$ is defined by

$$\Omega(E) = (|\Delta|^2 - E^2)(E^2 - \epsilon_0^2 - \frac{1}{4}\Gamma^2) + |\Delta|^2 \Gamma_L \Gamma_R \sin^2\left(\frac{\varphi}{2}\right), \tag{2.104}$$

To determine the position of the spectrum extrema we introduce the function $f(\epsilon, \varphi)$ defined by

$$f(\epsilon, \varphi) = \Omega(\epsilon, \varphi) + \Gamma \epsilon^2 \sqrt{|\Delta|^2 - \epsilon^2} \tag{2.105}$$

The bounds states satisfy $f(E_{ABS}(\varphi), \varphi) = 0$, thus we have

$$\frac{\mathrm{d}E_{ABS}}{\mathrm{d}\varphi} = -\frac{\mathrm{d}f}{\mathrm{d}\varphi} \Big/ \frac{\mathrm{d}f}{\mathrm{d}\epsilon}\bigg|_{\epsilon = E(\varphi)} \tag{2.106}$$

which implies that

$$\frac{\mathrm{d}E_{ABS}}{\mathrm{d}\varphi} \propto \sin\big(\varphi\big) \tag{2.107}$$

Thus the extrema are located at $\varphi \equiv 0 \mod \pi$. While at $\varphi = \pi$ the SQDS junction has the same behaviour as the SNS junction, the situation is different at $\varphi = 0$ where gaps form between the discrete states and the continuum, see fig. 2.13. When the junction is almost symmetric and $\Delta \ll \Gamma$, $|\epsilon_0| \ll |\Delta|$, we can estimate the size of the gap

$$1 - \frac{|E_{ABS}\big(\varphi = 0\big)|}{|\Delta|} = \frac{8|\Delta|^2}{\Gamma^2} + O\left(\frac{|\Delta|^4}{\Gamma^4}\right). \tag{2.108}$$

Under the same assumption, one can approximate the ABS energies by

$$E_{\pm}(\varphi) = \pm\Delta\sqrt{T_0 \cos^2(\varphi/2) + R_\pi \sin^2(\varphi/2)}, \tag{2.109}$$

where the $R_\pi \equiv 1 - T_\pi$ is the junction reflection probability at the Fermi energy

$$T_\pi = \frac{\Gamma_{\mathrm{L}} \Gamma_{\mathrm{R}}}{((\Gamma_{\mathrm{L}} + \Gamma_{\mathrm{R}})/2)^2 + \epsilon_0^2}, \tag{2.110}$$

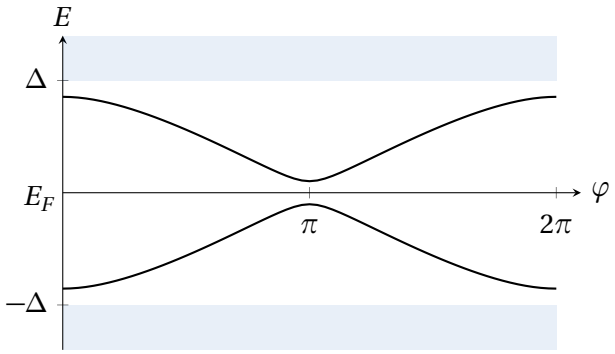

Figure 2.13: Spectrum of a slightly dissymmetric S-QD-S junction, the parameters are $\epsilon_0 = 0.4|\Delta|$, $\delta\Gamma = 0.2|\Delta|$. We observe the detachment of the Andreev bound states from the continuum at all phase differences.

and T_0 is an effective transmission probability that can be estimated from eq. (2.108) to be of the same magnitude as $|\Delta|^2/\Gamma^2$. Interestingly, Eq. (2.109) also holds in the presence of a strong Coulomb interaction [23, 47] when the junction is almost symmetric and the gap is small compared to the Kondo temperature $\Delta \ll T_K$ after substituting Γ with $T_K \gg \Delta$ in the estimate for R_0 (up to a logarithmic correction [48]), setting ϵ_0 to 0 and renormalizing the parameters $\Gamma_{L/R}$.

The gaps that detach the Andreev bound states from the continuum at all phase differences is responsible for the qualitative changes in the non-adiabatic Josephson radiation as it permit complex dynamics of the Andreev bound state occupations. Indeed, these occupations are not reset any more when $\varphi \equiv 0 \mod 2\pi$. Furthermore, Interferences between successive non-adiabatic processes may occur [24]. In the following chapter we propose a stochastic model of the bound state occupations.

CHAPTER 3

Markov dynamics

This chapter explores the out-equilibrium occupation dynamics of the Andreev bound states that are developed in a junction made of a quantum dot coupled to two conventional superconductors. Hereafter, we consider that the interaction with the environment is strong enough to suppress any coherence effect, the ABS dynamics is thus described by a Markov equation. We will derive the average occupation of the different states and the associated correlation function. Analysing the finite-frequency noise, we find that the model may exhibit either an integer or a fractional AC Josephson effect, depending on the bias voltage and the size of the gaps in the Andreev spectrum.

3.1 Stochastic model

We consider a junction made of a spin-degenerate single-level quantum dot that is contacted to two superconducting leads. For an almost symmetric coupling, when the transmission is almost ballistic, $R_\pi \equiv 1 - T_\pi \ll 1$, the junction accommodates two particle-hole symmetric ABS denoted $|+\rangle$ and $|-\rangle$. Their energies are approximated by

$$E_\pm(\varphi) = \pm\Delta\sqrt{T_0\cos^2(\varphi/2) + R_\pi \sin^2(\varphi/2)}. \tag{3.1}$$

The ABS dispersion is illustrated in fig. 3.1. We turn now to the current flowing through the junction. Each

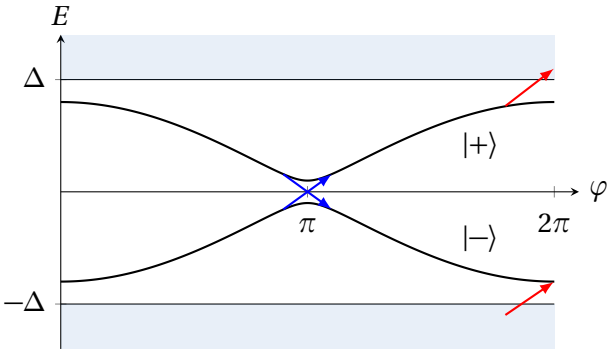

Figure 3.1: Spectrum of the Andreev bound states as a function of the superconducting phase difference. In the presence of a voltage bias, the phase increases with time and non-adiabatic transitions may occur between states $|+\rangle$ and $|-\rangle$ (blues arrows), as well as between state $|+\rangle$ and the continuum at energy $E > \Delta$ or between the continuum at energy $E < -\Delta$ and state $|-\rangle$ (red arrows).

occupied ABS carries a supercurrent

$$I_{\pm}(\varphi)=\frac{2e}{\hbar}\frac{\partial E_{\pm}(\varphi)}{\partial\varphi}\approx\mp I_J\sin\frac{\varphi}{2}\mathrm{sign}\left(\cos\frac{\varphi}{2}\right), \tag{3.2}$$

where $I_J=e\Delta/\hbar$, and we used $R_0,R_\pi\ll 1$ in the last equality. In equilibrium, the average ABS occupations are set by the Fermi distribution, while the contribution of the continuum is negligibly small. Thus, the equilibrium supercurrent at zero temperature is given by $I_-(\varphi)$. In the presence of a DC voltage bias, the phase difference increases linearly with time, $\varphi(t)=\omega_J t+\varphi_0$ with a reference phase φ_0. (Here we assume $V>0$, for concreteness.) As a consequence, changes in the occupations of the ABS can occur due to non-adiabatic transitions. Using $R_0,R_\pi\ll 1$ and $V\ll\Delta/e$, we can isolate two kinds of non-adiabatic processes. Near $\varphi=\pi \bmod 2\pi$, these are the transitions between $|+\rangle$ and $|-\rangle$, which occur with the Landau-Zener probability $p_\pi=\exp(-\pi R_\pi\Delta/eV)$ [49]; p_π increases rapidly from 0 to 1 as V increases in the vicinity of $V_\pi=R_\pi\Delta/e$. Near $\varphi=0 \bmod 2\pi$, these are non-adiabatic transitions between $|+\rangle$ and the continuum states with energy $E>\Delta$ as well as the continuum states with energy $E<-\Delta$ and $|-\rangle$ [24], which take place with probability $p_0=p(V/V_0)$ with $V_0=R_0^{3/2}\Delta/e$, where the function $p(x)$ calculated in Ref. [50] (and Ref. [24] at $V\ll V_0$) is such that p_0 increases rapidly from 0 to 1 as V increases in the vicinity of V_0. We assume $T\ll\Delta$, so that continuum states with energy $E<-\Delta$ ($E>\Delta$) are occupied (empty). We also neglect the short timescales over which the non-adiabatic processes take place on the scale of the Josephson period, $2\pi/\omega_J$. Then at each time, the state of the junction is fully characterized by the occupations $n_\pm=0,1$. (In particular, we ignore coherent superpositions between $|\pm\rangle$-states.) The states $(0,1)$ and $(1,0)$ are the ground and first excited states in the even parity sector of the junction, respectively; the states $(0,0)$ and $(1,1)$ are the "poisoned" states in the odd parity sector [51]. These last states are degenerate [1]. Within a Markov model that describes switches in their random occupations [44, 50], the average supercurrent is

$$\langle I(t)\rangle=\mathscr{I}(t)\big[P_{01}(\varphi(t))-P_{10}(\varphi(t))\big]. \tag{3.3}$$

Here $\mathscr{I}(t)=I_-\big(\varphi(t)\big)$ and $P_{n_+n_-}(\varphi)$ with $n_+,n_-=0,1$ denotes the ABS occupations at a given phase. Neglecting any coupling with an external bath, these probabilities remain constant within intervals $\pi m<\varphi<\pi(m+1)$ with m integer, while their values immediately before and after the specific phases where non-adiabatic transitions can take place are related with each other through the transition probabilities p_π and p_0,

$$\boldsymbol{P}((2m+1)\pi^+)=\mathscr{L}_\pi\boldsymbol{P}((2m+1)\pi^-), \tag{3.4a}$$

$$\boldsymbol{P}(2m\pi^+)=\mathscr{L}_0\boldsymbol{P}(2m\pi^-) \tag{3.4b}$$

with $\boldsymbol{P}(\varphi)=\big(P_{11}(\varphi),P_{10}(\varphi),P_{01}(\varphi),P_{00}(\varphi)\big)^T$ and the transition matrices

$$\mathscr{L}_\pi=\begin{pmatrix}1&0&0&0\\0&1-p_\pi&p_\pi&0\\0&p_\pi&1-p_\pi&0\\0&0&0&1\end{pmatrix}, \tag{3.5a}$$

$$\mathscr{L}_0=\begin{pmatrix}1-p_0&p_0(1-p_0)&0&0\\0&(1-p_0)^2&0&0\\p_0&p_0^2&1&p_0\\0&p_0(1-p_0)&0&1-p_0\end{pmatrix} \tag{3.5b}$$

The non-adiabatic processes accounted for by the matrix elements of $\mathscr{L}_\pi$ and $\mathscr{L}_0$ are illustrated in fig. 3.2(b) and fig. 3.2(c). Before evaluating the full current noise spectrum , we shall explore the low frequencies $\omega\ll\omega_J$ behaviour of this system by integrating out the high frequency dynamics.

[1] The states (0,0) and (1,1) carry zero current (see eq. (3.42)) and have the same incoming and out-coming probabilities (see fig. 3.2 (c)). Hence, an alternative model not distinguishing these states could be formulated. However, it would be unsuited for the comparison with topological junctions (see section 3.4).

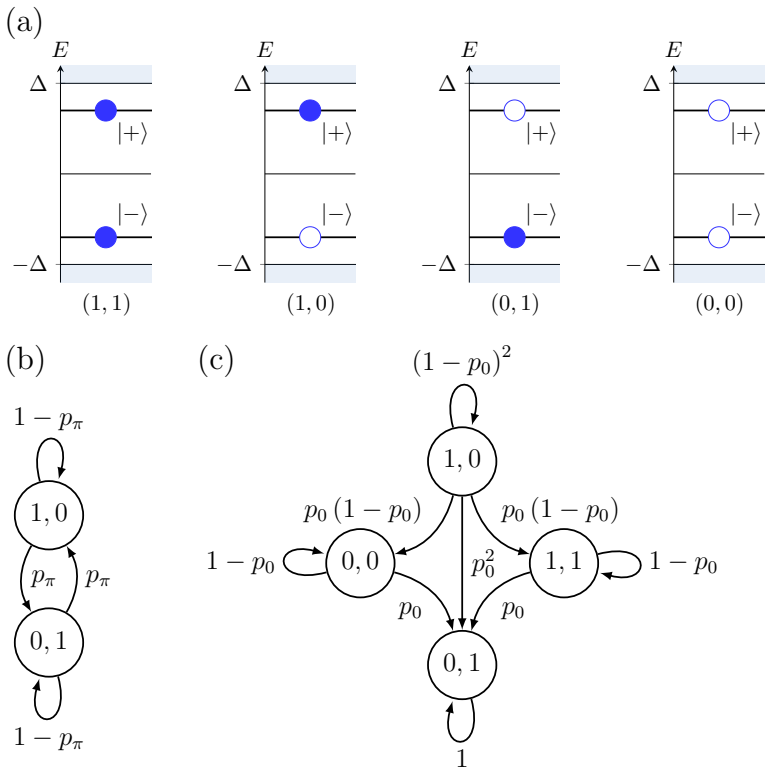

Figure 3.2: (a) The junction state is characterized by the occupations of the two Andreev bound states. Filled and unfilled circles, depict occupied and unoccupied Andreev bound states. (b)-(c) Graphs of the transition matrices. Each arrow denotes a possible transition between two states (n_+, n_-) and (n'_+, n'_-), and is labelled by the transition probability.(b) non-adiabatic processes described by $\mathscr{L}_\pi$ can exchange the occupation of states $(0,1)$ and $(1,0)$ by enabling a particle from one ABS to jump to the other ABS. (c) non-adiabatic processes described by $\mathscr{L}_\mathbf{0}$ can populate the lower ABS, enabling transitions from $(0,0)$ to $(0,1)$, and from $(1,0)$ to $(1,1)$. They can also deplete the higher ABS state, enabling transitions from $(1,0)$ to $(0,0)$ and from $(1,1)$ to $(0,1)$. As the changes of the population of the lower and upper ABS are independent, the total transition probabilities indicated in the figure are a product of two probabilities.

3.2 Low frequency model

The initial Markov chain eq. (3.5) is not stationary. But once the high frequency $\omega \gtrsim \omega_J$ is integrated out, the resultant model is stationary. This greatly simplify the derivation of the low frequency current statistic.

3.2.1 Averaging out the high frequencies

Considering a τ-periodic Markov chain associated to the probabilities $p(t) = (p_1, p_2, ..., p_N)$, it is possible to formulate a stationary low frequency model where the dynamics on timescales shorter than τ are averaged out. The probability vector satisfies

$$\frac{\mathrm{d}p(t)}{\mathrm{d}t} = \mathbf{M}(t)p(t), \tag{3.6a}$$

$$\mathbf{M}(t+\tau) = \mathbf{M}(t), \tag{3.6b}$$

where $\mathbf{M}(t)$ is a Markov matrix, *id est* all its entries are positive numbers and the sum of each column is equal to 1. We introduce the associated retarded Green function $\mathscr{L}(t,t')$ that vanishes for $t' < t$ and is defined for $t > t'$ by:

$$p(t) = \mathscr{L}(t,t')p(t'), \tag{3.7}$$

where $p(t)$ is any probability vector that satisfy the master equation $eq.$ (3.6b). One might show that the Green function satisfies the following differential equation

$$\left\{\frac{\mathrm{d}}{\mathrm{d}t}-\mathbf{M}(t)\right\}\mathscr{L}(t,t')=\delta(t,t') \tag{3.8}$$

From the definition $\mathscr{L}(t,t')$, we have

$$p(n\tau+\tau)=\mathscr{L}(n\tau+\tau,n\tau)p(n\tau) \tag{3.9}$$

Using the periodicity of the Markov chain, we simplify this last expression to

$$p((n+1)\tau)=\mathscr{L}(\tau,0)p(n\tau). \tag{3.10}$$

Hence, the vector $p_\tau(n)\equiv p(n\tau)$ obeys the time independent Markov equation:

$$p_\tau(n+1)=\mathscr{L}(\tau,0)p_\tau(n) \tag{3.11}$$

While the short times scales properties of the initial model are lost, this new effective model provides an efficient method to access long timescale quantities. This method can be directly applied to the junction model. The retarded Green function of the equation eq. (3.4) for $\varphi\in[0,2\pi]$ is

$$\mathscr{L}(\varphi,0^+)=\begin{cases}\mathbb{1} & \varphi<\pi\\ \mathscr{L}_\pi & \pi\le\varphi<2\pi\\ \mathscr{L}_0\mathscr{L}_\pi & \varphi=2\pi\end{cases} \tag{3.12}$$

Hence, $\mathscr{L}\equiv\mathscr{L}(2\pi,0^+)=\mathscr{L}_0\mathscr{L}_\pi$. In the same basis than eq. (3.5) we have

$$\mathscr{L}=\begin{pmatrix}1-p_0 & p_0(1-p_0)(1-p_\pi) & p_0p_\pi(1-p_0) & 0\\ 0 & (1-p_0)^2(1-p_\pi) & p_\pi(1-p_0)^2 & 0\\ p_0 & p_0^2(1-p_\pi)+p_\pi & p_0^2p_\pi-p_\pi+1 & p_0\\ 0 & p_0(1-p_0)(1-p_\pi) & p_0p_\pi(1-p_0) & 1-p_0\end{pmatrix} \tag{3.13}$$

Under careful examination, it appears that a charge is transferred across the system during a period if and only if a Landau Zener transition occurs. In the other cases, due to the Andreev bound state energy symmetries, the current averaged to 0 over a period. Thus, as for SNS junction section 2.2.4.3, we just have to count the number of charges that effectively cross the junction.

3.2.2 Counting field method

The counting field method permits to keep track of a quantity that changes under transition of the Markov chain but is not included in the state definition. In our problem, the state are defined by the occupation of the ABS, yet to evaluate the current we must count the particle transfers. Let's consider a system describe by a finite Markov chain

$$p(n+1)=\mathbf{\Gamma}p(n). \tag{3.14}$$

The probability vector should be normalized $\sum_i p_i(n)=1$. To conserve this normalization, $\mathbf{\Gamma}$ must be a stochastic matrix, *i.e.* $\sum_j \Gamma_{ij}=1$. We are interested in the statistics of an observed variable $\hat{N}(n)$. Each transition $s\to s'$ change this quantity by a fixed amount $N_{s's}$. We introduce the probability $p_s(N,n)$ to be in the state s at step n with $\hat{N}(n)=N$. The transfer matrix is rewrite as $\mathbf{\Gamma}=\sum_q\mathbf{\Gamma}_q$. Where the transition included in $\mathbf{\Gamma}_q$ increase the value of $\hat{N}$ by q. Thus, we have

$$p(N,n+1)=\sum_{q=-\infty}^{\infty}\mathbf{\Gamma}_q p(N-q,n). \tag{3.15}$$

We exploit the independence of $\mathbf{\Gamma}$ with respect to the number of counted particles by introducing the Fourier transform

$$\rho_s(\chi, n) = \sum_{N=-\infty}^{+\infty} p_s(N, n) e^{iN\chi}. \tag{3.16}$$

Thus, equation eq. (3.15) takes the following form

$$\rho(\chi, \tau+1) = \left(\sum_{q=-\infty}^{\infty} \mathbf{\Gamma}_q e^{iq\chi} \right) \rho(\chi, \tau). \tag{3.17}$$

Writing $\tilde{\Gamma}_{p,q}(\chi) = \Gamma_{p,q} \cdot e^{iN_{p,q}\chi}$, we have

$$\rho(\chi, \tau+1) = \tilde{\mathbf{\Gamma}}(\chi)\rho(\chi, \tau). \tag{3.18}$$

Solving this trivial recurrence, we get

$$\rho(\chi, \tau) = \tilde{\mathbf{\Gamma}}^n(\chi)\rho(\chi, 0). \tag{3.19}$$

When χ goes to 0, the spectrum of $\tilde{\mathbf{\Gamma}}(\chi)$ converges smoothly to the spectrum of $\mathbf{\Gamma}$. Assuming that $\mathbf{\Gamma}$ admits a unique stationary state and can be diagonalized, there is a unique eigenvalue λ_χ such that $\lambda_\chi \to 1$ when $\chi \to 0$. Hence, when $\chi \ll 1$ and $\tau \gg 1$, from eq. (3.19) we can write

$$\rho(\chi, \tau) \approx \lambda_\chi^n \boldsymbol{Q}_\chi \begin{pmatrix} 1 & & \\ & 0 & \\ & & \ddots \end{pmatrix} \boldsymbol{Q}_\chi^{-1} \rho(\chi, 0). \tag{3.20}$$

Finally, we introduce the characteristic function of $\hat{N}(n)$ which we denote by $\Lambda(\chi, n) = \sum_s \rho_s(\chi, n)$:

$$\Lambda(\chi, \tau) = \lambda_\chi^n h(\chi) \tag{3.21}$$

Where $h(\chi)$ is the function of χ whose expression is not relevant for what follow. We may now introduce the cumulant generative function $C(\chi, n) = \log \Lambda(\chi, n)$. Hence, when $\chi \ll 1$ and $n \gg 1$, we got:

$$\boxed{C(\chi, \tau) = \tau \log(\lambda_\chi)} \tag{3.22}$$

Thus, the cumulant of order p is given by:

$$\boxed{\kappa_p = (-i)^p \frac{\partial^p C(\chi, \tau)}{\partial \chi^p}} \tag{3.23}$$

The firsts cumulants are the mean and standard deviation

$$\kappa_1 = \langle N_\tau \rangle, \quad \kappa_2 = \sigma^2_{N(n)}. \tag{3.24}$$

Using $n \gg 1$ this simplifies to:

$$\langle N_\tau \rangle / \tau = -i \left. \frac{\partial \lambda_\chi}{\partial \chi} \right|_{\chi=0} \tag{3.25}$$

$$\sigma^2_{N_\tau} / \tau = \left. \frac{\partial \lambda_\chi}{\partial \chi} \right|^2_{\chi=0} - \left. \frac{\partial^2 \lambda_\chi}{\partial \chi^2} \right|_{\chi=0} \tag{3.26}$$

These derivatives can be evaluated without computing the eigenvalues of $\tilde{\mathbf{\Gamma}}$. Let's define $F(\chi,\lambda)=\det\left(\tilde{\mathbf{\Gamma}}-\lambda\right)$. Thus λ_χ satisfies the equation $F(\chi,\lambda_\chi)=0$. By taking successive derivatives of this equation with respect to χ we deduce the expression of the derivatives of λ_χ:

$$\lambda'_\chi=-\frac{\partial_{1,0}F(\chi,\lambda_\chi)}{\partial_{0,1}F(\chi,\lambda_\chi)} \tag{3.27}$$

$$\lambda''_\chi=-\frac{\partial_{2,0}F(\chi,\lambda_\chi)+2\lambda'_\chi\partial_{1,1}F(\chi,\lambda_\chi)+\lambda'^2_\chi\partial_{0,2}F(\chi,\lambda_\chi)}{\partial_{0,1}F(\chi,\lambda_\chi)} \tag{3.28}$$

3.2.3 Zero frequency current statistics

To use the counting field method, we first need to identify the different transitions that participate in the charges transport. As in the SNS junctions, a charge is transferred during a phase cycle if and only if a Landau-Zener transition occur at $\varphi=\pi \mod 2\pi$. Thus, we deduce that the low frequency transition matrix augmented by the counting field reads as

$$\tilde{\mathscr{L}}=\mathscr{L}_0\tilde{\mathscr{L}}_\pi, \tag{3.29}$$

with

$$\tilde{\mathscr{L}}_\pi=\begin{pmatrix}1&0&0&0\\0&1-p_\pi&p_\pi e^{iq_*\chi}&0\\0&p_\pi e^{-iq_*\chi}&1-p_\pi&0\\0&0&0&1\end{pmatrix}, \tag{3.30}$$

and $q_*=2\Delta/V$ the effective charge which diverges as the inverse of the bias voltage. Using the previous results, we immediately derive the DC current and its Fano factor

$$I_{DC}=\frac{2}{\pi}\frac{p_0p_\pi}{1-\lambda_3}I_J \quad \text{with} \quad \lambda_3=(1-p_0)(1-2p_\pi) \tag{3.31}$$

The parameters λ_3 will reappear later as an eigenvalue of the transition matrix. I_{DC} relates the dissipative current with non-adiabatic processes through the gaps in the Andreev spectrum. It corresponds to the low-voltage regime of multiple Andreev reflections (MAR). It generalizes formulas derived in superconducting atomic contacts [49] at $p_0=1$, and in topological Josephson junctions [50] at $p_\pi=1$. The Fano factor normalized by the effective charge can be cast into

$$F=\frac{\sigma_I^2}{I_{DC}q_*}=\frac{A+B}{8p_0p_\pi(1-\lambda_3)} \tag{3.32}$$

with

$$A=8p_0p_\pi(1-p_\pi)[1+(1-p_0)^2](1+\lambda_3)/\mathscr{N}, \tag{3.33a}$$

$$B=-16p_\pi p_0(2-p_0)\lambda_3/\mathscr{N}, \tag{3.33b}$$

$$\mathscr{N}=(2-p_0)(1-\lambda_3). \tag{3.33c}$$

The Fano factor permits to distinguish different regimes of the junction dynamics. At $p_\pi\ll p_0$, when the bottleneck for the transfer of quasiparticles across the junction is the gap near the Fermi level, $F=1$. This indicates that charge transfer can be described as a Poisson process. The region where $F=1/2$ corresponds approximately to $p_\pi\gtrsim 0.5$ and $p_0\ll 1$, then the transfer process is limited by two gaps of same width near the edges of the continuum spectrum. This halving of the Fano factor might be interpreted as a halving of the effective charge. In particular, at $p_\pi=1$, one recovers the results of Ref. [50] for a topological junction, see section 3.4. F vanishes at $1-p_0,1-p_\pi\ll 1$, when quasiparticle transfer across the gap becomes deterministic. In the general case $0<F<1$, see fig. 3.3.

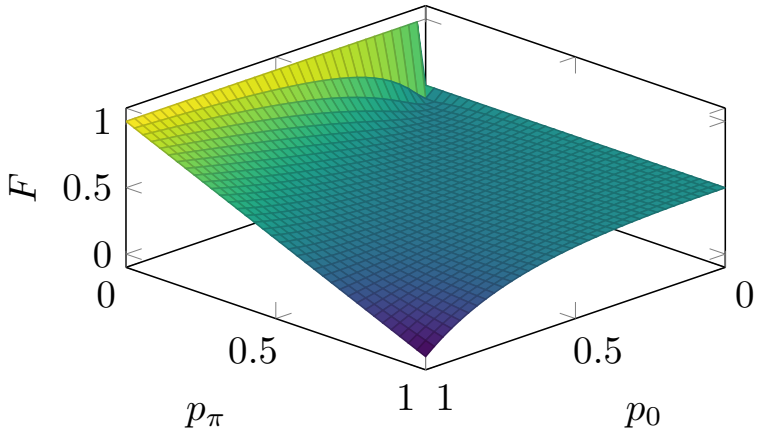

Figure 3.3: The Fano factor as a function of p_0 and p_π.

3.3 Finite frequency current statistics

We now turn to the evaluation of the finite frequency current noise spectrum. While the calculations are rather simple, deriving the finite frequency noise expression is a long trek. We start by considering the stochastic matrix describing a full phase cycle $\mathscr{L} \equiv \mathscr{L}_0 \mathscr{L}_\pi$. It admits normalized right and left-eigenvectors u_α and v_α, with a common eigenvalue λ_α, such that $\mathscr{L} u_\alpha = \lambda_\alpha u_\alpha$, $\mathscr{L} v_\alpha = \lambda_\alpha v_\alpha$, and $v_\alpha^T u_\beta = \delta_{\alpha\beta}$. Furthermore, the eigenvalue $\lambda_0 = 1$ is associated with the left eigenvector $v_0 = (1,\dots,1)^T$, while other eigenvalues, $\lambda_1 = 1-p_0$, $\lambda_2 = (1-p_0)^2$, and $\lambda_3 = (1-p_0)(1-2p_\pi)$, satisfy $|\lambda_{\alpha\neq 0}| < 1$. Thus, the probability vector $\boldsymbol{P}$ that solves eq. (3.4) reaches a solution at long times that does not depend on the initial condition; it is given by the eigensolution $\alpha = 0$:

$$\boldsymbol{P}(\varphi) = \begin{cases} u_0, & 2m\pi < \varphi < (2m+1)\pi, \\ \mathscr{L}_\pi u_0, & (2m+1)\pi < \varphi < (2m+2)\pi, \end{cases} \tag{3.34}$$

with

$$u_0 = \frac{1}{\mathscr{N}} \begin{pmatrix} p_\pi(1-p_0) \\ p_\pi(1-p_0)^2 \\ \mathscr{N} - p_\pi(1-p_0)(3-p_0) \\ p_\pi(1-p_0) \end{pmatrix}, \tag{3.35a}$$

$$\mathscr{L}_\pi u_0 = \frac{1}{\mathscr{N}} \begin{pmatrix} p_\pi(1-p_0) \\ p_\pi \\ \mathscr{N} - p_\pi(3-2p_0) \\ p_\pi(1-p_0) \end{pmatrix}, \tag{3.35b}$$

and $\mathscr{N} = (2-p_0)(1-\lambda_3)$. In particular, the ground state $(0,1)$ is mostly occupied with $u_0 \approx \mathscr{L}_\pi u_0 \approx (0,0,1,0)^T$ at $p_\pi \ll p_0$, while all states are approximately equally occupied with $u_0 \approx \mathscr{L}_\pi u_0 \approx (\frac{1}{4},\frac{1}{4},\frac{1}{4},\frac{1}{4})^T$ at $p_0 \ll p_\pi$. Inserting eq. (3.34) into eq. (3.3), we find the average current in the long-time limit,

$$\begin{aligned} \langle I(t)\rangle &= \frac{p_0}{1-\lambda_3}\big[p_\pi |\mathscr{I}(t)| + (1-p_\pi)\mathscr{I}(t)\big] \\ &= I_{\mathrm{DC}}\left\{1 - \sum_{n\geq 1} \frac{2}{4n^2-1}\Big[\cos\big(n\varphi(t)\big) + 2(-1)^n n \frac{1-p_\pi}{p_\pi}\sin\big(n\varphi(t)\big)\Big]\right\}. \end{aligned} \tag{3.36}$$

The ratio between cosine and sine harmonics of the Josephson frequency is controlled by non-adiabatic transitions between ABS with positive and negative energies. When these processes are rare, the sine harmonics dominate like in the adiabatic case.

3.3.1 Evaluation of the current noise spectrum

Due to the stochastic nature of the non-adiabatic processes, the current fluctuates. We characterize the fluctuations with the current noise spectrum,

$$S(\omega)=2\int_0^\infty d\tau\cos(\omega\tau)\overline{S(t+\tau/2,t-\tau/2)}, \tag{3.37}$$

where the bar denotes an average over t. Within the Markov theory, we relate the current correlator,

$$S(t_1,t_2)=\langle I(t_1)I(t_2)\rangle-\langle I(t_1)\rangle\langle I(t_2)\rangle, \tag{3.38}$$

with

$$\langle I(t_1)I(t_2)\rangle=\mathscr{I}(t_1)\mathscr{I}(t_2)\times\sum_{n_1,n_2}(-1)^{n_1+n_2}P_{n_1\bar{n}_1|n_2\bar{n}_2}(\varphi_1|\varphi_2)P^{\infty}_{n_2\bar{n}_2}(\varphi_2) \tag{3.39}$$

at $t_1>t_2$. Here $P_{n_1n_1'|n_2n_2'}(\varphi_1|\varphi_2)$ with $\varphi_i=\varphi(t_i)$ is the conditional probability for the system to reside in state (n_1,n_1') at phase φ_1 if it was in state (n_2,n_2') at phase $\varphi_2<\varphi_1$; it solves the same eq. (3.4) as the probability $P_{n_1n_1'}(\varphi_1)$, together with the initial condition $P_{n_1n_1'|n_2n_2'}(\varphi_2|\varphi_2)=\delta_{n_1,n_2}\delta_{n_1',n_2'}$. Thus, it is the retarded Green function of this equation. Furthermore, we used the notations $\bar{0}=1$ and $\bar{1}=0$. Using a matrix representation [in the same basis of states as the one used in eq. (3.4) and eq. (3.5)] for the closure relation, $\sum_\alpha u_\alpha v_\alpha^T=1$, we find

$$P(\varphi_1|\varphi_2)=\mathscr{L}_\pi^{k_1}\left(\sum_\alpha u_\alpha\lambda_\alpha^{m_1-m_2}v_\alpha^T\right)\mathscr{L}_\pi^{-k_2} \tag{3.40}$$

for $(2m_i+k_i)\pi<\varphi_i<(2m_i+k_i+1)\pi$ with m_i integer, $k_i=0,1$, and $i=1,2$. The second term in the r.h.s. of eq. (3.38) compensates the contribution from the terms with $\alpha=0$ when inserting eq. (3.40) into eq. (3.39). Furthermore, the expectation value of the current operator in the states with $\alpha=1,2$ vanishes. Therefore, only the terms with $\alpha=3$ contribute to eq. (3.38). Combining eq. (3.38), eq. (3.39) and eq. (3.40), one obtains the following expression for the noise:

$$S(t_1,t_2)=\mathscr{I}(t_1)\mathscr{I}(t_2)\sum_{\alpha=1}^{3}v_0^T\hat{\mathscr{I}}\mathscr{L}_\pi^{k_1}u_\alpha\lambda_\alpha^{m_1-m_2}v_\alpha^T\mathscr{L}_\pi^{-k_2}\hat{\mathscr{I}}\mathscr{L}_\pi^{k_2}u_0, \tag{3.41}$$

Here $\hat{\mathscr{I}}$ is the current operator, which in the basis of eq. (3.4) and eq. (3.5) takes the form

$$\hat{\mathscr{I}}=\begin{pmatrix}0&0&0&0\\0&-1&0&0\\0&0&1&0\\0&0&0&0\end{pmatrix}. \tag{3.42}$$

To evaluate the noise, the left and right eigenvectors of the stochastic matrix $\mathscr{L}$ are needed. The right eigenvector u_0, describing the stationary state is given by eq. (3.35), whereas the others read as follows:

$$u_1=\begin{pmatrix}1\\0\\0\\-1\end{pmatrix},\qquad u_2=\begin{pmatrix}1\\-1\\-1\\1\end{pmatrix},\qquad u_3=\begin{pmatrix}p_0(1-2p_\pi)\\-2p_\pi(1-p_0)\\-2p_0+2p_\pi(1+p_0)\\p_0(1-2p_\pi)\end{pmatrix}. \tag{3.43}$$

One notes that the eigenvectors u_1 and u_2 do not carry any current, $v_0^T\hat{\mathscr{I}}u_{1,2}=0$. Furthermore, u_1 and u_2 are eigenvectors not only of $\mathscr{L}$ but also of $\mathscr{L}_\pi$, namely $\mathscr{L}_\pi u_{1,2}=u_{1,2}$, which further yields $v_0^T\hat{\mathscr{I}}\mathscr{L}_\pi u_{1,2}=0$. As a consequence, the expression for the noise reduces to

$$S(t_1,t_2)=\mathscr{I}(t_1)\mathscr{I}(t_2)\lambda_3^{m_1-m_2}\left(v_0^T\hat{\mathscr{I}}\mathscr{L}_\pi^{k_1}u_3\right)\left(v_3^T\mathscr{L}_\pi^{-k_2}\hat{\mathscr{I}}\mathscr{L}_\pi^{k_2}u_0\right). \tag{3.44}$$

Only the eigenvalue λ_3 contributes to the current fluctuation. Thus, there is a unique timescale for the decay of correlations. This can be linked to the symmetric structure of the transition graph fig. 3.2: for the current flow and the occupation dynamics, the states $(0,0)$ and $(1,1)$ are indistinguishable. In addition to $v_0 = (1,\dots,1)^T$, the only other left eigenvector needed is v_3, given as

$$v_3 = -\frac{1}{2\big(p_0-2p_\pi\big)(1-\lambda_3)}\begin{pmatrix} p_0 \\ 2p_0+2p_\pi(1-p_0) \\ -2p_\pi(1-p_0) \\ p_0 \end{pmatrix}. \tag{3.45}$$

With the expressions provided in eq. (3.43) and eq. (3.45), as well as eq. (3.4) and eq. (3.5), we can evaluate the matrix elements contributing to the noise as given in eq. (3.44). In particular,

$$v_0^T\,\hat{\boldsymbol{\mathcal{I}}}\,u_3 = 2(2p_\pi - p_0), \tag{3.46a}$$

$$v_3^T\,\hat{\boldsymbol{\mathcal{I}}}\,u_0 = \frac{\lambda_3 p_\pi[(1-p_0)(2p_\pi-p_0)-\mathcal{N}]}{\mathcal{N}(p_0-2p_\pi)(1-2p_\pi)(1-\lambda_3)}, \tag{3.46b}$$

$$v_3^T\,\mathcal{L}_\pi^{-1}\,\hat{\boldsymbol{\mathcal{I}}}\,\mathcal{L}_\pi\,u_0 = \frac{p_\pi(2p_\pi-p_0-\mathcal{N})}{\mathcal{N}(p_0-2p_\pi)(1-2p_\pi)(1-\lambda_3)}, \tag{3.46c}$$

$$v_0^T\,\hat{\boldsymbol{\mathcal{I}}}\,\mathcal{L}_\pi\,u_3 = \big(1-2p_\pi\big)\,v_0^T\,\hat{\boldsymbol{\mathcal{I}}}\,u_3. \tag{3.46d}$$

We can now turn to the computation of the noise spectrum $S(\omega)$. As a first step, we rewrite eq. (3.37) as

$$S(\omega) = \lim_{T\to\infty}\frac{2}{T}\int_0^\infty d\tau\,\cos(\omega\tau)\int_0^T dt\,S(t+\tau,t). \tag{3.47}$$

The function $S(t+\tau,t)$ is periodic in t and quasi-periodic in τ with period $T = 2\pi/\omega_J$:

$$S(t+2\pi/\omega_J+\tau, t+2\pi/\omega_J) = S(t+\tau,t), \tag{3.48}$$

$$S(t+\tau+\frac{2\pi}{\omega_J},t) = \lambda_3 S(t+\tau,t). \tag{3.49}$$

Using the periodicity in t, we rewrite the time average as

$$\lim_{T\to\infty}\frac{1}{T}\int_0^T dt\,S(t+\tau,t) = \frac{\omega_J}{2\pi}\int_0^{2\pi/\omega_J} dt\,S(t+\tau,t). \tag{3.50}$$

And by using the quasi-periodicity in τ, we rewrite the Fourier transform as

$$\int_0^\infty d\tau\,\cos(\omega\tau)S(t+\tau,t) = \mathcal{R}\left\{\sum_{n=0}^\infty\big(\lambda_3 e^{2i\pi\omega/\omega_J}\big)^n\int_0^{2\pi/\omega_J} d\tau\,e^{i\omega\tau}S(t+\tau,t)\right\}. \tag{3.51}$$

By combining eq. (3.50) and eq. (3.51), and performing the sum over n, we get

$$S(\omega) = \frac{\omega_J}{\pi}\mathcal{R}\left\{\frac{1}{1-\lambda_3 e^{\frac{2i\pi\omega}{\omega_J}}}\int_0^{2\pi/\omega_J} d\tau\int_0^{2\pi/\omega_J} dt\,e^{i\omega\tau}S(t+\tau,t)\right\}. \tag{3.52}$$

By applying the change of variables $\omega_J t+\varphi_0\to\varphi$ and $\omega_J\tau\to\delta$, we obtain

$$\int_0^{2\pi/\omega_J} d\tau\int_0^{2\pi/\omega_J} dt\,e^{i\omega\tau}S(t+\tau,t) = \frac{1}{\omega_J^2}\int_0^{2\pi} d\delta\int_0^{2\pi} d\varphi\,e^{i\tilde{\omega}\tau}S(\varphi+\delta,\varphi), \tag{3.53}$$

where $\tilde{\omega} = \omega/\omega_J$. To perform the remaining integration, we shall notice that $S(t,t+\tau)$ possesses discontinuities at $\delta+\varphi = n\pi$ and $\varphi = n\pi$. There, the values of the indices m_1-m_2, k_1, and k_2 change in the expression of the noise, eq. (3.44). Thus, the integration domain must be split into different segments.

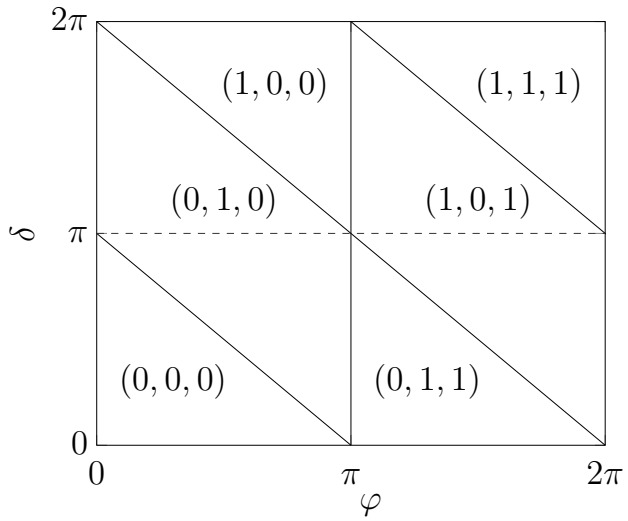

Figure 3.4: Map of the indices (m_1-m_2,k_1,k_2) determining $S(\varphi+\delta,\varphi)$ according to eq. (3.44) as a function of φ and δ. Discontinuities in $S(\varphi+\delta,\varphi)$ appear at the boundaries of the different domains delimited by full lines. The integration scheme introduces additional segments depending on the value of δ, separated by the dashed line.

Once we perform the integration over φ in the eight segments shown in fig. 3.4, we end up with a piecewise continuous function of δ. Integrating over δ and rearranging the terms, we obtain eq. (3.41) with coefficients

$$A = 2(1+\lambda_3)\, v_0^T \hat{\mathscr{I}} u_3 \left\{\left[-2\lambda_3+(1-2p_\pi)(1-\lambda_3)\right] v_3^T \mathscr{L}_\pi^{-1} \hat{\mathscr{I}} \mathscr{L}_\pi u_0 + \left[1-\lambda_3+2(1-2p_\pi)\right] v_3^T \hat{\mathscr{I}} u_0\right\} \tag{3.54a}$$

$$B = 8 v_0^T \hat{\mathscr{I}} u_3 \left[\lambda_3^2 v_3^T \mathscr{L}_\pi^{-1} \hat{\mathscr{I}} \mathscr{L}_\pi u_0 - \left(1-2p_\pi\right) v_3^T \hat{\mathscr{I}} u_0\right] \tag{3.54b}$$

$$C = 32\lambda_3 v_0^T \hat{\mathscr{I}} u_3 \left[v_3^T \mathscr{L}_\pi^{-1} \hat{\mathscr{I}} \mathscr{L}_\pi u_0 - \left(1-2p_\pi\right) v_3^T \hat{\mathscr{I}} u_0\right] \tag{3.54c}$$

Using eq. (3.46), this finally provide the expression

$$\frac{S(\omega)}{S_0} = \frac{A\left[1+4\tilde{\omega}^2-4\tilde{\omega}\sin(\pi\tilde{\omega})\right]+(B+C\tilde{\omega}^2)\cos^2(\pi\tilde{\omega})}{(1-4\tilde{\omega}^2)^2\left[(1+\lambda_3)^2-4\lambda_3\cos^2(\pi\tilde{\omega})\right]} \tag{3.55}$$

with

$$A = 8p_0p_\pi(1-p_\pi)[1+(1-p_0)^2](1+\lambda_3)/\mathscr{N}, \tag{3.56a}$$

$$B = -16p_\pi p_0(2-p_0)\lambda_3/\mathscr{N}, \tag{3.56b}$$

$$C = 128p_\pi(1-p_\pi)(1-p_0)[1-\lambda_3(1-p_0)]/\mathscr{N}, \tag{3.56c}$$

$$S_0 = I_J^2/(\pi\omega_J) \tag{3.56d}$$

We published the above result in [52], yet in the published version, the above coefficient eq. (3.56b) contains a typo that we fixed here. Below we discuss the zero-frequency noise as well as structures related to the AC currents in the finite frequency noise given by eq. (3.55).

3.3.2 Analysis of the finite frequency noise

As it appears in eq. (3.41), the current correlation function decays as $|\lambda_3|^{|\omega_J\tau/2\pi|}$. Thus, the noise is expected to display sharp features when $1-|\lambda_3| \ll 1$. This is confirmed by the final expression eq. (3.55). This happens when $p_0, p_\pi \ll 1$ or $p_0, 1-p_\pi \ll 1$. At $p_0, p_\pi \ll 1$ the noise spectrum displays features with a

narrow linewidth,

$$\gamma = \frac{1}{2\pi}(p_0 + 2p_\pi)\omega_J, \tag{3.57}$$

near $\omega = n\omega_J$ with n integer. In particular, at very low frequency, $\omega \ll \omega_J$,

$$\frac{S(\omega)}{e^\star I_{\rm DC}} = F + (F_{\rm app} - F)\frac{\omega^2}{\omega^2 + \gamma^2}. \tag{3.58}$$

Here, eq. (3.31) simplifies to

$$I_{\rm DC} = \frac{2I_J}{\pi}\frac{p_0 p_\pi}{p_0 + 2p_\pi}, \tag{3.59}$$

and the Fano factor,

$$F = \frac{p_0^2 + p_0 p_\pi + 2p_\pi^2}{(p_0 + 2p_\pi)^2}, \tag{3.60}$$

is only accessible in a narrow frequency range $\omega \ll \gamma$, while an apparent Fano factor,

$$F_{\rm app} = \frac{(12 - 4\pi + \pi^2)p_0 + 8p_\pi}{2\pi^2 p_0}, \tag{3.61}$$

characterizes the noise in a wide frequency range $\gamma \ll \omega \ll \omega_J$. Note that $F_{\rm app} \gg F$ if $p_0 \ll p_\pi$. Furthermore

$$S(\omega) = \frac{32n^2}{(4n^2-1)^2\pi}\frac{(3p_0 + 2p_\pi)p_\pi}{(p_0 + 2p_\pi)^2}\frac{\gamma I_J^2/\pi}{(\omega - n\omega_J)^2 + \gamma^2} \tag{3.62}$$

at $|\omega - n\omega_J| \ll \omega_J$, up to a negative resonance-frequency shift of the order of $\gamma^2/\omega_J \ll \gamma$. Comparing eq. (3.62) with the amplitude of the harmonics in eq. (3.36), we conclude that the Josephson radiation at $p_0 \ll p_\pi \ll 1$ is dominated by the noise, eq. (3.62); thus it is broadened by non-adiabatic transitions. On the other hand, the Josephson radiation at $p_\pi \ll p_0 \ll 1$ is dominated by the sine harmonics in eq. (3.36); thus it is broadened by the environment of the junction.

At $p_0, 1 - p_\pi \ll 1$, $I_{\rm DC} = p_0 I_J/\pi$ and $F = 1/2$; the noise spectrum displays a narrow resonance at half the Josephson frequency

$$S(\omega) = \frac{I_J^2}{4}\frac{\gamma'}{(\omega - \omega_J/2)^2 + \gamma'^2} \tag{3.63}$$

with linewidth

$$\gamma' = \frac{1}{2\pi}[p_0 + 2(1 - p_\pi)]\omega_J, \tag{3.64}$$

up to a small resonance-frequency shift, of the order of $\gamma'^2/\omega_J \ll \gamma'$, which increases as p_π decreases. Higher order resonances around $(n+1/2)\omega_J$ are suppressed. Comparison between eq. (3.36) and eq. (3.64) shows that the Josephson radiation is dominated by the noise, and it is thus broadened by the non-adiabatic processes. At $1 - p_\pi \ll 1$, transitions across the gap at π are very frequent, leading to a large, but random 4π-periodic contribution to the current. Thus, the Josephson radiation is fractional despite the junction *not* being topological. In the extreme case $p_\pi = 1$, where the transitions across the gap at π are deterministic, the system can be described as two independent topological junctions in parallel [23]. The crossover between a well-resolved fractional or conventional Josephson radiation, when p_0 is small and p_π increases from 0 to 1 occurs through the gradual shift and broadening of the peaks in the noise spectrum, as illustrated in fig. 3.5. A similar behaviour has been reported in topological junctions, but with a residual coupling to the Majoranas at the far ends of the superconducting wires [19].

To clarifies the relation between our model and topological junctions we propose in the following section an alternative description of the device at $p_\pi = 1$.

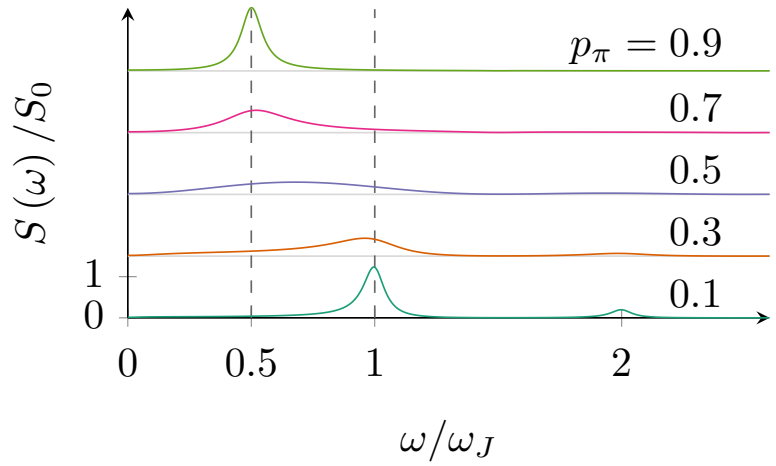

Figure 3.5: Current noise spectrum for $p_0 = 0.1$ and several equally spaced values of p_π between 0.1 and 0.9. The curves are shifted vertically for clarity.

3.4 Equivalent model at $p_\pi = 1$

When the Landau-Zener probability is $p_\pi = 1$, stochastic processes happen only at phases $\varphi = 2m\pi$. By contrast, at $\varphi = (2m+1)\pi$, a deterministic exchange between the states $|\pm\rangle$ takes place. In this case, a more natural basis of states $|a\rangle, |b\rangle$ is given as

- $|a\rangle = |+\rangle$ and $|b\rangle = |-\rangle$ for $(4m-1)\pi < \varphi < (4m+1)\pi$,
- $|a\rangle = |-\rangle$ and $|b\rangle = |+\rangle$ for $(4m+1)\pi < \varphi < 4(m+3)\pi$,

which absorbs the effect of the deterministic Landau-Zener transitions due to $\mathscr{L}_\pi$ at $p_\pi = 1$. This change of representation is described by fig. 3.6. Then the probabilities $\tilde{\boldsymbol{P}}(\varphi) = \big(P_{1_a 1_b}(\varphi), P_{1_a 0_b}(\varphi), P_{0_a 1_b}(\varphi), P_{0_a 0_b}(\varphi)\big)^T$ are constant over the phase intervals $2m\pi < \varphi < 2(m+1)\pi$ and evolve according to

$$\tilde{\boldsymbol{P}}(4m\pi^+) = \mathscr{L}_0 \tilde{\boldsymbol{P}}(4m\pi^-), \tag{3.65a}$$

$$\tilde{\boldsymbol{P}}((4m+2)\pi^+) = \mathscr{L}_{2\pi} \tilde{\boldsymbol{P}}((4m+2)\pi^-). \tag{3.65b}$$

Here the transition matrices $\mathscr{L}_\varphi$ can be decomposed into a tensor product of Markov matrices acting on distinct ABS branches, $\mathscr{L}_\varphi = \mathscr{L}_\varphi^{(a)} \otimes \mathscr{L}_\varphi^{(b)}$. In particular,

$$\mathscr{L}_0 = \mathscr{L}_- \otimes \mathscr{L}_+, \qquad \mathscr{L}_{2\pi} = \mathscr{L}_+ \otimes \mathscr{L}_-. \tag{3.66}$$

We denote by $|n\rangle_x$ that the state $x = a, b$ contain $n = 0, 1$ particle. The new transition matrices in the basis $\{|1\rangle_x, |0\rangle_x\}$ with $x = a, b$ take the form

$$\mathscr{L}_- = \begin{pmatrix} 1 & p_0 \\ 0 & 1-p_0 \end{pmatrix}, \qquad \mathscr{L}_+ = \begin{pmatrix} 1-p_0 & 0 \\ p_0 & 1 \end{pmatrix}. \tag{3.67}$$

Thus, the occupations of the two states $|a\rangle$ and $|b\rangle$ switch independently. The dynamics of each state is governed by the same equations as the dynamics of the 4π-periodic Andreev bound state appearing in a topological Josephson junction [50]. The two states carry a current $I_{a/b}(\varphi) = \pm I_J \sin\big(\varphi/2\big)$. Furthermore, the current operator $\hat{\mathscr{I}}$ is also separable,

$$\hat{\mathscr{I}} = \frac{1}{2}(\sigma_z \otimes \mathbb{1} - \mathbb{1} \otimes \sigma_z). \tag{3.68}$$

As a consequence, at $p_\pi = 1$, the system can be described as two independent topological junctions in parallel. Thus, both the average current and the noise are doubled compared to the values for the topological junction reported in [50]. As a consequence, one obtains the same Fano factor, $F = 1/2$, as well as a peak in the noise spectrum at $\omega = \omega_J/2$, corresponding to a fractional Josephson effect.

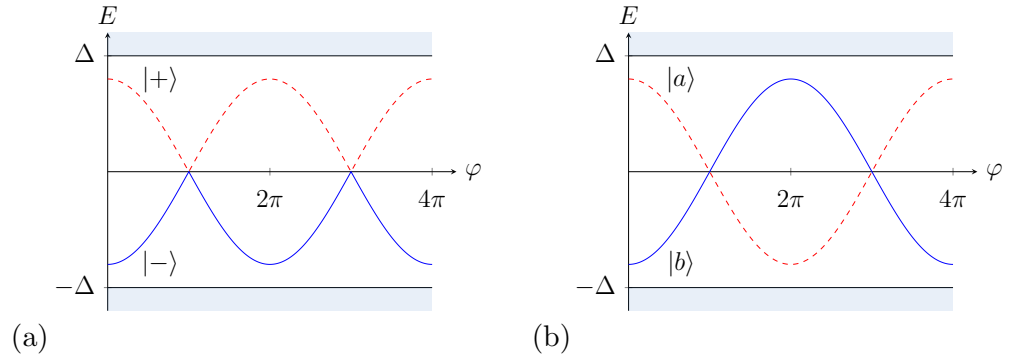

Figure 3.6: (a) Representation of the Andreev Bound states in the initial basis $|\pm\rangle$. The solid line corresponds to the state $|-\rangle$. The Dashed line is the state $|+\rangle$. (b) Representation of the Andreev Bound states in the basis $|a/b\rangle$. The deterministic Landau-Zener process at $\varphi = (2m+1)\pi$ have been absorbed by the change of basis. The solid line corresponds to the state $|b\rangle$. The Dashed line is the state $|a\rangle$.

Conclusion

In this chapter, we proposed a simple model to analyse the role of non-adiabatic transitions between Andreev states in the Josephson radiation of a superconductor-quantum dot-superconductor junction. Within a simplified model of the Andreev states' dynamics, we predicted that such a conventional junction may display either conventional radiation or fractional radiation, thus mimicking a topological Josephson junction, depending on its parameters and on the bias voltage. Thus, it would be interesting to extend the analysis to a more general description of the Andreev dynamics, as well as to develop a theory frame to compare the influence of the environment (neglected in our study) and the non-adiabatic transition on the loss of coherence of the Josephson radiation. The following chapters will focus on a microscopic model of the junction, and introduce numerical tools to solve the resulting Dyson equation in time domain.

CHAPTER 4

Quantum-dot junctions in the quantum field formalism

This chapter introduces a microscopic description of the quantum dot junction. We start with a Hamiltonian picture of the closed system formed by the dot connected to extended leads. In this initial framework, we derive the expressions of the average current and its fluctuations. To reduce the problem size, we formally integrate out the lead degrees of freedom using the quantum field formalism. This results in a description of the dot as an open system dressed by the interactions induced by the leads. We then deduce the expressions of the observables in this new framework.

4.1 Hamiltonian model

4.1.1 Hamiltonian

Here we introduce the different objects appearing in the microscopic Hamiltonian. The leads are BCS superconductors [13] with uniform order parameter Δ_l. The operators $\psi^\dagger_{\alpha,l,s}$ create an electron of spin s in the mode α of the lead l, and $d^\dagger_s$ create an electron of spin s on the dot at energy ε. The number operators are defined as $n_{\alpha,l,s} = \psi^\dagger_{\alpha,l,s}\psi_{\alpha,l,s}$ and $n_s = d^\dagger_s d_s$. $\epsilon_{\alpha,l}$ is the energy of an electron in the state α of the lead l at $\Delta_l = 0$. $t_{\alpha,l}$ is the tunnel coupling between the dot and the mode α of the lead l. The Fermi level of lead l is denoted by μ_l. U_C is the strength of the coulomb interaction between the electrons of the dot. It is related to the dot capacitance C by $U_C \sim e^2/2C$ [53]. Up to a unitary transformation, the tunnel couplings can absorb the order parameter phases such that Δ_l are positive real numbers. Hence, we may write the usual Hamiltonian [53, 54]

$$H = H_L + H_D + H_T - \sum_l \mu_l N_l, \tag{4.1}$$

with

$$\begin{aligned}
H_L &= \sum_{\alpha,l,s} \epsilon_{\alpha,l} n_{\alpha,l,s} + \sum_{\alpha,l} (\Delta_l \psi^\dagger_{\alpha,l,\downarrow}\psi^\dagger_{\alpha,l,\uparrow} + \Delta_l \psi_{\alpha,l,\uparrow}\psi_{\alpha,l,\downarrow}), && (4.2)\\
H_D &= \varepsilon \sum_s d^\dagger_s d_s + U_C n_\uparrow n_\downarrow, && (4.3)\\
H_T &= \sum_{\alpha,l,s} \left\{ t_{\alpha,l}\psi^\dagger_{\alpha,l,s} d_s + \text{h.c.} \right\}, && (4.4)\\
N_l &= \sum_{\alpha,s} n_{\alpha,l,s}. && (4.5)
\end{aligned}$$

When the Coulomb interaction is large enough, *id est* $U \gg \Delta_l \gg |t_l|^2$, and the dot is in the magnetic regime $-U_C < \varepsilon < 0$ one can account for the interactions by renormalizing the junction parameters [23, 24, 53]. It can be understood as follows, in presence of Coulomb interaction and when the dots have a non-zero spin, a screening electronic cloud may form. When the Coulomb interaction is large compared to the other relevant energies scales, the state of this electronic cloud is frozen. It results in a system that behaves as a non-interacting one with renormalized parameters. This situation is similar to the Fermi liquid theory. Hereafter, we will either suppose that the Coulomb interaction is negligible or that the parameters have been renormalized to include its effects. In both case, we drop the interaction term $U_C \to 0$. A second unitary transformation removes the energy offsets from the leads to include them in the tunnelling terms [55]. The operator of this transformation is

$$U(t) \quad = \quad \exp\left(i \sum_l \frac{\hat{N}_l}{\hbar} \int^t \mu_l(\tau) d\tau \right). \tag{4.6}$$

A time-dependent unitary transformation turns a Hamiltonian H into $\tilde{H}$ as follows

$$\tilde{H} = U(t) H U(t)^\dagger - i\hbar \frac{dU(t)}{dt} U^\dagger(t). \tag{4.7}$$

Both the lead and the dot Hamiltonians are invariant under the action of $U(t)$ as they conserve the particle numbers. This is trivial for the dot, but the situation of the leads deserves an explanation. At first sight the term $\Delta_l \psi^\dagger_{\alpha,l,\downarrow} \psi^\dagger_{\alpha,l,\uparrow}$ and $\Delta_l \psi_{\alpha,l,\uparrow} \psi_{\alpha,l,\downarrow}$ break the particle conservation symmetry. Yet, the parameter Δ_l must satisfy the self-consistency relation eq. (2.26). At the end, only the tunnel Hamiltonian must be examined closely. The operators $\hat{n}_{\alpha,l,s}$ commute which each others, thereby

$$U(t) \quad = \quad \prod_{\alpha,l,s} U_{\alpha,l,s}(t), \tag{4.8}$$

with

$$U_{\alpha,l,s} = \exp\left(i \sum_l \frac{\hat{n}_{\alpha,l,s}}{\hbar} \int^t \mu_l(\tau) d\tau \right). \tag{4.9}$$

$U_{\alpha,l,s}$ is a unitary operator that commutes with $\psi^\dagger_{\alpha',l',s'}$ when $(\alpha, l, s) \neq (\alpha', l', \sigma')$. Therefore

$$U(t) \psi^\dagger_{\alpha,l,s} U^\dagger(t) = U_{\alpha,l,s}(t) \psi^\dagger_{\alpha,l,s} U^\dagger_{\alpha,l,s}(t). \tag{4.10}$$

Finally, we end up with

$$U(t) \psi^\dagger_{\alpha,l,s} U^\dagger(t) \quad = \quad \psi_{\alpha,l,s} \exp\left(\frac{i}{\hbar} \int^t \mu_l(\tau) d\tau \right), \tag{4.11}$$

which leads to

$$H_T = \sum_{\alpha,l,s} \left\{ t_{\alpha,l} e^{i\phi_l(t)/2} \psi^\dagger_{\alpha,l,s} d_s + \text{h.c.} \right\}, \tag{4.12}$$

with the time dependent phase $\phi_l(t)$ set by the following relation

$$\phi_l(t) = \left(\frac{2e}{\hbar} \int^t V_l(\tau) d\tau \right) \quad \text{with } V_l(\tau) = \mu_l(\tau)/e. \tag{4.13}$$

The term $-\sum_l \mu_l \hat{N}_l$ being exactly cancelled by $i\hbar \frac{dU(t)}{dt} U^\dagger(t)$, we are left with

$$H(t) = H_L + H_D + H_T(t). \tag{4.14}$$

To efficiently deal with the superconducting leads, we introduce the operators d and Ψ in a Nambu space

$$d \equiv \begin{pmatrix} d_\uparrow \\ d_\downarrow^\dagger \end{pmatrix}, \tag{4.15}$$

$$\Psi_{\alpha,l} \equiv \begin{pmatrix} \psi_{\alpha,l,\uparrow} \\ \psi_{\alpha,l,\downarrow}^\dagger \end{pmatrix}. \tag{4.16}$$

We express the Hamiltonian $H = H_L + H_D + H_T$ in this representations

$$H_L = \sum_{\alpha,l} \Psi_{\alpha,l}^\dagger \left(\sigma_x \Delta_l + \sigma_z \epsilon_{\alpha,l}\right) \Psi_{\alpha,l}, \tag{4.17}$$

$$H_D = d^\dagger \sigma_z \varepsilon d, \tag{4.18}$$

$$H_T = \sum_{\alpha,l} \left\{ \Psi_{\alpha,l}^\dagger \mathscr{T}_{\alpha,l} d + \text{h.c} \right\}, \tag{4.19}$$

where σ_i are the Pauli matrices acting in the Nambu space and $\mathscr{T}$ is the tunnel matrix

$$\mathscr{T}_{\alpha,l} = t_{\alpha,l} \sigma_z e^{i\sigma_z \phi_{\alpha,l}(t)/2}. \tag{4.20}$$

Now that the microscopic Hamiltonian is set, we turn to the definitions of the observables.

4.1.2 Observables

We are interested in the statistical properties of the charge current flowing from a lead l to the dot. In the Nambu space, the charge number operators of the leads are $Q_l = -e \sum_\alpha \Psi_{\alpha,l}^\dagger \sigma_z \Psi_{\alpha,l}$: Defining the currents as the variations of these operators under the action of the tunnel Hamiltonians, we get

$$I_l(t) = \frac{-ie}{\hbar} [H_t(t), Q_l] \tag{4.21a}$$

$$= \frac{ie}{\hbar} \sum_\alpha \left\{ \Psi_{\alpha,l}^\dagger \sigma_z \mathscr{T}_{\alpha,l}(t) d - d^\dagger \sigma_z \mathscr{T}_{\alpha,l}^\dagger(t) \Psi_{\alpha,l} \right\} \tag{4.21b}$$

Once the operators are known, we can express their statistics in terms of the particle correlation functions. For the average current at the instant t, we start from

$$\langle I(t) \rangle = \frac{ie}{\hbar} \sum_\alpha \left\langle \Psi_{\alpha,l}^\dagger(t) \sigma_z \mathscr{T}_{\alpha,l}(t) d(t) - d^\dagger(t) \sigma_z \mathscr{T}_{\alpha,l}^\dagger(t) \Psi_{\alpha,l}(t) \right\rangle. \tag{4.22}$$

To exchange the operators and form proper Green functions we introduce the trace over the Nambu indices Tr^N , and use its invariance under cyclic permutations, taking into account the sign changes induce by the fermionic statistics

$$\langle I(t) \rangle = \frac{ie}{\hbar} \sum_\alpha \left\langle \text{Tr}^N \left[\Psi_{\alpha,l}^\dagger(t) \sigma_z \mathscr{T}_{\alpha,l}(t) d(t) - d^\dagger(t) \sigma_z \mathscr{T}_{\alpha,l}^\dagger(t) \Psi_{\alpha,l}(t) \right] \right\rangle, \tag{4.23}$$

$$= \frac{ie}{\hbar} \sum_\alpha \text{Tr}^N \left[\sigma_z \mathscr{T}_{\alpha,l}(t)^\dagger \left\langle \Psi_{\alpha,l}(t) d^\dagger(t) \right\rangle - \sigma_z \mathscr{T}_{\alpha,l}(t) \left\langle d(t) \Psi_{\alpha,l}^\dagger(t) \right\rangle \right] \tag{4.24}$$

$$= \frac{ie}{\hbar} \sum_\alpha \text{Tr}^N \left[\sigma_z \mathscr{T}_{\alpha,l}(t) \left\langle \Psi_{\alpha,l}^\dagger(t) d(t) \right\rangle - \sigma_z \mathscr{T}_{\alpha,l}(t)^\dagger \left\langle d^\dagger(t) \Psi_{\alpha,l}(t) \right\rangle \right]. \tag{4.25}$$

By replacing the creation destruction product by the *lesser* Green function $G^<$ we obtain

$$\boxed{\langle I(t) \rangle = \frac{e}{\hbar} \sum_\alpha \text{Tr}^N \left[\sigma_z \mathscr{T}_l(t) G^<_{d,(\alpha,l)}(t,t) - \sigma_z \mathscr{T}_l^\dagger(t) G^<_{(\alpha,l),d}(t,t) \right]} \tag{4.26}$$

Following a similar path, we could derive the expression of the current correlation function $\langle I(t')I(t)\rangle$ in terms of the 2-particle correlations functions. That we could factorize into products of one particle Green functions as the problem is non-interacting. Yet, this would provide a lengthy and useless expression. We shall wait to have derived the effective model before performing this kind of work.

4.2 Effective model

The initial microscopic Hamiltonian eq. (4.1) provides a description of the quantum dot, the leads and the coupling between them. Within the BCS theory, the superconducting leads are described by an effective quadratic Hamiltonian. Thus, the quantum field formalism permits to exactly integrate them out, leaving an effective description of the dot in terms of the bare dot Green function g_d dressed by the lead induced self-energies Σ_l. We start by writing down the action of the initial problem using the results from section 1.6

$$S = S_d[d^\dagger, d] + \sum_{\alpha,l} S_l[\Psi^\dagger_{\alpha,l}, \Psi_{\alpha,l}] + S_{d,l}[d^\dagger, \Psi^\dagger_{\alpha,l}, d, \Psi_{\alpha,l}], \tag{4.27}$$

with S_d the action associated to the dot, S_l the action of the lead l and $S_{d,l}$ the action resulting from the tunnel coupling between the dot and the leads l. By introducing the inverse Green functions of the isolated lead g_l^{-1}, and of the isolated dot g_d^{-1}, we can write the actions as

$$S_l\left[\Psi^\dagger_{\alpha,l}, \Psi_{\alpha,l}\right] = \int \mathrm{d}t\, \Psi^\dagger_{\alpha,l}(t) g_l^{-1}(t) \Psi_{\alpha,l}(t), \tag{4.28a}$$

$$S_d\left[d^\dagger, d\right] = \int \mathrm{d}t\, d^\dagger(t) g_d^{-1}(t) d(t), \tag{4.28b}$$

$$S_{d,l}\left[d^\dagger, \Psi^\dagger_{\alpha,l}, d, \Psi_{\alpha,l}\right] = -\int \mathrm{d}t\, \left\{\Psi^\dagger_{\alpha,l}(t)\mathscr{T}_{\alpha,l}(t) d(t) + \text{h.c.}\right\}. \tag{4.28c}$$

Thus, the partition function is

$$Z = \int \mathscr{D}[d^\dagger, d] \int \prod_{\alpha,l} \mathscr{D}[\Psi^\dagger_{\alpha,l}, \Psi_{\alpha,l}] e^{\frac{i}{\hbar}\left(S_d[d^\dagger,d] + \sum_{\alpha,l} S_l[\Psi^\dagger_{\alpha,l}, \Psi_{\alpha,l}] + S_{d,l}[d^\dagger, \Psi^\dagger_{\alpha,l}, d, \Psi_{\alpha,l}]\right)}, \tag{4.29}$$

Exploiting the Gaussian integration formula for Grassmann fields of appendix A, we can perform the integration over the leads configurations, this result in

$$\int \prod_l \mathscr{D}[\Psi^\dagger_l, \Psi_l] e^{\frac{i}{\hbar}\left(\sum_l S_l[\Psi^\dagger_l, \Psi_l] + S_{d,l}[d^\dagger, \Psi^\dagger_l, d, \Psi_l]\right)} = \prod_l \det\left(\frac{-i g_l^{-1}}{\hbar}\right) e^{\frac{-i}{\hbar}\iint_C d^\dagger(t)\mathscr{T}^\dagger_l(t)\frac{g_l(t,t')}{\hbar}\mathscr{T}_l(t')d(t')\,\mathrm{d}t\,\mathrm{d}t'}, \tag{4.30}$$

where we drop the mode index α. The determinant in front of the right-hand side of the above expression must vanish to preserve the normalization condition $Z = 1$, see eq. (1.106). The coupling to the leads is described through the introduction of self-energies Σ_l defined by

$$\Sigma_l(t, t') = \mathscr{T}^\dagger_l(t) \frac{g_l(t, t')}{\hbar} \mathscr{T}_l(t'). \tag{4.31}$$

Thus, the action of the effective theory is

$$S_{\text{eff}}[d^\dagger, d] = S_d[d^\dagger, d] - \sum_l \iint d^\dagger(t)\Sigma_l(t, t')d(t')\mathrm{d}t\,\mathrm{d}t'. \tag{4.32}$$

The generating functional is recast as an integral over the quantum dot field configurations

$$Z = \int \mathscr{D}[d^\dagger, d] e^{\frac{i}{\hbar} S_{\text{eff}}[d^\dagger, d]} \tag{4.33}$$

In the real-time picture, Σ_l has a matrix structure.

$$\Sigma \to \hat{\Sigma} \equiv \begin{pmatrix} \Sigma^{++} & \Sigma^{+-} \\ \Sigma^{-+} & \Sigma^{--} \end{pmatrix} \tag{4.34}$$

We denote by $\tau_{x,y,z}$ the Pauli matrices acting in the real-time Keldysh space, thus the real-time representation of the self-energy takes the form

$$\hat{\Sigma}_l = \sum_{\alpha,\alpha'} \mathscr{T}^{\dagger}_{\alpha,l}(t)\tau_z \hat{g}_{(\alpha,l),(\alpha',l)}(t,t')\tau_z \mathscr{T}_{\alpha',l}(t'), \tag{4.35}$$

where τ_z permits to take into account the sign change of the Hamiltonian on the backward branch, see eq. (1.95). The time ordered, anti-time ordered, lesser and greater self-energy are defined as

$$\begin{pmatrix} \Sigma^{++} & \Sigma^{+-} \\ \Sigma^{-+} & \Sigma^{--} \end{pmatrix} = \begin{pmatrix} \Sigma^{T} & -\Sigma^{<} \\ -\Sigma^{>} & \Sigma^{\tilde{T}} \end{pmatrix}. \tag{4.36}$$

By applying to $\hat{\Sigma}$ the transformation we applied to $\hat{G}$ in section 1.8, we obtain the symmetric representation of the self-energy, once again this name is misleading, as the corresponding is not symmetric in general.

$$\Sigma \to \begin{pmatrix} \Sigma^{K} & \Sigma^{R} \\ \Sigma^{A} & 0 \end{pmatrix}, \tag{4.37}$$

We observe that the disposition of the retarded, advanced, and Keldysh component is different from the one of symmetric Green function, see section 1.8. This underline that retarded and advanced component must be multiplied by components of the same kind. By contrast, the Keldysh components are multiplied on the left by the retarded one, and on the right by the advanced one.

For more details see chapter 5 of [28]. The expression of the Keldysh, retarded and advanced self-energies $\Sigma_l^{R/A/K}$ are provided by the following expression

$$\boxed{\Sigma_l^{R/A/K} = \sum_{\alpha,\alpha'} \mathscr{T}^{\dagger}_{\alpha,l}(t) \frac{g^{R/A/K}_{(\alpha,l),(\alpha',l)}(t,t')}{\hbar} \mathscr{T}_{\alpha',l}(t')} \tag{4.38}$$

By integrating the leads out of the system, we prevent direct application of the formula of the kind of eq. (4.26) as they involve Green functions between the dot and leads. Hence, we follow the counting field method [38, 54, 56] to derive the expressions of the observables in the reduced description.

4.2.1 Expression of observables in the effective model.

To derive the expression of the average current and its correlations, we supplement the generating functional by a counting field $\eta_l(t)$. It is introduced by the transformation $\mathscr{T}_l(t) \to \mathscr{T}_l(t) e^{i\frac{e\sigma_z\tau_z}{2}\eta_l(t)}$ in the real-time representation. Thus, the generating functional is

$$Z[\eta(t)] = \int \mathscr{D}[d^{\dagger},d] \int \prod_{\alpha} \mathscr{D}[\Psi_l^{\dagger},\Psi_l] e^{\frac{i}{\hbar}\left(S_d[d^{\dagger},d] + \sum_l S_l[\Psi_l^{\dagger},\Psi_l] + S_{d,l}[d^{\dagger},\Psi_l^{\dagger},d,\Psi_l;\eta_l]\right)}, \tag{4.39}$$

while we are using the same notations for the creation operator and the field configurations, one shall keep in mind that the field configurations have a structure in the Keldysh space

$$\Psi_l = \begin{pmatrix} \Psi_l^{+} \\ \Psi_l^{-} \end{pmatrix}, \tag{4.40}$$

where Ψ_l^+ refers to the configuration on the forward time branch, and Ψ_l^- on the backward branch. This convention also holds for the dot configurations:

$$d = \begin{pmatrix} d^+ \\ d^- \end{pmatrix}. \tag{4.41}$$

By taking the ln-derivative of the generating functional with respect to the counting field η we obtain

$$\frac{\delta \ln\big(Z[\eta]\big)}{\delta \eta_l(t)} = \int \frac{\mathscr{D}[d^\dagger,\Psi^\dagger,d,\Psi]e}{2\hbar Z[\eta_l(t)]} \sum_\alpha \Big\{\Psi^\dagger_{\alpha,l}(t)\sigma_z\tau_z\mathscr{T}_{\alpha,l}(t)d(t) - \text{h.c.}\Big\}\, e^{\frac{i}{\hbar}\hat{S}[d^\dagger,\Psi^\dagger,d,\Psi,\eta_l]}. \tag{4.42}$$

By adding a trace operator tr^{NK} over the Nambu and Keldysh index and taking care of the sign due to exchange of Grassmann variables, the terms in brackets can be changed into

$$\text{tr}^{NK}\Big\{\Psi^\dagger_{\alpha,l}(t)\sigma_z\tau_z\mathscr{T}_{\alpha,l}(t)d(t) - \text{h.c.}\Big\} = -\text{tr}^{NK}\Big\{\sigma_z\tau_z\mathscr{T}_{\alpha,l}(t)d(t)\Psi^\dagger_{\alpha,l}(t) - \text{h.c.}\Big\}. \tag{4.43}$$

From the results of chapter 1, or by having a look at [28, 29] we then deduce that

$$\frac{\delta \ln\big(Z[\eta]\big)}{\delta \eta_l(t)} = \frac{e}{2\hbar}\,\text{tr}^N\Big\{\sigma_z\mathscr{T}_{\alpha,l}(t)\big\langle \mathbf{T_C}{\Psi_{\alpha,l}}^\dagger(t^+)d(t^+)\big\rangle - \sigma_z\mathscr{T}_{\alpha,l}(t)\big\langle \mathbf{T_C}{\Psi_{\alpha,l}}^\dagger(t^-)d(t^-)\big\rangle - \text{h.c.}\Big\} \tag{4.44}$$

Finally, considering two real times t_1, t_2 the contour ordering imposes

$$\langle \mathbf{T_C}{\Psi_{\alpha,l}}^\dagger(t_1^+)d(t_2^+)\rangle = -\langle \mathbf{T_C}{\Psi_{\alpha,l}}^\dagger(t_1^-)d(t_2^-)\rangle. \tag{4.45}$$

Using this relation, we get

$$\left.\frac{\delta \ln\big(Z[\eta]\big)}{\delta \eta_l(t)}\right|_{\eta=0} = \frac{e}{\hbar}\,\text{tr}^N\big[\sigma_z\mathscr{T}_{\alpha,l}(t)\big\langle {\Psi_{\alpha,l}}^\dagger(t)d(t)\big\rangle - \text{h.c.}\big] \tag{4.46}$$

Thus we express the average current as a function of the augmented partition function $Z[\eta]$:

$$\boxed{\langle I_l(t)\rangle = i\left.\frac{\delta \ln\big(Z[\eta]\big)}{\delta \eta_l(t)}\right|_{\eta=0}} \tag{4.47}$$

Once the leads have been integrated out, the generating functional reads

$$Z[\eta] = \int \mathscr{D}[d^\dagger,d]\, e^{\frac{i}{\hbar}\left(\hat{S}_d[d^\dagger,d] - \sum_l \iint \mathrm{d}\tau\mathrm{d}\tau' d^\dagger(\tau)\Sigma_l(\tau,\tau')d(\tau')\right)}. \tag{4.48}$$

The equation 4.47 still holds, consequently:

$$\begin{aligned} \frac{2\hbar}{q}\langle I_l(t)\rangle &= \int \mathscr{D}[d^\dagger,d]\int \mathrm{d}\tau\big[d^\dagger(t)\tau_z\sigma_z\Sigma_l(t,\tau)d(\tau) - d^\dagger(\tau)\Sigma_l(\tau,t)\tau_z\sigma_z d(t)\big]\, e^{\frac{i}{\hbar}\hat{S}_{\text{eff}}[d^\dagger,d]}, &(4.49)\\ &= \int \mathscr{D}[d^\dagger,d]\,\text{tr}^{NK}\Big\{\sigma_z\tau_z\int \mathrm{d}\tau\big[d(t)d^\dagger(\tau)\Sigma_l(\tau,t) - \Sigma_l(t,\tau)d(\tau)d^\dagger(t)\big]\Big\}\, e^{\frac{i}{\hbar}\hat{S}_{\text{eff}}[d^\dagger,d]}, &(4.50)\end{aligned}$$

Finally, we deduce the expression of current:

$$\boxed{\langle I_l(t)\rangle = \frac{e}{2\hbar}\,\text{tr}^{NK}\Big\{\tau_z\sigma_z\int G(t,\tau)\Sigma_l(\tau,t) - \Sigma_l(t,\tau)G(\tau,t)\mathrm{d}\tau\Big\}} \tag{4.51}$$

Where G is the contour ordered Green function of the system. Using a similar argument we can also derive an expression for the current noise. In general, $I_l(t)$ and $I_l(t')$ do not commute, for a discussion on the symmetrized and unsymmetrized noise see [57]. To deal with it, we use the same trick as [54, 56]: we impose the first temporal argument to live on the forward Keldysh branch, while the second is on the backward branch. Thus, we are not imposing any constraint on their relative position in real-time. The counting field is changed according to:

$$\mathscr{T}_{\alpha,l}(t) \to \mathscr{T}_{\alpha,l}(t) e^{ie\sigma_z\left(\eta_l^+(t)-\eta_l^-(t)\right)}, \tag{4.52}$$

As previously the first step is to derive the expression of the correlation function in terms of derivatives of the partition function with respect to the counting field. This time we start from eq. (1.49) to write

$$Z[\eta] = \mathrm{Tr}\left\{\mathbf{T_C} \exp\left(-\frac{i}{\hbar}\int_C \tilde{H}(t)\,\mathrm{d}t\right)\rho(-\infty)\right\} \tag{4.53}$$

where $\tilde{H}(t)$ is the Hamiltonian augmented by the counting field. This permits to painlessly demonstrate that

$$\boxed{-\left.\frac{\delta^2 \ln Z[\eta]}{\delta\eta_l^-(t)\delta\eta_{l'}^+(t')}\right|_{\eta=0} = \langle I_l(t) I_{l'}(t')\rangle - \langle I_l(t)\rangle\langle I_{l'}(t')\rangle} \tag{4.54}$$

The action of the reduced model is still quadratic, thus it can be written as

$$S_{\mathrm{eff}}[d^\dagger, d] = \int_C d^\dagger(t) G^{-1}(t) d(t)\,\mathrm{d}t, \tag{4.55}$$

where the full inverse Green function G^{-1} is provided by the relation

$$G^{-1} = g^{-1} - \Sigma, \tag{4.56}$$

and $\Sigma \equiv \sum_l \Sigma_l$ is the total self-energy. The generating functional is thus

$$Z[\eta] = \int \mathscr{D}[d^\dagger, d] e^{\frac{i}{\hbar}\int_C d^\dagger(t) G^{-1}(t) d(t)\mathrm{d}t}. \tag{4.57}$$

Once again, using the results from appendix A, we get

$$Z[\eta] = \exp\left\{\ln\det\left(\frac{G^{-1}}{i\hbar}\right)\right\} \tag{4.58}$$

To evaluate the derivative of the partition function with respect to the source field we use the same relations that for the derivation of the mean field approximation in section 2.1.3. We first transform the above equation into

$$Z[\eta] = \exp\left\{\mathrm{tr}\ln\left(\frac{G^{-1}}{i\hbar}\right)\right\} \tag{4.59}$$

Upon taking the functional log-derivative we get

$$\frac{\delta^2 \ln Z[\eta]}{\delta\eta_l^-(t)\delta\eta_l^+(t')} = \mathrm{tr}\left\{\frac{\delta}{\delta\eta_l^-(t)}\left(\frac{G}{\hbar}\frac{\delta G^{-1}}{\delta\eta_l^+(t')}\right)\right\} \tag{4.60}$$

The counting field is only present in Σ, see eq. (4.56), thus we can rewrite this equation as

$$-\frac{\delta^2 \ln Z[\eta]}{\delta\eta_l^-(t)\delta\eta_{l'}^+(t')} = \mathrm{tr}\left\{\frac{\delta}{\delta\eta_l^-(t)}\left(\frac{G}{\hbar}\frac{\delta\Sigma}{\delta\eta_{l'}^+(t')}\right)\right\} \tag{4.61}$$

Before diving into the evaluation of this expression, we shall introduce a Dirac operator δ_t which acts on a kernel G as follows

$$\delta_{t_1}(t,t') \equiv \delta(t-t_1)\delta(t_1-t'). \tag{4.62}$$

With this definition at hand, we write in a rather compact form the different functional derivatives

$$\frac{\delta\Sigma}{\delta\eta_l^-(t)} = ie\{\delta_t\sigma_z\Sigma_l - \Sigma_l\delta_t\sigma_z\} \tag{4.63a}$$

$$\frac{\delta\Sigma}{\delta\eta_{l'}^+(t')} = -ie\{\delta_t\sigma_z\Sigma_{l'} - \Sigma_{l'}\sigma_z\delta_{t'}\} \tag{4.63b}$$

$$\frac{\delta}{\delta\eta_l^-(t)}\left(\frac{G}{\hbar}\frac{\delta\Sigma}{\delta\eta_{l'}^+(t')}\right) = \frac{1}{\hbar}\left\{\frac{\delta G}{\delta\eta_l^-(t)}\frac{\delta\Sigma}{\delta\eta_{l'}^+(t')} + G\frac{\delta^2\Sigma}{\delta\eta_l^-(t)\delta\eta_{l'}^+(t')}\right\} \tag{4.63c}$$

To evaluate the derivative of G we first notice that $G = \hbar\left(g^{-1}-\Sigma\right)^{-1}$. Then, we get

$$\frac{\delta G(t_2,t_1)}{\delta\eta_l^-(t)} = \frac{1}{\hbar}G\frac{\delta\Sigma}{\delta\eta_l^-(t)}G \tag{4.64a}$$

$$= \frac{ie}{\hbar}\{G\delta_t\sigma_z\Sigma_l G - G\Sigma_l\sigma_z\delta_t G\} \tag{4.64b}$$

Hence the first term in brackets of eq. (4.63) is

$$\begin{aligned}\frac{1}{\hbar}\frac{\delta G}{\delta\eta_l^-(t)}\frac{\delta\Sigma}{\delta\eta_{l'}^+(t')} = \frac{e^2}{\hbar^2}\{&G\delta_t\sigma_z\Sigma_l G\delta_{t'}\sigma_z\Sigma_{l'} - G\delta_t\sigma_z\Sigma_l G\Sigma_{l'}\sigma_z\delta_{t'}\\ &-G\Sigma_l\delta_t\sigma_z G\delta_{t'}\sigma_z\Sigma_{l'} + G\Sigma_l\delta_t\sigma_z G\Sigma_{l'}\sigma_z\delta_{t'}\}\end{aligned} \tag{4.65}$$

The second term is

$$\frac{G}{\hbar}\frac{\delta^2\Sigma}{\delta\eta_l^-(t)\delta\eta_{l'}^+(t')} = \frac{e^2}{\hbar}\delta_{l,l'}\{G\delta_t\delta_{t'}\Sigma_{l'} - G\delta_{t'}\sigma_z\Sigma_{l'}\sigma_z\delta_t - G\delta_t\sigma_z\Sigma_{l'}\sigma_z\delta_{t'} + G\Sigma_{l'}\delta_t\delta_{t'}\} \tag{4.66}$$

Finally, after reordering the operators under the full trace we get an expression of the current correlation function

$$\begin{aligned}S_{l,l'}(t,t') = \frac{e^2}{\hbar^2}\,\mathrm{tr}\,&\{(\delta_t\sigma_z\Sigma_l G\delta_{t'})(\delta_{t'}\sigma_z\Sigma_{l'}G\delta_t) - (\delta_t\sigma_z\Sigma_l G\Sigma_{l'}\delta_{t'})(\delta_{t'}\sigma_z G\delta_t)\\ &-(\delta_t\sigma_z G\delta_{t'})(\delta_{t'}\sigma_z\Sigma_{l'}G\Sigma_l\delta_t) + (\delta_t\sigma_z G\Sigma_{l'}\sigma_z\delta_{t'})(\delta_{t'}G\Sigma_l\delta_t)\}\\ +\frac{e^2}{\hbar}\delta_{l,l'}\,\mathrm{tr}\,&\{\delta_t\Sigma_{l'}G\delta_{t'} - (\delta_t G\delta_{t'})(\delta_{t'}\sigma_z\Sigma_{l'}\sigma_z\delta_t)\\ &-(\delta_{t'}G\delta_t)(\delta_t\sigma_z\Sigma_{l'}\sigma_z\delta_{t'}) + \delta_t G\Sigma_{l'}\delta_{t'}\}.\end{aligned} \tag{4.67}$$

The last step is to express the full Green function.

4.3 Dyson equations

The action of the effective theory is quadratic, so the inverse contour ordered Green G^{-1} function shall verify

$$G^{-1}(t) = g^{-1} - \Sigma, \tag{4.68}$$

This can be recast into the usual Dyson equation [28]

$$G = g + g\Sigma G/\hbar, \tag{4.69}$$

Or its symmetric form:

$$G = g + G\Sigma g/\hbar\,. \tag{4.70}$$

To streamline the following equations, we set $\hbar \leftarrow 1$ till the end of this section. In the symmetric RAK basis, the Dyson equation 4.69 reads

$$\begin{pmatrix} 0 & G^A \\ G^R & G^K \end{pmatrix} = \begin{pmatrix} 0 & g^A \\ g^R & g^K \end{pmatrix} + \begin{pmatrix} 0 & g^A \\ g^R & g^K \end{pmatrix} \begin{pmatrix} \Sigma^K & \Sigma^R \\ \Sigma^A & 0 \end{pmatrix} \begin{pmatrix} 0 & G^A \\ G^R & G^K \end{pmatrix}. \tag{4.71}$$

By expanding the matrix products, we deduce the equations for each component:

$$G^{R/A} = g^{R/A} + g^{R/A}\Sigma^{R/A}G^{R/A}, \tag{4.72}$$

$$G^K = g^K + g^R\Sigma^K G^A + g^K\Sigma^A G^A + g^R\Sigma^R G^K\,. \tag{4.73}$$

The equation for G^K can be recast as:

$$G^K = \left(\mathbb{1} - g^R\Sigma^R\right)^{-1} g^K \left(\mathbb{1} + \Sigma^A G^A\right) + \left(\mathbb{1} - g^R\Sigma^R\right)^{-1} g^R\Sigma^K G^A\,. \tag{4.74}$$

Now, using the Dyson equations 4.69 and 4.70, we have

$$\left(\mathbb{1} - g^R\Sigma^R\right)^{-1} = G^R g^{R^{-1}} = \left(\mathbb{1} + G^R\Sigma^R\right) \tag{4.75}$$

Thus the equation for the Keldysh component is recast as

$$G^K = \left(\mathbb{1} + G^R\Sigma^R\right) g^K \left(\mathbb{1} + \Sigma^A G^A\right) + G^R\Sigma^K G^A\,. \tag{4.76}$$

Hence, the equation for G^K is formally solved once the equation for G^R is solved. Finally, the Dyson equation in the RAK basis can be rewritten as:

$$\boxed{\begin{aligned} G^R &= g^R + g^R\Sigma^R G^R, && \text{(4.77a)}\\ G^A &= G^{R^\dagger}, && \text{(4.77b)}\\ G^K &= \left(\mathbb{1} + G^R\Sigma^R\right) g^K \left(\mathbb{1} + \Sigma^A G^A\right) + G^R\Sigma^K G^A. && \text{(4.77c)} \end{aligned}}$$

Thereby, one first has to solve the equation for the retarded component, and then plug the result in 4.77c to obtain the full Dyson Green function. In the following, we will come across self-energies and Green functions describing instantaneous correlations, thus that are proportional to Dirac distribution in the time domain representation. When discussing the numerical resolution of such equations, it will be useful to consider a specialized version of the Dyson equation. We first introduce some new notations. For a function $A(t,t') = A_\delta(t)\delta(t-t') + A_{\text{smooth}}(t,t')$ where neither $A_\delta(t)$ nor $A_{\text{smooth}}(t,t')$ contain a Dirac distribution, we write

$$\mathring{A}(t,t') = A_\delta(t)\delta(t-t'), \tag{4.78a}$$

$$\check{A}(t,t') = A_{\text{smooth}}(t,t'). \tag{4.78b}$$

Thus, we can write down the product rules for a set of two operators $A = \mathring{A} + \check{A}$ and $B = \mathring{B} + \check{B}$

$$\mathring{A}B = \mathring{A}\mathring{B}, \tag{4.79a}$$

$$\check{A}B = \mathring{A}\check{B} + \check{A}\mathring{B} + \check{A}\check{B}. \tag{4.79b}$$

Hence, by defining $F^R = g^R\Sigma^R$, the retarded equation is rewritten as:

$$\mathring{G}^R = \mathring{g}^R + \mathring{F}^R\mathring{G}^R, \tag{4.80a}$$

$$\check{G}^R = \check{g}^R + \check{F}^R\mathring{G}^R + \mathring{F}^R\check{G}^R + \check{F}^R\check{G}^R. \tag{4.80b}$$

The equation 4.80a is a linear algebraic equation that is easy to solve. The second equation 4.80b differs from 4.77a by the presence of the instantaneous term $\mathring{F}^R\check{G}^R$. The expression, in terms of singular and regular components, of G^K stems from the product rule 4.79 and the equation 4.77c. In the following chapter, we will introduce a set of numerical methods to solve these equations in different setups.

4.4 Derivation of the bare Green functions

Before contemplating the resolution of the Dyson equation, one shall compute the bare Green functions. For simple systems like uniform non-interacting leads, or an isolated quantum dot, useful analytical expressions exist. We derive the Green functions for metallic and BCS superconducting leads. We conclude the section by the expression of the dot Green functions.

4.4.1 Metallic leads

Starting from eq. (1.132), we write the Green function of a metallic lead l in the energy representation as:

$$g_{l,\sigma}(E+i\eta)=\sum_{\alpha}\frac{\left|w_{\alpha,l}\right\rangle\left\langle w_{\alpha,l}\right|}{E+i\eta-\epsilon_{\alpha,l}}, \tag{4.81}$$

where $\left|w_{\alpha,l,s}\right\rangle$ are the leads eigenvectors of energy $\epsilon_{\alpha,l}$. η is the usual complex shift of energy that ensures a proper definition of the energy representation of the Green functions. Physically, it corresponds to introducing a finite relaxation rate. We introduce the spectral function $K_l(E)$ to replace the discrete sum by a more convenient integral

$$K_l(E)=\int\left|w_{\alpha,l}\right\rangle\left\langle w_{\alpha,l}\right|\delta(\epsilon_{\alpha,l}-E)d\alpha\,, \tag{4.82}$$

we get:

$$g_{l,\sigma}(E+i\eta)=\int_{-\infty}^{\infty}d\epsilon\frac{K_l(\epsilon)}{E+i\eta-\epsilon}. \tag{4.83}$$

To further simplify the expression, we perform the integration over ϵ. Hence, we have to choose a model for the density of states. The dependence of K_l with respect to the spatial coordinates can be disregarded: all its effects will be included in an effective tunnel coupling. When the characteristic energy width W of the lead conduction bands is much larger than all the other energy scales, *i.e.* $W\gg\Delta, t_{\alpha,l}, T, eV$, we may consider a flat density of states: $K_l(E)=K_l$. Due to this wideband assumption, the above integral does not converge. We regularize it by performing a symmetric integration:

$$g_{l,\sigma}(E+i\eta)=\lim_{\varepsilon_c\to+\infty}\int_{-\varepsilon_c}^{\varepsilon_c}d\epsilon\frac{K_l}{E+i\eta-\epsilon}, \tag{4.84}$$

this results in:

$$\boxed{g^{R/A}_{l,\sigma}(E)=\mp i\pi K_l}. \tag{4.85}$$

It can be recast in the time domain:

$$g^{R/A}_{l,\sigma}(t)=\mp i\pi K_l\delta(t). \tag{4.86}$$

The equilibrium kinetic equation is deduced from the relation eq. (1.131) which we reproduce here for the reader's convenience

$$g^K(E)=\left(g^R(E)-g^{R^\dagger}(E)\right)\tanh\left(\frac{E}{2k_BT}\right). \tag{4.87}$$

Hence, we immediately deduce the Keldysh component of the lead Green function:

$$g^K_{l\sigma}(E)=-2i\pi K_l\tanh\left(\frac{E}{2k_BT}\right) \tag{4.88}$$

The Green function $g^K_{l,\sigma}$ is not integrable. This is a direct consequence of the wideband approximation, but its Fourier transform is well-defined in the sense of distributions [32].

4.4.2 Superconducting leads

We now turn to superconducting leads. As in section 2.1.4 we first diagonalize the Bogolioubov-De Gennes Hamiltonian. Let $H_0 \equiv H_l(\Delta \to 0)$ be the normal state Hamiltonian, and $\left|w_{\alpha,l,\uparrow\downarrow}\right\rangle$ its eigenvalues: $H_0\left|w_{\alpha,l}\right\rangle = \epsilon_{\alpha,l}$. The Hamiltonian H_L is block diagonal in the basis built from $\left|w_{\alpha,l,\uparrow\downarrow}\right\rangle$. In the absence of magnetic fields, the wave-functions can be factorized as $\left|w_{\alpha,l,\uparrow\downarrow}\right\rangle = |\uparrow\downarrow\rangle \otimes \left|w_{\alpha,l}\right\rangle$, thus the eigenvector associated to H_L reads

$$\begin{pmatrix} \epsilon_{\alpha,l} & \Delta_l \\ \Delta_l & -\epsilon_{\alpha,l} \end{pmatrix}\begin{pmatrix} u \\ v \end{pmatrix}\left|w_{\alpha,l}\right\rangle = E\begin{pmatrix} u \\ v \end{pmatrix}\left|w_{\alpha,l}\right\rangle, \tag{4.89}$$

where $u, v \in \mathbb{C}^2$ are coordinates in the Nambu space. Hence, it amounts to solve the same equation as in section 2.1.4

$$\begin{pmatrix} \epsilon_{\alpha,l} & \Delta_l \\ \Delta_l & -\epsilon_{\alpha,l} \end{pmatrix}\begin{pmatrix} u_{\alpha,l} \\ v_{\alpha,l} \end{pmatrix} = E\begin{pmatrix} u_{\alpha,l} \\ v_{\alpha,l} \end{pmatrix}. \tag{4.90}$$

The eigenvalues are $E^{\pm}_{\alpha,l} = \pm\sqrt{\Delta_l^2 + \varepsilon^2_{\alpha,l}}$, and the eigenvectors satisfy

$$u^{\pm}_{\alpha,l}/v^{\pm}_{\alpha,l} = \frac{\varepsilon_{\alpha,l} \pm \sqrt{\varepsilon^2_{\alpha,l} + \Delta_l^2}}{\Delta_l}. \tag{4.91}$$

Thus applying eq. (1.132) we may write:

$$g_l(E + i\eta) = \sum_{\nu=\pm}\sum_{\alpha}\begin{pmatrix} |u^{\pm}_{\alpha,l}|^2 & u^{\pm}_{\alpha,l}v^{\pm *}_{\alpha,l} \\ v^{\pm}_{\alpha,l}u^{\pm *}_{\alpha,l} & |v^{\pm}_{\alpha,l}|^2 \end{pmatrix}\frac{\left|w_{\alpha,l}\right\rangle\left\langle w_{\alpha,l}\right|}{E + i\eta - E^{\pm}_{\alpha,l}}, \tag{4.92}$$

Once the sum over the indices ν is performed, we have

$$g_l(E + i\eta) = \sum_{\alpha}\begin{pmatrix} (\epsilon - E - i\eta) & \Delta_l \\ \Delta_l & -(\epsilon + E + i\eta) \end{pmatrix}\frac{\left|w_{\alpha,l}\right\rangle\left\langle w_{\alpha,l}\right|}{{E^+_{\alpha,l}}^2 + \Delta_l^2 - (E + i\eta)^2}. \tag{4.93}$$

As for the metallic leads, we replace the sum by an integral in the above expression by using the normal state spectral function 4.82:

$$\begin{aligned} g_l(E + i\eta) &= \int_{-\infty}^{\infty}\begin{pmatrix} (\epsilon - E - i\eta) & \Delta_l \\ \Delta_l & -(\epsilon + E + i\eta) \end{pmatrix}\frac{K_l(\epsilon)d\epsilon}{\epsilon^2 + \Delta_l^2 - (E + i\eta)^2} && (4.94)\\ &= \lim_{\varepsilon_c \to \infty}\int_{-\varepsilon_c}^{\varepsilon_c}\begin{pmatrix} (\epsilon - E - i\eta) & \Delta_l \\ \Delta_l & -(\epsilon + E + i\eta) \end{pmatrix}\frac{K_l\, d\epsilon}{\epsilon^2 + \Delta_l^2 + (\eta - iE)^2} && (4.95)\\ &= \begin{pmatrix} -(E + i\eta) & \Delta_l \\ \Delta_l & -(E + i\eta) \end{pmatrix}\frac{\pi K_l}{\sqrt{\Delta_l^2 - (E + i\eta)^2}} && (4.96) \end{aligned}$$

By taking the limit $\eta \to 0^{\pm}$, we deduce:

$$\boxed{g_l^{R/A}(E) = \begin{pmatrix} -(E + i0^{\pm}) & \Delta_l \\ \Delta_l & -(E + i0^{\pm}) \end{pmatrix}\frac{\pi K_l}{\sqrt{\Delta_l^2 - (E + i0^{\pm})^2}}} \tag{4.97}$$

We notice that the superconducting lead Green functions are diagonal in the same basis as their metallic counterpart. The eq. (1.131) provides the Keldysh component:

$$\boxed{g_l^K = -2i\pi\,\mathrm{Im}\left\{\frac{(E + i0^+)\sigma_0 - \Delta_l\sigma_x}{\sqrt{\Delta_l^2 - (E + i0^+)^2}}\right\}K_l\tanh\left(\frac{E}{2k_BT}\right)} \tag{4.98}$$

4.4.3 Dot Green function

The dot Hamiltonian describes a system with two degenerate states of opposite spins. The formula eq. (1.132) gives directly the retarded and advanced Green function in the Nambu space

$$\boxed{g_d^{R/A}(E) = (E \pm i\eta - \epsilon\sigma_z)^{-1}} \tag{4.99}$$

We immediately deduce the Keldysh Green function

$$\boxed{g_d^K(E) = -2i \begin{pmatrix} \frac{\eta}{(E-\varepsilon)^2+\eta^2} & 0 \\ 0 & \frac{\eta}{(E+\varepsilon)^2+\eta^2} \end{pmatrix} \tanh\left(\frac{E}{2k_BT}\right)} \tag{4.100}$$

4.5 Derivation of the self energies

Now that we have expressions for the lead Green functions, we are fully equipped to derive the expressions of the self-energies. Using that the lead Green functions are diagonal in the basis formed by the eigenvectors of the leads. The expression 4.38 is simplified to:

$$\hbar\Sigma_l^{R/A/K} = \sum_\alpha \mathscr{T}_{\alpha,l}^\dagger(t) g_{(\alpha,l),(\alpha,l)}^{R/A/K}(t,t') \mathscr{T}_{\alpha,l}(t'), \tag{4.101}$$

4.5.1 Metallic leads

For metallic leads, the tunnel coupling and the Green function commute, hence the phase difference is cancelled in the retarded and advanced self-energies. Removing for a moment the Nambu space, we have

$$\begin{aligned} \hbar\Sigma_{l,s}^{R/A}(t,t') &= \sum_\alpha t_{\alpha,l}^*(t) t_{\alpha,l}(t') g_{\alpha,l,s}^{R/A}(t-t') && (4.102)\\ &= \mp i\pi \sum_\alpha |t_{\alpha,l}|^2 \delta(t-t') && (4.103) \end{aligned}$$

where s refer to the spin degree of freedom. The functions $\gamma_l(t,t')$ characterize the interaction

$$\begin{aligned} \hbar\gamma_l(t,t') &= \pi \sum_\alpha t_{\alpha,l}^*(t) t_{\alpha,l}(t'), && (4.104)\\ &= \pi \sum_\alpha |t_{\alpha,l}|^2 e^{i\frac{\phi_l(t)-\phi_l(t')}{2}}, && (4.105) \end{aligned}$$

It thus appears that the coupling strength between the lead l and the dot is fully determined by $|\gamma_l|$

$$\boxed{\Sigma_{l,s}^{R/A}(t,t') = \mp i|\gamma_l|\delta(t-t')} \tag{4.106}$$

A similar derivation provides the expression of the Keldysh Green function

$$\boxed{\Sigma_{l,\sigma}^K = -2i\gamma_l(t,t') \int_{-\infty}^{\infty} \tanh\left(\frac{E}{2k_BT}\right) e^{-i\frac{E(t-t')}{\hbar}} \frac{\mathrm{d}E}{2\pi\hbar}} \tag{4.107}$$

When the Fermi levels of the different leads are constants, γ_l depends only on the time difference $\gamma(t,t') = \gamma(t-t')$, i.e. it is stationary. Which implies that the all the self-energies are also stationary. Thus, in the steady state, the quantum dot is characterized by stationary Green functions.

4.5.2 Superconducting leads

As the tunnelling matrix does not commute with the Green function for non-zero order parameter, we cannot regroup the phase terms

$$\boxed{\Sigma_l^{R/A}(t,t') = -|\gamma_l| \int_{-\infty}^{\infty} \frac{dE}{2\pi\hbar} \frac{e^{-i\sigma_z \frac{\phi_l(t)-\phi_l(t')}{2}}(E+0^{\pm}) + \Delta\sigma_x e^{-i\sigma_z \frac{\phi_l(t)+\phi_l(t')}{2}}}{\sqrt{\Delta^2-(E+0^{\pm})^2}} e^{-\frac{iE(t-t')}{\hbar}}} \tag{4.108}$$

The same problem persists for the kinetic component:

$$\boxed{\begin{aligned}\Sigma_l^K = &-2i|\gamma_l| \int_{-\infty}^{\infty} \mathrm{Im}\left\{\frac{(E+0^{\pm})}{\sqrt{\Delta^2-(E+0^{\pm})^2}}\right\} e^{-i\sigma_z \frac{\phi_l(t)-\phi_l(t')}{2}} \tanh\left(\frac{E}{2k_BT}\right) e^{-i\frac{E(t-t')}{\hbar}} \frac{dE}{2\pi\hbar} \\ &-2i|\gamma_l| \int_{-\infty}^{\infty} \mathrm{Im}\left\{\frac{\Delta\sigma_x}{\sqrt{\Delta^2-(E+0^{\pm})^2}}\right\} e^{-i\sigma_z \frac{\phi_l(t)+\phi_l(t')}{2}} \tanh\left(\frac{E}{2k_BT}\right) e^{-i\frac{E(t-t')}{\hbar}} \frac{dE}{2\pi\hbar}\end{aligned}} \tag{4.109}$$

Thereby, when there are several superconducting leads in the system, even a constant voltage bias induces a non-stationary steady state, which is at the origin of the AC Josephson effect. This encourages us to develop a new method to solve the out-of-equilibrium equation, that exploits modern matrix compression methods initially developed for electrodynamics and classical many-body problems. In the following chapter we review the classical methods and then introduce the new algorithm.

CHAPTER 5

Solving the Dyson equations

The previous chapter lays down the physical model of the junction, and lefts us a set of out-of-equilibrium Dyson equations. At this point, one might expect to find in the literature well established and relatively efficient methods to solve it, but the bibliography on this subject is surprisingly shallow especially for the general out-of-equilibrium regime. However, we shall review the classical methods, and discuss their strength and weakness. To this end, we first introduce some notions of algorithmic complexity, remind a few things about numerical linear algebra and quadrature methods. Then we turn to the common methods presented in the literature. We will start with the algorithm for stationary problems, then look at the computation of the steady state of periodically driven systems by use of the Floquet theorem, to finally describe a general approach in the time domain.

5.1 Numerical analysis survival guide

Before discussing different strategies to solve the Dyson equations, we shall briefly review some aspects of computer science. For a general introduction to the algorithmic see Ref. [58], and for the more specific field of numerical analysis one may have a look to Ref. [59].

5.1.1 Complexity analysis

The computational complexity of an algorithm is the amount of time, space or any other relevant resource required to perform it. While it is often expressed as a function f of a single parameter n which characterised the problem size, it may depend on other parameters. Some of them might be unknown before the execution of the algorithm. Hence, depending on the scenario, one may consider the averaged or the worst case complexity for a fixed n. While the exact complexity depends on the specific implementation, it is generally accepted that the complexities of two reasonable implementations of the same algorithm shall not differ beyond a proportionality factor. Hence, we use the asymptotic notations: $\mathcal{O}$ and Θ. $f(n) = \mathcal{O}(g(n))$ indicates that f is asymptotically bounded by g, *id est* there is a number N and a positive constant C such that $n > N \Rightarrow f(n) \leq C g(n)$. While $f(n) = \Theta(g(n))$ indicates that f is bounded below and above by g. More formally, there exists a constant N and two positives numbers C_1 and C_2 such that: $n > N \Rightarrow C_1 g(n) \leq f(n) \leq C_2 g(n)$. One shall note that $f = \mathcal{O}(g)$ is often used even though $f = \Theta(g)$ would also be true.

5.1.2 Numerical linear algebra

The field of numerical linear algebra is an essential part of the scientific computing theory and practice. It describes how to perform efficiently matrix algebra operations, while minimizing the errors introduced by floating points representation of numbers. The adapted algorithm to a particular operation depends on the properties of matrices at hand.

Dense and sparse matrices

A first possible classification can be to the separation of dense and sparse matrices. A matrix is said to be dense when a significant part of its entries are non-zero, and we do not suppose any particular structure in its coefficients. By contrast, a matrix is sparse when most of its entries are zeros. One may ask what is a "significant part". Essentially, a matrix is dense when there is no clear benefits in using sparse matrix framework over dense matrix routines. For sake of clarity, let's consider the product of a $m \times n$ matrix A by a vector x, the complexity of the corresponding dense algebra routine is $\Theta(mn^2)$. While in the case where A is a sparse matrix with on average k non-zero elements per row, the complexity is only $\mathcal{O}(kmn)$, and the memory usage is reduced from $\Theta(mn)$ to $\Theta(km)$. Yet the discarded prefactors are usually much larger for sparse routines, thus the sparse routines are more efficient than the dense one only when $k \ll n$. Large sparse linear equations appear in numerous fields, notably as the results of the discretization of partial differential equations. Therefore, intense efforts have been devoted to develop efficient tools to solve such systems like PARDISO [60–62], MUMPS [63, 64] or Sparse Suite [65–67]. As a side note, in many numerical analysis textbook, the resolution of $Ax = b$ by inverting the matrix A is discouraged. It is rather advised to directly compute the solution x by direct methods. Hence, a specific notation exists: $x = A\backslash b$ that designates the division of b by A on the left.

BLAS and LAPACK

The Basic Linear Algebra Subprogram (BLAS) and the Linear Algebra Package (LAPACK) were originally libraries to perform elementary matrix algebra operations and solve linear equations. They have evolved into informal specifications for a set of routines to perform numerical linear algebra operations. Modern implementations of these specifications are extremely optimized codes. While efficient open-source implementations exist, most hardware vendors provide libraries specifically tuned for their products. Plus, some BLAS and LAPACK implementations are designed to leverage specialized hardwares such as graphical processing units (GPUs) or digital signal processors (DSPs). When performing linear algebra operations in Python with Scipy and Numpy, in Matlab, or in Julia, we are using these libraries through a convenient abstraction layer. As a rule of thumb, we should recast our algorithms in terms of matrix operations, to benefit from these optimized codes, even in case where it slightly increases the theoretical complexity.

5.1.3 Order of convergence

Let's consider a converging sequence u_n in a space equipped with a norm. We then borrow the definition of the index of convergence from Ref. [68].

Algrebraic index of convergence *The* algebraic index of convergence *or* convergence order μ *of the sequence* u_n *is the largest integer* k *such that*

$$\lim_{n\to\infty} \|u_n - u_\infty\| n^k < \infty. \tag{5.1}$$

Spectral convergence *A sequence is said to have a* infinite order, exponential *or* spectral *convergence when the algebraic index of convergence is infinite, that is*

$$\forall k \in \mathbb{N},\ \lim_{n\to\infty} \|u_n - u_\infty\| n^k = 0. \tag{5.2}$$

To compare spectrally convergent sequences, an exponential index of convergence can be defined (see Ref. [68]). In the following, the convergence index will be used to describe how different discretization schemes converge to an exact solution. But we should keep in mind that it is an asymptotic property. Let's consider the following problem: we want to solve a functional equation $\mathscr{L}(f) = 0$ of unknown f, where $\mathscr{L}$ is some functional that defines the equation. A usual approach is to first discretize the equation in a space of dimension N, and solve this new equation. A criterion to select a discretization scheme is the value of N required to achieve a certain accuracy. For this purpose, the index of convergence can be misleading; meaning that it only describes how fast the errors decrease once the asymptotic regime is reached. Let's say that we need to choose between two discretizations, one of order two and a spectral one. They start to converge when $N \gtrsim N_2$ and $N \gtrsim N_\infty$ respectively. If $N_2 \gtrsim N_\infty$, the spectral method wins, but when $N_2 \ll N_\infty$, the order two method will be more efficient to provide a low accuracy solution.

5.1.4 Quadrature methods

Quadrature rules, *i.e.* numerical integrations, are a rather broad topic, especially if we consider the problem arising in large dimensions and the infamous *curse of dimensionality*. Here we shall focus on a few results for 1-dimensional quadrature rules that sample the integrand at equidistant points. This last constraint prevents the use of efficient high order rules such as Gauss-Legendre [1]. In this section, we consider a sequence of equidistant points $x_0, x_1, ..., x_N$ spaced by a constant step h, and a smooth enough function f. The problem at hands, is to approximate an integral by a sum

$$\int_{x_q}^{x_p} f(x)\mathrm{d}x \approx \sum_{k=q}^{p} w_{q,k,p} f(x_i). \tag{5.3}$$

On a uniform mesh, specifying a quadrature amount to provide the coefficients $w_{q,i,p}$.

Order of a quadrature method *The* order d *of a quadrature method is the largest integer such that the quadrature provides the exact result for polynomials of degree $n \leq d$.*

Generally, the order of a quadrature rule does not coincide with its order of convergence, but it may provide a rough estimate when the integrand can be reasonably approximated by a polynomial of degree that matches the method order.

Composite quadrature rules *A* composite quadrature rule *is formed by dividing the integration domain into subdomains where the integral is evaluated by another quadrature rule.*

[1] High order stable rules on equidistant grid do exist, but they usually require much more points than the classical high order quadratures [69].

In this chapter, we shall limit ourselves with the glorious trapezoidal rule and the slightly exotic Gregory quadrature. We will not discuss the family of notorious Newton-Cotes rules that are present in most textbooks about numerical analysis, as they are unstable beyond first orders and do not possess the regularity that we will be seeking in the following chapters.

Trapezoidal rule

The trapezoidal rule is a quadrature that approximates the integrand by an affine function, thus its order is one

$$\int_{x_p}^{x_{p+1}} f(x)\mathrm{d}x = \frac{hf(x_p)}{2} + \frac{hf(x_{p+1})}{2} + o(h^2), \tag{5.4}$$

applying this rule on each subsegment, we get

$$\int_{x_p}^{x_q} f(x)\mathrm{d}x = \frac{hf(x_p)}{2} + \frac{hf(x_q)}{2} + \sum_{i=p+1}^{q-1} hf(x_i) + o(h^2). \tag{5.5}$$

In the following, we refer to this composite rule simply as the *trapezoidal quadrature*. This quadrature is extremely important for a few reasons. First, when the integrand is not smooth, this quadrature is difficult to beat, and it is easy to implement. Second, the approximation error is in even power of h, it may be shown using the Euler-Maclaurin summation formula [59]

$$\int_{x_p}^{x_q} f(x)\mathrm{d}x = \frac{hf(x_p)}{2} + \frac{hf(x_q)}{2} + \sum_{i=p+1}^{q-1} hf(x_i) - \sum_{l=2}^{k} \frac{B_l h^{2l}}{(2l)!}(f^{(2l-1)}(x_q) - f^{(2l-1)}(x_p)) - R_l, \tag{5.6}$$

where B_n are the Bernoulli numbers and the rest R_k can be majored by

$$R_k \leq h^{2k} \frac{B_{2k}}{(2k)!} \int_{x_0}^{x_N} |f^{(2k)}(x)|\mathrm{d}x. \tag{5.7}$$

Hence, if one computes an approximation S_N of the integral using N points and a second one S_{2N}, a better approximation can be built by combining the previous one

$$\begin{aligned} S_N &= S_\infty + \frac{\alpha}{N^2} + \frac{\beta}{N^4} + O\left(\frac{1}{N^6}\right), & (5.8)\\ S_{2N} &= S_\infty + \frac{\alpha}{4N^2} + \frac{\beta}{16N^4} + O\left(\frac{1}{N^6}\right), & (5.9)\\ \frac{4S_{2N} - S_N}{3} &= S_\infty - \frac{\beta}{4N^4} + O\left(\frac{1}{N^6}\right), & (5.10) \end{aligned}$$

where α and β are constants independent of N. Hence, $(4S_{2N} - S_N)/3$ converges as h^4. This process is called the Richardson acceleration and is particularly efficient with the trapezoidal rule as we increase by two the convergence order at each iteration. The last point that makes this rule so special is its *spectral convergence* for integration over the whole real line, or periodic integrand [70]. For instance, if we consider the problem

$$\begin{aligned} S &= \int_0^{2\pi} e^{\cos(x)}\mathrm{d}x, & (5.11)\\ &\approx \frac{2\pi}{N}\left[e + \sum_{i=1}^{N-1} e^{\cos\left(i\frac{2\pi}{N}\right)}\right]. & (5.12) \end{aligned}$$

The approximation can be compared with the exact value of S

$$S = 2\pi I_0(1), \tag{5.13}$$

where I_0 is the Bessel modified function of the first kind. Using the trapezoidal rule 5.12, an estimate of S limited by 64-bits floats points accuracy is reached with only 16 mesh points as shown in fig. 5.1. While it would require around 10^6 points to obtain the same accuracy with a cubic method. This suggests that

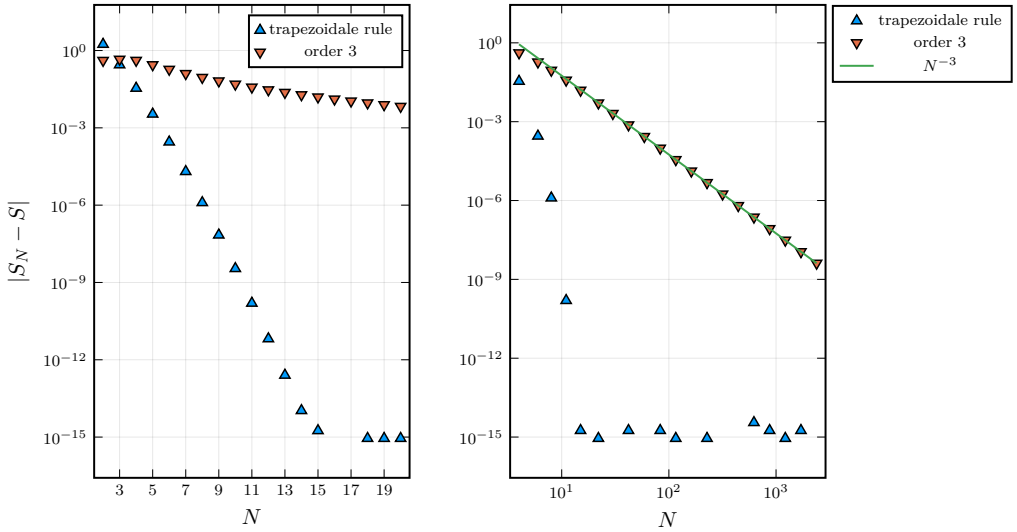

Figure 5.1: Comparison of the trapezoidal rule exponential convergence rate to a cubic convergence rate. On the left panel the horizontal axis is linear, while on the right panel it is in log scale. The spectral accuracy of the trapezoidal rule manifests itself on the left plot by the linear slope. The plateau in the errors associated to the trapezoidal rule is due to the finite accuracy of the number representation, *id est* the integral is accurate down to the machine precision.

most of the errors come from the edge of the integration domain. Several methods correct it, for instance one may rewrite the Euler-Maclaurin formula 5.6 as

$$\int_{x_0}^{x_N} f(x)\mathrm{d}x \approx \frac{hf(x_0)}{2} + \frac{hf(x_N)}{2} + \sum_{i=1}^{N-1} hf(x_i) - \sum_{p=2}^{k} \frac{B_p h^{2p}}{(2p)!}(f^{(2p-1)}(x_N) - f^{(2p-1)}(x_1)). \tag{5.14}$$

The term of the above equation involving the endpoint derivatives is a correction to the trapezoidal rule. Another quadrature derived by Gregory in the middle of the 16th century does not require the knowledge of any function derivatives, and will be useful to provide a compact discretization of the Dyson equation in the following chapter [71].

Gregory rules

The presentation of Gregory rules usually starts by introducing the finite difference operator $\Delta f(x) = f(x+h) - f(x)$. We will consider its iterates

$$\Delta^0 f(t) = f(t), \tag{5.15}$$
$$\Delta^1 f(t) = f(t+h) - f(x), \tag{5.16}$$
$$\Delta^2 f(t) = f(t+2h) - 2f(t+h) + f(t). \tag{5.17}$$

k	0	1	2	3	4	5	6
d_k	$-\frac{1}{2}$	$\frac{1}{12}$	$-\frac{1}{24}$	$\frac{19}{720}$	$-\frac{3}{160}$	$\frac{863}{60480}$	$-\frac{275}{24192}$

Table 5.1: Coefficient of the traditional Gregory quadrature

In the above formula, the coefficients of successive lines form the Pascal triangle. The Gregory rules for a semi-infinite interval with n_g+1 correction writes as

$$\int_{x_0}^{\infty} f(t)\mathrm{d}t \approx h\sum_{k=0}^{\infty} f(t_k) + h\sum_{k=0}^{n_g} d_k \Delta^k f(t_0), \tag{5.18}$$

where the first coefficients d_k are tabulated in table 5.1. The rule is extended to a finite interval by replicating the correction on the other side of the domain. For clarity, we introduce the reversed finite difference operator $\tilde{\Delta} f(t) = f(t-h) - f(t)$. The integral can then be approximated by

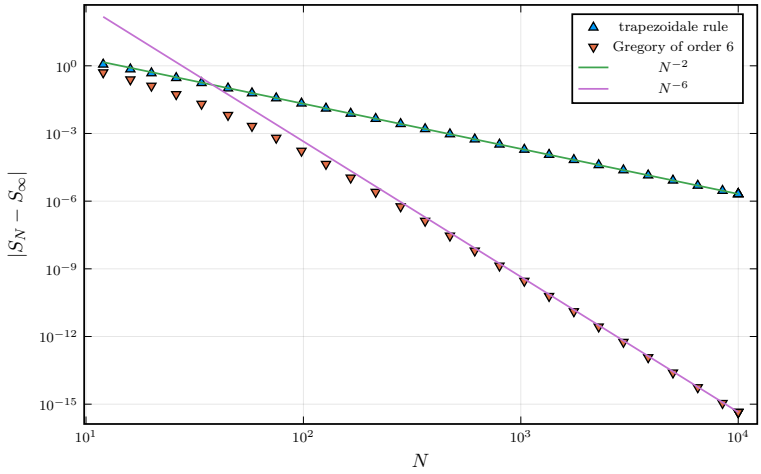

Figure 5.2: Benchmark of the Gregory rule of order six and the trapezoidal rule on the test problem $\int_0^{\infty} e^{-t}\mathrm{d}t = 1$.

$$\int_{x_0}^{t_n} f(t)\mathrm{d}t \approx h\sum_{k=0}^{\infty} f(t_k) + h\sum_{k=0}^{n_g} d_k \Delta^k f(t_0) + h\sum_{k=0}^{n_g} d_k \tilde{\Delta}^k f(t_n). \tag{5.19}$$

By expanding the correction terms for a given value of p, this quadrature can be rewritten under the form of eq. 5.3

$$\int_{t_q}^{t_p} f(t)\mathrm{d}x \approx \sum_{k=p}^{q} \ell_{p,k,q}^{(n_g)} f(t_k). \tag{5.20}$$

Fig. 5.2 compares the order 6 Gregory rule to the classical trapezoidal method. At large orders, the coefficient amplitudes are large, oscillating and some of them are negative. This may induce instabilities. Yet, it is worthy to note that some improvement over the classical rule can reduce this phenomenon [71]. And following the approach of Ref. [71] we may extend the historical Gregory rule to deal with edges singularities.

Now that the relevant notions of numerical analysis have been introduced, we can turn to the review of the classical numerical methods to solve the Dyson equations.

5.2 Steady state regime

Once the steady state is reached , most systems are expected to present some sort of invariance under time translation. These symmetries in time can be used to solve the Dyson equations in the frequency domain.

5.2.1 Stationary steady state

Even in the out-of-equilibrium regime, the correlation function might be stationary, meaning that they can be written as $g(t,t') = g(t-t')$. By Fourier transforming $g(t)$, we get $g(\omega)$. Then, using the following classical Fourier analysis result

$$\mathscr{F}\left\{\int_{-\infty}^{\infty} \mathrm{d}t_1 A(t-t_1)B(t_1)\right\} = \mathscr{F}\{A\}\mathscr{F}\{B\}, \tag{5.21}$$

where $\mathscr{F}$ is the Fourier transform operator, A and B are functions. We can then rewrite the integral equation as

$$G(\omega) = G(\omega) + g(\omega)\Sigma(\omega)g(\omega). \tag{5.22}$$

It can be solved independently at each energy by formally inverting the Dyson equation

$$G(\omega) = \big(1 - g(\omega)\Sigma(\omega)\big)^{-1} g(\omega). \tag{5.23}$$

Hence, when the self-energy Σ is known, only a relatively small equation per energy must be solved. For a system with m orbital states, the computational cost of solving the equation at a given ω scales at worst as $\mathscr{O}(m^3)$ in time and the computation requires a memory space of size $\mathscr{O}(m^2)$. Hence, to solve the equation at n energies, the total cost is $\mathscr{O}(nm^3)$ in time and $\mathscr{O}(nm^2)$ in memory. Yet, in many approximation schemes [72] that attempt to describe the effects of interactions, the self-energy and higher order correlation functions depend on the dressed Green function, as in the mean field approximation of the BCS theory. Hence the Dyson equation takes the following form

$$G(\omega) = g(\omega) + g(\omega)\Sigma[G](\omega)G(\omega). \tag{5.24}$$

This is a non-linear equation in G that must be solved at all energies at once. The Green function energy spectrum being typically spread over several orders of magnitude, naive approaches to solve the above equation are restricted to small or well-behaved systems. This is still motivating new research [30, 72]. As we have seen in the previous chapter, these methods are not directly applicable to our problem, even when we apply a constant bias across the junction as the self-energies induced by the superconducting leads are not stationary.

5.2.2 Periodic steady state

By the use of the Floquet theorem [73] , the Fourier representation can be extended to an out-of-equilibrium system driven by a periodic perturbation.

Floquet Theorem *Considering a T-periodic piecewise continuous function $A(t)$ and the following linear equation*

$$\frac{d\boldsymbol{x}(t)}{dt} = A(t)\boldsymbol{x}(t), \tag{5.25}$$

there is a matrix B and a matrix valued function $P(t)$ such that a fundamental matrix solution $\Phi(t)$ written as

$$\Phi(t) = P(t)e^{tB}. \tag{5.26}$$

This result is similar to the Bloch theorem that predicts the existence of band structures in a spatially periodic system. Both of them allow to block diagonalize a periodic Hamiltonian.

Floquet Hamiltonian

Let's derive the Floquet representation of the periodic Schrödinger equation following the reference [74]. We start by the usual equation

$$i\hbar\frac{\mathrm{d}}{\mathrm{d}t}\psi(t)=H(t)\psi(t). \tag{5.27}$$

When the Hamiltonian is P-periodic, the Floquet theorem suggests to look for solutions of the form

$$\psi_\alpha(t)=e^{-i\varepsilon_\alpha t/\hbar}u_\alpha(t) \tag{5.28}$$

with $u_\alpha(t)$ a P-periodic function, which can be Fourier transformed as

$$u_\alpha(t)=\sum_{n=-\infty}^{+\infty}u_\alpha^n e^{-in\Omega t}, \tag{5.29}$$

where Ω is the fundamental pulsation: $\Omega=\frac{2\pi}{P}$. Plugging this expression in the Schrödinger equation eq. (5.27) , one get

$$\sum_{m=-\infty}^{+\infty}(\varepsilon_\alpha+m\hbar\Omega t)\,u_\alpha^m=H(t)\phi_\alpha(t). \tag{5.30}$$

This suggests that we shall define

$$H_{mn}\equiv\frac{1}{P}\int_{-P/2}^{P/2}\mathrm{d}t\,H(t)e^{i(m-n)\Omega t}, \tag{5.31}$$

Injecting eq. (5.31) in eq. (5.29), we get the Floquet representation of the Schrödinger equation

$$\sum_{n=-\infty}^{\infty}H_{mn}\,u_\alpha^n=(\varepsilon_\alpha+m\hbar\Omega)u_\alpha^m. \tag{5.32}$$

We end up with an equation similar to the stationary Schrödinger equation, *except* that the energy is conserved up to an integer multiple of $\hbar\Omega$. $(\varepsilon_\alpha+m\hbar\Omega)$ is called the *quasi-energy*. H_{mn} is the coupling between the Floquet modes m and n. One can compare this situation to the diffusion of a wave by a periodic medium: when a focused beam of electron is shone on a crystal, the electronic wave vector is not conserved, yet only some directions of diffraction are authorized.

Floquet Green function

While the Green functions associated to a Floquet Hamiltonian are not stationary, one can show [75–77] that they present a discrete time translation invariance which is made explicit by introducing the average of time $T=(t+t')/2$ and the time difference $\tau=t-t'$, so that a Green function can be written as

$$G(T,\tau)=G(T+\tau/2,T-\tau/2). \tag{5.33}$$

When the Green function is associated to a Floquet Hamiltonian, it is periodic in T. Hence, we may develop $G(T,\tau)$ as a Fourier series in T and take the Fourier transform on τ. This leads to

$$G_n(\omega)=\frac{1}{P}\int_{-p/2}^{P/2}\mathrm{d}T\int_{-\infty}^{\infty}\mathrm{d}\tau\,e^{i(\omega\tau-\Omega mT)}G(T,\tau). \tag{5.34}$$

This is the so-called *Wigner representation* of the kernel $G(t,t')$. We then derive the *Floquet representation* $G_{mn}(\omega)$, with ω restricted to the first Brillouin zone $(-\Omega/2 < \omega \leq \Omega/2)$

$$G_{mn}(\omega) \equiv G_{m-n}\left(\omega + \frac{m+n}{2}\Omega\right). \tag{5.35}$$

Within this formalism, kernel products can be recast as matrix products

$$C(t,t') = \int \mathrm{d}t_1 A(t,t_1)B(t_1,t') \tag{5.36}$$

$$\Leftrightarrow C_{nm}(\omega) = \sum_{p=-\infty}^{\infty} A_{np}(\omega)B_{pm}(\omega) \tag{5.37}$$

Hence in the Floquet representation, the elements $G_{nm}(\omega)$ are the coupling of the Floquet mode n to the mode m of quasi-energy ω. For a stationary correlation function $A(\tau)$, one has

$$A_{mn}(\omega) = \delta_{m,n} A(\omega + m\Omega), \tag{5.38}$$

where the choice of Ω is arbitrary. The Dyson equation for the Floquet Green function is immediately deduced from section 4.3 in the real-time representation

$$G_F(\omega) = g_F(\omega) + g_F(\omega)\Sigma_F(\omega)G_F(\omega), \tag{5.39}$$

where $g_F(\omega)$, $\Sigma_F(\omega)$ and $G_F(\omega)$ are the Floquet matrices of the corresponding correlation functions in the real-time Keldysh formalism. For each value of ω, these matrices are infinite. To numerically solve this problem, an energy cut-off E_c larger that all the relevant energies of the system is usually included [54, 77]. The size N of Floquet matrices thus scales as $N \propto E_c/\hbar\Omega$. Solving the Dyson equation at a pulsation ω by standard methods thus costs $\mathcal{O}(N^3)$ operations and the required memory scales as $\mathcal{O}(N^2)$. The ω-axis must also be discretized. The required number of points M depends on the typical feature size $\omega_0 \ll \Omega$. A conservative estimate would be $M \sim \Omega/\omega_0$. Hence, the overall time complexity is $\mathcal{O}\left(E_c^3/\hbar^3\omega_0\Omega^2\right)$ and the required memory evolves as $\mathcal{O}(E_c^2/\omega_0\hbar\Omega)$. For instance, if we consider a Josephson junction formed by a quantum point contact biased by a small constant voltage $V \ll \Delta$, where Δ is the superconducting gap. The pulsation Ω coincides with the Josephson frequency $\omega_J = 2eV/\hbar$. Hence, as we decrease the applied bias, the computational cost increases as $1/V^2$ if the feature width is independent of the bias. However, in the Markov model, the equation 3.57 suggests that in highly transparent junctions, narrow structure of width γ appears in the spectrum with

$$\gamma = \frac{\omega_J}{\pi}\exp\left(-\frac{\pi\sqrt{1-T_\pi^2}\Delta}{eV}\right), \tag{5.40}$$

where T_π is the junction transparency. This sharp feature may increase largely the solving cost at low accuracy. Thus, the computational cost associated to the Floquet method can grow quickly when the system spectrum contains sharp resonances or several distant energy scales. Plus, as for the stationary method, the Fourier transform given by eq. (5.34) typically converges slowly due to a lack of regularity of the real-time Green function. This might represent a serious difficulty to solve the Dyson equation in interacting systems where the self-energy is approximated by a functional that depends on the full Green function. A natural cure is to renounce to solve numerically the Dyson equation in a Fourier representation, and use more adapted representations [72, 78, 79]. Plus, these frequency domain methods are not able to capture the general transient regime. This unconstrained out-of-equilibrium dynamics is more naturally described in the time domain. Hence, the last part of this chapter is dedicated to the exposition of the classical time domain strategy.

5.3 Transient regimes

In the transient regime, the absence of strong time invariance asks for resolution of the equations in the time domain. A rather naive yet instructive method is to construct a matrix representation of the integral operators appearing in the Dyson equations. And then rewrite the Dyson equation as matrices equations.

5.3.1 Nyström discretization

Let's consider a uniform discretization of the time axis of step-size h with N steps on each direction, and a bijection $\mathscr{I}$ from $\{1,2...N\}^2$ to $\{1,2...N^2\}$. Let's suppose that the orbital part, *id est* all non-temporal indices except the Keldysh ones, of correlation functions are discretized into M^2 degrees of freedom. A kernel $f_{x,x'}(t,t')$ is then represented as a matrix $\mathbf{f}$ of size $N^2M\times M$ organized by blocks of size $M\times M$. The $\mathscr{I}(p,q)$-th block represents the correlations between time t_p and t_q:

$$\mathbf{f}_{\mathscr{I}(p,q)} \equiv \mathscr{D} f(t_p,t_q), \tag{5.41}$$

where $\mathscr{D}$ is the operator that discretize the orbital part. In the following, we suppose that $\mathscr{D}$ is a morphism for the common operations on a vectorial space, up to the errors caused by discretization

$$\mathscr{D}\left\{f(t,t_1)g(t_1,t')\right\} \approx \mathscr{D}\left\{f(t,t_1)\right\}\mathscr{D}\left\{g(t_1,t')\right\}, \tag{5.42}$$

$$\mathscr{D}\left\{\lambda f(t,t')+g(t,t')\right\} \approx \lambda\mathscr{D}\left\{f(t,t')\right\}+\mathscr{D}\left\{g(t,t')\right\}, \tag{5.43}$$

with λ a scalar and g another correlation function. Hereafter, the orbital discretization operations will always be kept implicit. Introducing a set of quadrature rules $w_{p,k,q}$, the integrals are discretized according to

$$\int_{t_\alpha}^{t_\beta} K(t_p,t_1)f(t_1,t_q)\mathrm{d}t_1 \approx h\sum_k w_{\alpha,k,\beta}K(t_p,t_k)f(t_k,t_q). \tag{5.44}$$

This is the so called *Nyström discretization* [80], it permits to discretize the different integral operators which associate a function f with the map $(t,t')\to\int K(t,t_1)f(t_1,t')\mathrm{d}t_1$. We start by the operators appearing in the retarded Dyson equation, to which we refer as *Volterra operators parametrized by the kernel* K and write its discretized matrix representation as $\mathbf{V}[K]$. Its action is discretized following

$$\int_{t_p>t_1>t_q} K(t_p,t_1)f(t_1,t_q)\mathrm{d}t_1 \approx h\sum_k w_{p,k,q}K(t_p,t_k)f(t_k,t_q). \tag{5.45}$$

The reader may notice here a first problem caused by the Nyström approach, when K and f are retarded correlation functions, *i.e.* when

$$K(t,t') = \Theta(t-t')K(t,t'), \tag{5.46}$$

$$f(t,t') = \Theta(t-t')f(t,t'), \tag{5.47}$$

the eq. (5.45) rewrites as:

$$\int_{t_p>t_1>t_q} K(t_p,t_1)f(t_1,t_q)\mathrm{d}t_1 \approx h\sum_k w_{q,k,p}K(t_p,t_k)f(t_k,t_q)\Theta(t_p-t_k)\Theta(t_k-t_q), \tag{5.48}$$

$$\approx h\sum_{k=q}^{p} w_{q,k,p}K(t_p,t_k)f(t_k,t_q). \tag{5.49}$$

Thus only $(q-p+1)$ points are naively available to evaluate the integral from time t_q to t_p. While to ensure a certain convergence rate α of the discrete approximation, we would like to use quadratures of at least order $(\alpha-1)$. Such quadratures usually require at least α points. Thus, we are limited to the use of

order 1 quadratures. This issue can be solved by different tricks such as the one proposed in [81] where an analytic continuation of the retarded correlation function is used. For the moment, we will simply suppose that either we are using the trapezoidal rule that is of order 1, or that the correlation functions have been smoothly extended. Thus, the action of $\mathbf{V}[k]$ on a vector $\mathbf{f}$ is defined as

$$\mathbf{V}[K]\mathbf{f} = \left[\sum_l w_{p(l),l,q(l)}\mathbf{K}_{\mathscr{I}(p(l),l)}\mathbf{f}_{\mathscr{I}(l,q(p))}\right]_m, \tag{5.50}$$

$$= \left[\sum_{l|p(l)=p(m)} w_{p(m),q(l),q(m)}\mathbf{K}_{\mathscr{I}(p(m),q(l))}\mathbf{f}_l\right]_m, \tag{5.51}$$

where $\big(p(l),q(l)\big)=\mathscr{I}^{-1}(l)$. To rewrite the above relation as a matrix product, we introduce the following sets of indices

$$\mathscr{I}(:,q)\equiv\big\{m|\exists p\,(p,\,q)=\mathscr{I}^{-1}(m)\big\}, \tag{5.52}$$

and their indicating functions

$$\chi_{(:,p)}(m)=\begin{cases}1 & \text{if } m\in\mathscr{I}(:,p)\\ 0 & \text{otherwise}\end{cases}. \tag{5.53}$$

Thus, the general form of the matrix $\mathbf{V}[K]$ writes as

$$\mathbf{V}[K]=\big[w_{p(m),p(l),q(m)}\chi_{(:,q(m))}(l)\mathbf{k}_{\mathscr{I}(p(m),q(l))}\big]_{m,l} \tag{5.54}$$

The resulting discretization of the Volterra operator $\mathbf{V}[k]$ is of size $N^2\times N^2$, but on each line, at most N elements are non zeros. Hence, the number of non-zero elements is lesser than N^3. It turns out that $\mathbf{V}[K]$ is a sparse matrix. For simplicity, we consider the case where both the self energy and the bare retarded Green function do not contain Dirac singularities. Hence, we are left with the usual retarded Dyson equation

$$G^R(t,t')=g^R(t,t')+\int_{t>t_1>t'}F^R(t,t_1)G^R(t_1,t')\mathrm{d}t_1, \tag{5.55}$$

where $F^R=g^R\Sigma^R$. The solution of the retarded Dyson equation can thus be written as

$$\mathbf{G^R}=\big(\mathbb{1}-\mathbf{V}[F^R]\big)\backslash\mathbf{g^R} \tag{5.56}$$

The exact solving cost of this equation depends on the specific method used and the structure of the matrix. But, as we are explicitly storing the solution at each time point, the time and memory complexity cannot be lower that $\Theta(N^2)$ as it requires at least one operation per point. Usual direct sparse solver would require to store all the non-zero elements of the matrix resulting in a minimal time and space complexity of $\Theta(N^3)$. Considering the indexing defined by the following relation

$$\mathscr{I}(i,j)\equiv(j-1)N+i, \tag{5.57}$$

the matrix $\big(\mathbf{1}-\mathbf{V}[F^R]\big)$ is block diagonal, and each block is almost triangular of size $MN\times MN$. Thus, the eq. (5.56) can be solved block by block. Solving each quasi-triangular equation costs $\mathscr{O}(N^2)$ operations, thus the total solving cost is $\mathscr{O}(N^3)$ in time. This estimate match the results of the numerical experiment illustrated in fig. 5.3 that solves the equation by forming the sparse matrices in memory and solve the linear system by using the direct sparse solver provided by the Julia SparseArray library. This results in an $\mathscr{O}(N^3)$ memory complexity. Once the retarded Green function is known, the direct use of quadrature formula of the kind of 5.44 combined with expression 4.77c provides the kinetic Green function in $\Theta(N^3)$ operation while requiring $\Theta(N^2)$ bytes of memory. Hence, the whole resolution procedure scales at best as $\Theta(N^3)$ in time and $\mathscr{O}(N^2)$ in memory, when solving the equation for the retarded Dyson equation block by block. But parallelizing this approach by solving several blocks at once and thus exploiting modern computing architecture requires storing several blocks simultaneously in memory, and thus it increases the space consumption to $\mathscr{O}(dN^2)$, where d is the number of blocks solved at once. The *time stepping method* prevents this as presented in the next section.

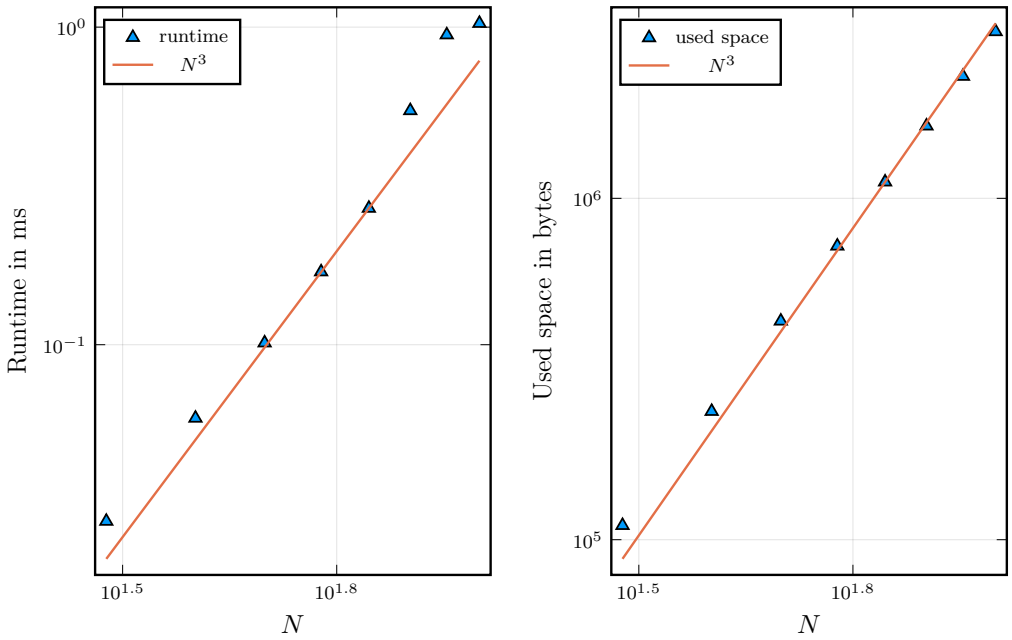

Figure 5.3: Experimental time and space complexity for the resolution of the retarded Dyson equation by direct resolution using sparse solver. The scaling is linear with the number of non-zero elements in matrix.

5.3.2 Time stepping method

For each value of t', the retarded Dyson equation is a linear integral Volterra equation of the second kind [59], *id est* an equation of the form

$$f(t) = s(t) + \int^{t} k(t, t_1) f(t_1) \mathrm{d}t_1, \tag{5.58}$$

where $k(t, t')$ and $s(t)$ are functions defining the problem and $f(t)$ is the unknown. This kind of problem arises in numerous fields such as finance [82], physics [83, 84] or biology [85]. Some efforts are still dedicated to the development of efficient and general methods [78, 86–88]. Yet, the classical algorithm [59] is relatively efficient and simple to implement. It amounts to first discretize the integral by the Nyström method, and then exploit the causal structure of the equation to solve it by a time stepping approach. The very same approach can be applied to the resolution of the retarded Dyson [81]. Let's consider the discretization of the retarded Dyson equation on a uniform grid of step size h with the quadrature rules $w_{q,k,p}$, such that

$$G^R(t_p, t_q) = g^R(t_p, t_q) + h \sum_{k \leq p} w_{q,k,p} F^R(t_p, t_k) G^R(t_k, t_q). \tag{5.59}$$

We may rewrite this equation as

$$G^R(t_p, t_q) = \left(1 - h\, w_{p,p,q} F(t_p, t_p)\right) \backslash \left\{ g^R(t_p, t_q) + \sum_{k<p} \omega_{q,k,p} F^R(t_p, t_k) G(t_k, t_q) \right\}. \tag{5.60}$$

Hence, once $G^R(t_{k<p}, t_q)$ is known, we can compute $G^R(t_p, t_q)$. The average number of operations required to perform a time step for a couple (p, q) is $\mathcal{O}(N)$ as we need to compute the history sum. So the average cost of a time step for all the values of q at a fixed p is $\mathcal{O}(N^2)$. Hence, the total cost is $\mathcal{O}(N^3)$ in time. While its memory complexity is only $\mathcal{O}(N^2)$. This method is equivalent to solving one Volterra equation

per value of q. This algorithm can be parallelized on a cluster [89]. In our own experience when working on a single node, *i.e.* on a laptop, the history summations can be efficiently implemented by recasting them as linear algebra operations. Thus, the parallelization is delegated to the highly optimized BLAS.

Conclusion

The naive time stepping method was until Fall 2020 the only published method at our knowledge to solve the general out-of-equilibrium Dyson equations. Therefore, both its memory and time complexity were prohibitive to solve the trajectories of even small systems on long times. As we will see in the following chapter, both time and memory usage can be greatly reduced by use of compression techniques. The first step is due to Ref. [30]. They were able to reduce months of computation effort to a day. We will go a step further and reduce even more the cost of solving the Dyson equations.

CHAPTER 6

Solving the Dyson equation using compression techniques

"On n'est jamais mieux servi que par soi-même"

— Charles-Guillaume Étienne, *Bruis et Palaprat*

In the previous chapter, we reviewed the usual methods to solve the Dyson equation. All of them have strong limitations: the Fourier representation requires some invariance by time translation and converged slowly towards the exact solution. While the more general time stepping method partially solves those issues, its complexity remains prohibitive for long times simulations. This last approach treats the Dyson equation as a large set of independent Volterra equations and solves them separately. Solving a unique Volterra equation is already a costly process as for evaluating each new time step, we have to recompute the whole history sum and by solving each of them independently we do not exploit their similarities to reduce the total complexity. Without any assumption on the aspect of the discrete problem, we cannot expect to do much better. However, it arises from the discretization of a continuous linear integral equation describing a physical system. Hence, it should present some structure that could be leveraged to reduce the solving cost in both memory and time. We begin this chapter by describing how to convert a certain class of integral equations into ordinary differential equations, thus removing the burden of the history sum. This will provide some insight about the kind of regularities that actually matter, and suggest storing the correlation functions as recursively semi-separable matrices. Then we introduce the hierarchically semi separable matrix (HSS) [90–93] as a method to efficiently represent the correlation matrices. To fully exploit this tool, we reformulate the Dyson equation discretized by the Nyström method into a compact matrix equation. The chapter concludes with some numerical benchmarks.

6.1 The intuition

My work on time domain numerical methods for the resolution of the Dyson equation started in Summer 2020, when I needed to solve it in the out-of-equilibrium regime. By this time the paper [30] was still unpublished, and the literature on this topic was rather thin. This deceived me into believing that the problem was too trivial to deserve any publications. Thus, I got my pen and I tried to cobble a solver together. It quickly became clear that the problem was still open and I got pretty interested in it. I tried various approaches with moderate success until I stepped on the theory of *holonomic* or $\mathscr{D}$*-finite* functions.

6.1.1 $\mathscr{D}$-finite functions

$\mathscr{D}$-finite functions *A function $f(x)$ is* $\mathscr{D}$-finite *or holonomic if it exists an integer n, and a set of polynomial function $a_k(x)$ such that*

$$\sum_{k=0}^{n} a_k(x)\frac{d^k f(x)}{dx^k} = 0. \tag{6.1}$$

Such a differential operator $\mathscr{L}$ is called an annihilator *of f.*

While the theory of holonomic functions is far out of the scope of this manuscript, it is not out of reach of the interested physicists, see [94, 95]. The set of holonomic functions $\mathscr{D}$ is extremely large, it includes all the rational fractions and all the holomorphic functions. Yet, not all common functions are holonomic. For instance, $1/\cos$ is not a holonomic function as any element of $\mathscr{D}$ has a finite number of poles in the complex plan. A holonomic function f can be represented by an annihilator $\mathscr{L}_f$ combined with a set of initial conditions. Operations on elements of $\mathscr{D}$ can be often recast as operations on the annihilators and initial conditions. Hence, the theory of holonomic functions provides a very elegant way to exactly represent a wide class of functions with a finite set of numbers, and therefore to recast functional equations into discrete equations. Could we represent the solution of the Dyson equation as a linear differential equation under some mild assumptions and thus avoid the evaluation of the history sums ? For the particular case of the retarded Dyson equation, the answer to this question is definitely *yes* as we are about to show.

6.1.2 Converting the integral equation to an differential equation

For clarity, we will suppose that all the functions appearing in this subsection are smooth enough so all the transformations are well-defined. For a function of two variables $A(t,t')$, we define

$$\partial_{p,q}A(t,t') \equiv \frac{d^{p+q}A(t,t')}{dt^p dt'^q}. \tag{6.2}$$

Here we consider the following Volterra equation

$$G^R(t,t') = g^R(t,t') + \int_{t'}^{t} F(t,t_1)G(t_1,t')\mathrm{d}t_1. \tag{6.3}$$

By differentiating the above equation with respect to t we get the relation

$$\partial_{1,0}G^R(t,t') = \partial_{1,0}g^R + F^R(t,t)G^R(t,t') + \int_{t'}^{t} \partial_{1,0}F(t,t_1)G(t_1,t')\mathrm{d}t_1. \tag{6.4}$$

Taking successive derivatives, we obtain a family of integro-differential equation of the form

$$\partial_{k,0}G^R(t,t') = \int_{t'}^{t} \partial_{k,0}F(t,t_1)G(t_1,t')\mathrm{d}t_1 + R_k[F^R,g^R]G^R, \tag{6.5}$$

where $R_k[F^R,g^R]$ is a differential operator. It admits a closed form, but its expression is of no use here. One might simply dismiss high order derivatives to obtain an approximate equation for the Green function. We will rather suppose that the kernel $F(t,t')$ satisfies a linear differential equation of the form

$$\sum_{p=0}^{k} c_p(t)\partial_{p,0}F(t,t') = 0. \tag{6.6}$$

We call $\mathscr{L}$ the corresponding differential operator. If we restrict the coefficients $c_p(t)$ to be polynomials, the function $t \to f(t,t')$ belongs to the set of holonomic functions. When its exists, the determination of $\mathscr{L}$ can be recast as a linear-algebra problem [94, 95]. Applying this operator on both sides of equation 4.77a, we get a linear differential equation for G^R

$$\boxed{\sum_{p=1}^{k} c_p(t)\left\{R_j[F^R, g^R] - \partial_{j,0}\right\} G^R(t,t') = 0,} \tag{6.7}$$

where R_j is a differential operator parametrized by F^R, g^R. Hence, we manage to transform the integral equation into a differential equation. The initial conditions are provided by taking the limit $t \to t'$ in eq. 6.5. The degree k of the resultant differential equation *might* be large, or the equation *could* contain sources of instability. Yet, we can still evaluate the asymptotic cost to solve it. Solving the differential equation for a given value of t' over N time steps costs $\mathcal{O}(k^3 N)$, while solving the equivalent Volterra equation by times stepping as describe in 5.3 cost $\mathcal{O}(N^2)$. For large values of N it is a neat improvement. Second, as the differential equation does not depend on t', only the initial conditions do, we do not need to solve the equation for each t'. It is enough to compute k independent solutions $(e_p(t))_{p=1\ldots k}$. This can be done in $\mathcal{O}(k^3 N)$. Hence, the retarded Green function can be written as

$$G^R(t,t') = \sum_{p=1}^{k} a_p(t') e_p(t). \tag{6.8}$$

Hence, we only need to store the value of $a_p(t')$ and $e_p(t)$. $a_p(t_i)$ is computed by solving a linear equation of size $\propto k$, hence it costs $\mathcal{O}(k^3)$ per point. Assuming that we discretize the second time axis t' on N points, computing both $a_p(t')$ and $e_p(t)$ costs $\mathcal{O}(k^3 N)$, and requires $\mathcal{O}(N)$ of memory space. As determining the differential equation satisfied by $F(t,t')$ does not depend on N, the overall complexity of this approach scales as $\mathcal{O}(N)$. This is a significant improvement over the time stepping method described in 5.3. It economizes the cost of the history sums by only keeping tracks of the relevant information, *i.e.* the derivatives. It also exploits the similarities between the correlation functions at different time arguments to reduce the amount of information required to fully describe the solution. Yet, the specific form we assume for the kernel is not general enough, and we did not propose a method for a fast evaluation of kernel products. Elaborations over the kind of transformations we performe here may permit to overcome these issues. But, it is October 2020, Jason Kaye and Denis Golež working at the *Flatiron institute* published on arXiv [30]. They managed to improve the time stepping method to solve a slightly different version of the out-of-equilibrium Dyson equation, namely the *Kadanoff-Baym* equation, by using only $\mathcal{O}\left(n \log n\right)$ space and $\mathcal{O}\left(n^2 \log n\right)$ operations. Their essential idea was to use a matrix compression known as *Hierarchical Off Diagonal Low Rank* (HODLR) matrices that enable them to speed up the evaluation of the history sum.

6.1.3 Matrix compression

The most general way to represent a matrix is to store all its entries. However, dense matrices arising from the discretization of continuous equation often present a structure that reduces the amount of information required to describe it. Finite difference discretizations of partial differential equations produce *sparse matrices*. Other scenarios lead to the formation of *low-rank* or *approximately low rank* matrices.

Low rank matrix *A matrix M of size $m \times n$ is said to be* low rank *when it exists an integer $r \ll \min(n,m)$ and two matrices U of size $m \times r$ and V of size $r \times n$, such that:*

$$M = UV \tag{6.9}$$

Thus, it is more efficient to store and manipulate the factors U and V than the full matrix.

It turns out that a matrix can be dense and yet contains only a small quantity of information. These matrices are called *data-sparse*. We can compress them as we would compress a picture, except that we want to perform some algebraic operation on these compact representations. In quantum physics, the most known format is probably the *Matrix product states* (MPS) and *matrix product operator* (MPO), which are commonly used to efficiently represent the states and Hamiltonians of many-body problems. To be of any use, the compression technics shall be adapted to the problem at hand. The HOLDR format used in [30] is one of the numerous format designed to represent matrix whose diagonal blocks are all *semi-separable*.

Semi-separable matrix *A $n \times n$ matrix M is said to be semi separable of semi separability rank r if it satisfies the following conditions*

$$\begin{aligned} \text{rank}(M[i:n, 1:\min(i+r-1, n)]) &\leq r \quad \forall i \in \{1, 2, ..., n\}, \\ \text{rank}(M[1:\min(i+r-1, n), i:n]) &\leq r \quad \forall i \in \{1, 2, ..., n\}. \end{aligned}$$

That is all the blocks extracted from either above the r-th super-diagonal or below the r-th sub-diagonal have a rank smaller than r. A whole family of algorithms has been developed to exploit this structure [96].

While the HOLDR format is commonly used to solve certain integral equations arising from electrodynamics, [30] does not propose any explanation of the observed performance. Yet, in the situation exposed in section 6.1.2, the retarded Green functions are the inverse of some differential operators. Upon discretization by finite difference methods, these operators are band diagonal, thus their inverses, that is the Green functions, are semi-separable [96]. Hence, the performance of HODLR-like format shall not be a surprise. By providing a compact matrix formulation of the Nyström discretized Dyson equation, and by doing a more efficient use of the inversion algorithms for compressed matrix, we reduce further the time complexity from $\mathcal{O}\left(n^2 \log n\right)$ to $\mathcal{O}\left(n \log n\right)$. While the HODLR format is very efficient, we will give a try to the more sophisticated *HSS* format.

6.2 Hierarchically semi-separable matrix

The HSS format is traditionally used for integral equations on the plane. It is more involved than the HODLR format, however it exhibits better asymptotic complexities. Yet, the main argument in favor of this compression is the availability of an open-source implementation in Julia [97] that we adapted for our needs, see [98]. While more mature implementations such as *STRUMPACK* [99] are available, their integration within our library would have required much more work. The HSS format is a multilevel format. The stored matrix is divided into blocks which are recursively compressed. At each level the diagonal blocks are supposed to be semi-separable. The interested reader may find the full details of algorithms used in our application in [90–92]. In the following we mostly follow the description proposed by [90].

At each level k of the hierarchy, we divide the matrix into 2^k row blocks and 2^k column blocks of width $\left\{m_{k:j}\right\}_{j=1}^{2^k}$. The $m_{k:j}$ form a set of partition of n, *id est*

$$\forall k, \sum_{j=1}^{2^k} m_{k:j} = n. \tag{6.10}$$

Intersection of the j-th row block and column block at level k defines the diagonal block matrix $D_{k:j}$. In particular, $D_{0:0}$ corresponds to the full matrix. They are factorized as follows

$$D_{k-1:j} = \begin{pmatrix} D_{k:2j-1} & U_{k:2j-1} B_{k:2j-1,2j} V_{k:2j}^T \\ U_{k:2j} B_{k:2j,2j-1} V_{k:2j-1}^T & D_{k:2j}. \end{pmatrix} \tag{6.11}$$

As we expect the blocks $D_{k,j}$ to be semi separable, the off-diagonal blocks should be low rank, i.e their rank r should be much smaller that both their height $m_{k:p}$ and width $m_{k:q}$. Hence, the *singular value decompositions* theorem states that there are three matrices $U_{k:p}$, $B_{k:p,q}$ and $V_{k:s}$ of size $m_{k:p} \times r$, $r \times r$ and $r \times m_{k:q}$,respectively, such that the off-diagonal block at level k formed by the intersection of row and column blocks $k:p$ and $k:q$ writes as $U_{k:p} B_{k:p,q} V_{k:q}$. Storing explicitly these matrices rather than the blocks would reduce the number of stored matrix entries from $m_{k:p} m_{k:q}$ to $r\left(m_{k:p} + r + m_{k:q}\right)$, yet the truncated change-of-basis matrices $U_{k:p}$ and $V_{k:s}$ are deduced from the next level matrices

$$U_{k:j} = \begin{pmatrix} U_{k+1:2j-1} R_{k+1:2j-1} \\ U_{k+1:2j} R_{k+1:2j} \end{pmatrix}, \quad V_{k:j} = \begin{pmatrix} V_{k+1:2j-1} W_{k+1:2j-1} \\ V_{k+1:2j} W_{k+1:2j}, \end{pmatrix} \tag{6.12}$$

where $W_{k:s}$ and $R_{i:s}$ are the displacement operators. Except at the last compression level, only $B_{k:i,j}$, $W_{k:i}$ and $R_{k:i}$ are stored.

HSS rank *The* HSS rank *is the maximum rank of all the off diagonal blocks at all levels. A matrix in HSS format is said to be compact if its HSS rank is small compared to its size, and all the generator R, W and B have size close to the* HSS *rank.*

For matrices of size $n \times n$ in HSS representation, a set of matrix algebra operations including inversion, matrix multiplication and addition can be performed in linear complexity in both memory and time with respect to n. At least if we suppose the HSS rank r to be independent of the size of the matrices at hand. But first, we need to build the HSS representation of the matrices. The deterministic methods starting from a plain matrix requires $\mathcal{O}(n^2 r)$ memory and space and would be the computational bottleneck, see [90]. Yet, faster algorithms exist for specific matrices [93]. In particular, several *stochastic algorithms* have been developed to overcome this issue[91]. They only require a method to access matrix elements and perform matrix vector products. It reaches a $\mathcal{O}(n r^2)$ time complexity when the matrix vector product routine is $\mathcal{O}(n)$ and the access to individual element is an $\mathcal{O}(1)$ operation. In the absence of fast matrix vector product, the time complexity is quadratic in n but the memory use remains proportional to n. This method is quite different from stochastic algorithm usually known by physicists, *e.g.* Monte-Carlo integration, as the approximation error is very low with relatively few samples. However, there is a finite probability of failure that is controlled by the user and can be made small enough for most applications. We shall refrain ourselves from describing further these algorithms to save some place. We emphasize that the method we propose does not depend critically on a specific compression method. It uniquely supposes the existence of efficient algorithms for the compression and algebraic manipulations of the matrices.

One might be tempted to use the matrix compression wizardry to solve the equation 5.56. We resisted to this temptation, but it shall result in $\mathcal{O}(N^2)$ in both memory and time, where N is the number of time steps on each axis. In the following section, we propose a compact formulation of the discretized Dyson equation, *id est* it only involves a few $N \times N$ matrices which will permit to reduce further this complexity.

6.3 Fast time domain solver

In the previous chapter, after using the Nyström method to discretize the equation, we obtain the matrix equation 5.56 involving $N^2 \times N^2$ sparse matrices with $\mathcal{O}(N^3)$ non-zero entries, where N is the number of time steps. Examination of the matrix expression 5.54 reveals that most of the coefficients are identical from blocks to blocks up to a change of the quadrature weights. The time stepping prevents this memory waste and can be fastened by compression methods as done in [30], yet this requires to implement efficiently non-standard linear algebra operations such as the low-rank update of compressed matrices. Here, we propose a strategy to solve the retarded Dyson equation by performing only standard matrix operations on $N \times N$ size matrices, thereby we exploit the modern matrix compression methods. But first, let's compress the matrices.

6.3.1 Compression of the initial kernel

To perform HSS factorization of the initial Green functions $g(t,t')$ and self energies $\Sigma(t,t')$, we use the stochastic HSS factorization algorithm [90]. To compress a matrix A of size $N \times N$, this method needs a fast algorithm to multiply A by an arbitrary vector in $\mathcal{O}(n)$ complexity, and constant time access to elements of A. It is usually easy to comply with this second constraint. For the first one, we have to exploit matrix particularities. We mostly encounter one of the following situations, either the matrix A is sparse, thus the problem is trivial, or A describes a stationary system, it is thus a Toplitz matrix. In this last scenario, the matrix vector products implemented using the fast Fourier transform (FFT) reach a computation complexity of $\Theta(N \log N)$. Therefore, in both situation, the overall factorization complexity shall be of $\mathcal{O}(N \log N)$, which is close to the optimal complexity that would be $\mathcal{O}(N)$.

Before discussing the compact discretization itself, we need a last stop which is the boundary conditions.

6.3.2 Boundary conditions

Strictly speaking the initial conditions are embedded in the Dyson equation. We don't need to supplement them with explicit conditions on the boundaries. Yet, as the kinetic correlation functions have *a priori* an infinite support, the convolution products of the form $A^R B^K$ or $A^K B^R$ require performing an integration on an infinite domain. To get rid of those issues, we suppose hereafter that the self energy $\Sigma(t,t')$ is turned on after the time t_0, and eventually turned off at the end of the simulation time t_{end}

$$\forall (t,t') \notin [t_0,\, t_{\text{end}}]^2 : \Sigma(t,t') = 0. \tag{6.13}$$

Thus, the integrand of the relevant convolution products vanishes outside the simulation domain. In particular, we have

$$\left[A^R B^K\right](t,t') = \int_{t_0}^{t} A^R(t,t_1) B^K(t_1,t') \mathrm{d}t_1, \tag{6.14}$$

$$\left[A^K B^R\right](t,t') = \int_{t_0}^{t} A^K(t,t_1) B^R(t_1,t') \mathrm{d}t_1. \tag{6.15}$$

One shall note that this constraint on the self-energy is not essential[30]. Yet, it simplifies the problem.

6.3.3 Equation for the retarded Green function

First we evacuate the resolution of the instantaneous part of the Dyson equation eq. (4.80)

$$\mathring{G}^R(t) = \mathring{g}^R(t) + \mathring{g}^R(t)\mathring{\Sigma}^R(t)\mathring{G}^R(t). \tag{6.16}$$

This equation is diagonal in time. Thus, it can be solved over N time steps in $\mathcal{O}(N)$ by solving the equation independently at each time step. Let's turn to the non-instantaneous equation. The Nyström discretization of the equation 4.80b yields to the following set of equations for the retarded Dyson equation, where we use the notation $F \equiv g\Sigma$ as in chapter 4.

$$\check{G}^R(t_p,t_q) = \check{s}^R(t_p,t_q) + \mathring{F}^R(t_p)\check{G}^R(t_p,t_q) + h\sum_{k=q}^{p} w_{q,k,p}\check{F}^R(t_p,t_k)\check{G}^R(t_k,t_q), \tag{6.17}$$

where

$$\check{s}^R = \check{g}^R + \check{F}^R\mathring{G}^R, \tag{6.18}$$

with F^R and G^R being both causal, we can extend the summation index

$$\check{G}^R(t_p,t_q) = s^R(t_p,t_q) + \mathring{F}^R(t_p)\check{G}^R(t_p,t_q) + h\sum_{k=0}^{N} w_{q,k,p}\check{F}^R(t_p,t_k)\check{G}^R(t_k,t_q). \tag{6.19}$$

The weights $w_{q,k,p}$ depend on three indices, and thus prevent from direct rewriting of the above formula as a $N \times N$ matrix equation. Yet, proper selection and factorization of the quadrature can solve this issue. For the moment let's suppose that there exists a quadrature $w_{q,k,p}$ of order α that requires $p-q > d$,which can be factorized as [1]

$$\boxed{w_{q,k,p} = a_{p,k}\,b_{k,q} + c_{p,k,q},} \tag{6.20}$$

with the constraint that it exists an integer n, independent of the number of time steps, such that

$$|p-q| > 2n \implies \begin{cases} a_{p,q} &= 1 \\ b_{p,q} &= 1\,. \\ c_{p,k,q} &= 0 \end{cases} \tag{6.21}$$

Then we extend the definition of coefficients $w_{q,k,p}$ to $p-q \leq d$ by setting

$$w_{p,k,q} \underset{p-q\leq d}{\equiv} 0, \tag{6.22}$$

this amounts to set

$$c_{p,k,q} \underset{q-p\leq d}{\equiv} -a_{p,k}\,b_{k,q}. \tag{6.23}$$

For p,q such that $p-q > d$, we rewrite the sum as

$$\sum_{k=0}^{N} w_{q,k,p}\check{F}^R(t_p,t_k)\check{G}^R(t_k,t_q) = \sum_{k=0}^{N} c_{p,k,q}\check{F}^R(t_p,t_k)\check{G}^R(t_k,t_q) + \sum_{k=0}^{N}\big(a_{p,k}\check{F}^R(t_p,t_k)\big)\big(b_{k,q}\check{G}^R(t_k,t_q)\big). \tag{6.24}$$

We introduce boldface symbols to denote the matrix representation of the discretized functions, *id est* $\check{\mathbf{G}}^{\mathbf{R}} \equiv \big[\check{G}^R(t_k,t_q)\big]_{k,q}$, and the element-wise multiplication operator $A \odot B \equiv [A_{p,q}B_{p,q}]_{p,q}$, which is also known as Hadamard product. Thus, we change the above expression into

$$\sum_{k=0}^{N} w_{q,k,p}\check{F}^R(t_p,t_k)\check{G}^R(t_k,t_q) = \sum_{k=0}^{N} c_{p,k,q}\check{F}^R(t_p,t_k)\check{G}^R(t_k,t_q) + \big(\mathbf{a}.\check{\mathbf{F}}^{\mathbf{R}}\big)\big(\mathbf{b}.\check{\mathbf{G}}^{\mathbf{R}}\big). \tag{6.25}$$

[1] One shall notice that we exchange the indices p and q.

From eq. (6.22), the above sum vanishes for $p-q \leq d$. By introducing the mask $\Pi^d_{p,q}$ defined as

$$\Pi^d_{p,q} \equiv \begin{cases} 1 \text{ if } p-q > d \\ 0 \text{ otherwise} \end{cases}, \tag{6.26}$$

and the corresponding matrix $\mathbf{\Pi^d}$, we recast the equation 6.19 as

$$\mathbf{\Pi^d} \odot \check{\mathbf{G}}^{\mathbf{R}} = \mathbf{\Pi^d} \odot \left(\mathbf{s}^{\mathbf{R}} + \mathring{\mathbf{F}}^{\mathbf{R}} \check{\mathbf{G}}^{\mathbf{R}}\right) + h \sum_{k=0}^{N} c_{p,k,q} \check{\mathbf{F}}^{\mathbf{R}}_{p,k} \check{\mathbf{G}}^{\mathbf{R}}_{k,q} + h\left(\mathbf{a} \odot \check{\mathbf{F}}^{\mathbf{R}}\right)\left(\mathbf{b} \odot \check{\mathbf{G}}^{\mathbf{R}}\right), \tag{6.27}$$

both sides of this equation are zero when $p-q \leq d$, otherwise it is the discretized Dyson equation. To transform this last expression into a linear matrix equation on $\mathbf{\Pi^d} \odot \check{\mathbf{G}}^{\mathbf{R}}$, we define $\tilde{\mathbf{s}}^R$ as

$$\tilde{\mathbf{s}}^R \equiv \mathbf{\Pi^d} \odot \mathbf{s}^{\mathbf{R}} + h \sum_{k=0}^{N} c_{p,k,q} \check{\mathbf{F}}^{\mathbf{R}}_{p,k} \check{\mathbf{G}}^{\mathbf{R}}_{k,q} + h\left(\mathbf{a} \odot \check{\mathbf{F}}^{\mathbf{R}}\right)\left(\left\{\mathbf{b} - \mathbf{\Pi^d}\right\} \odot \check{\mathbf{G}}^{\mathbf{R}}\right), \tag{6.28}$$

with $\mathbf{1}$ is the matrix filled by 1. We finally obtain the compact formulation of the retarded Dyson equation

$$\boxed{\mathbf{\Pi^d} \odot \check{\mathbf{G}}^{\mathbf{R}} = \tilde{\mathbf{s}}^R + \mathring{\mathbf{F}}^{\mathbf{R}}\left(\mathbf{\Pi^d} \odot \check{\mathbf{G}}^{\mathbf{R}}\right) + h\left(\mathbf{a} \odot \check{\mathbf{F}}^{\mathbf{R}}\right)\left(\mathbf{\Pi^d} \odot \check{\mathbf{G}}^{\mathbf{R}}\right).} \tag{6.29}$$

As the elements of $\mathbf{b}-\mathbf{\Pi^d}$, and $c_{p,k,q}$ are non-zero only close to the diagonal, evaluating $\tilde{\mathbf{s}}^R$ requires knowing $G^R(t_p, t_q)$ for $q-p < \max(2n, d)$. While evaluating accurately those few terms is crucial to preserve the overall accuracy, there are so few of them that it shall not be the computational bottleneck. For a solution to this problem, see [81]. Once these entries of $\mathbf{G^R}$ are known, we have to evaluate the Hadamard products. Methods to computes such product of HSS matrices do exist [93], but none is implemented by the library we use. Thus, we exploit the sparsity of $\left\{\mathbf{b}-\mathbf{\Pi^d}\right\} \odot \check{\mathbf{G}}^{\mathbf{R}}$ and $\left\{\mathbf{1}-\mathbf{\Pi^d}\right\} \odot \check{\mathbf{G}}^{\mathbf{R}}$ which contain only $\mathcal{O}(N)$ non-zero elements to build their HSS representation in linear time using the stochastic factorization algorithm. For the remaining term, we write $\mathbf{\Pi^d s^R} = \mathbf{s^R} + (\mathbf{1}-\mathbf{\Pi^d})\mathbf{s^R}$ and use the sparsity of $(\mathbf{1}-\mathbf{\Pi^d}) \odot \mathbf{s^R}$ to construct its HSS representation. While the HSS representation of $\mathbf{s^R}$ is known from the HSS representation of the self-energy Σ^R and the Green function g^R. Finally, using the resolution algorithm for HSS matrix equations, we can swiftly evaluate $\mathbf{\Pi^d} \odot \check{\mathbf{G}}^{\mathbf{R}}$.

6.3.4 Kernel product

Once the retarded Green function is known, the kinetic one is obtained by eq.4.77c. Thus, we need an efficient method to perform product of correlation functions. After the Nyström discretization, the general form of these products is

$$\forall (p,q), p-m(q) > d : \int A(t,t_1)B(t_1,t')\mathrm{d}t_1 \approx h \sum_k w_{q(t'),k,p(t)} A(t,t_k)B(t_k,t'), \tag{6.30}$$

where the functions $p(t)$ and $q(t')$ describe the integral boundaries, and $t_{m(q)}$ is the lower integration bound. Once again we need to represent these operations in terms of usual matrix algebra. We have to consider the products of correlation functions that preserve the time causality, *id est* $A^R B^R$, $A^R B^K$ and $A^K B^A$. The operations of the form $A^R B^K C^A$ can be decomposed into $(A^R B^K)C^A$ or $A^R(B^K C^A)$ as the terms in brackets are similar to a Keldysh correlator for what matters here. For a quadrature $w_{p,k,q}$ that can be factorized as in 6.20 and requires $p-q > d$, we have

$$\sum_k w_{q,k,m(q)} A(t_p,t_k)B(t_k,t_q) = (\mathbf{a} \odot \mathbf{A})(\mathbf{b} \odot \mathbf{B}) + \left[\sum_k c_{p,k,m(q)} A_{p,k} B_{k,q}\right]_{p,q}. \tag{6.31}$$

By this way, we compute most of the kernel products entries in $\mathcal{O}(N)$. We put aside the evaluation of the remaining $\mathcal{O}(N)$ matrix entries. See Ref. [81] for a strategy to evaluate these entries.

6.3.5 The quadrature rules

The compact formulation we developed here requires a set of quadrature rules $w_{p,k,q}$ of order α that satisfy the constraints 6.26. For $|p-q| > 2d$ the $w_{p,k,q}$ must be equal to 1 except at the edges. In that sense, this quadrature shall be a trapezoidal rule with endpoints corrections. This suggests to use a Gregory quadrature. Its weights $\ell^{(n_g)}_{q,k,p}$ have the property to be equal to 1 in the interior of the integration domain, more precisely

$$\forall k,\, q+n_g < k < p-n_g \implies \ell^{(n_g)}_{p,k,q} = 1. \tag{6.32}$$

Thus it is possible to factorize these weights as follows

$$\boxed{\forall (p,q),\, p-q > 2n_g+1 : \ell^{(n_g)}_{q,k,p} = \ell^{(n_g)}_{p,k,-\infty}\ell^{(n_g)}_{\infty,k,q}.} \tag{6.33}$$

Hence the Gregory rule can be factorized as announced. Yet, in practice we contented ourselves with the trapezoidal rule as it greatly simplifies the implementation of all the edges cases and can still be combined with Richardson acceleration when higher accuracy is required.

6.3.6 Evaluation of the observables

So far, we left aside the problem of efficiently evaluating the observables from the compressed representation. In general, this problem *is difficult*. Here, we are interested in the average current $\langle I_l(t)\rangle$ defined by eq. (4.51) and its fluctuations $S_{l,l'}(t,t')$ expressed by eq. (4.67). Computing $\langle I_l(t)\rangle$ only requires a few kernel products and to take the trace over the Nambu and Keldysh space of the resultant operators. The result is a vector that does not need any further compression to be stored. The evaluation of $S_{l,l'}(t,t')$ is much more challenging as it requires performing several blocks wise Hadamard products. While it shall be possible to extend the algorithm for the usual Hadamard product between compressed HSS or HODLR matrices to the block wise Hadamard product, we choose a different approach. We implement evaluation of individual elements of $S_{l,l'}(t,t')$ and then use the adaptative-cross-decomposition [100] to form the HODLR [93] representation of the current map in quasi linear complexity. We manage to evaluate the whole current fluctuation map in quasi-linear time, but our implementation is still orders of magnitude slower than the resolution of the Dyson equation. This excessive computational cost combined with the numerous terms involved in the expression of $S_{l,l'}(t,t')$ make the debugging process extremely tedious. Despite our effort, the map of the current correlation seems to be still erroneous.

In this section, we use the regularity of certain quadrature to propose a compact formulation of the Nyström discretized Dyson equation. This enables the efficient use of compressed matrix formats. Yet, we shall emphasize that it also permits to use regular or GPU-accelerated dense linear algebra routine to solve small size or difficult problems, *id est* problems that do not benefit from compression schemes. This compact formulation used without compression permits to solve the full equation by a few optimized BLAS routines, thus it shall be competitive with efficient implementations of the time stepping method. In the following section, we show our actual numerical results.

6.4 Benchmark

We implemented the algorithms described above in a still unpublished Julia library. It permits to solve the Dyson equation and manipulate the different correlation functions. The matrices are either stored as non-compressed dense and sparse matrices or compressed in the HSS format. To keep the implementation simple we renounce to high order methods and implement only the trapezoidal rule, high accuracy can still be reached by using the Richardson acceleration. The correctness of algorithms is ensured by automatic testing most of the library components. We benchmark the solver on both a normal-

QD-normal junction for which analytical results can be straightforwardly derived and a quantum-point-contact Josephson junction as the literature contains detailed study of its properties under perfect voltage bias.

6.4.1 Non superconducting junction

Let's begin with the non-superconducting device. As we are solving the Dyson equation in the time domain, we have access to the full evolution of the Green functions. We can access to the steady states properties by waiting for the transient regime to damp out. Here we consider two scenarios. In the first one we apply a constant voltage across the junction to observe the steady state current and plot the differential conductance of the junction. In the second experiment, we bias the junction with a voltage ramp, and plot the observed current $\langle I(t)\rangle$ as a function of the applied voltage $V(t)$. As the slope of ramp is decreased, we observe the convergence of the plotted IV relation toward the adiabatic one. This will be the occasion to demonstrate the capacity of our method to perform long time simulations. All the simulations are performed for a symmetric junction at resonance, *i.e.* $\Gamma_L = \Gamma_R$, at zero temperature and in the atomic units, *i.e.* $e = \hbar = 1$.

6.4.1.1 Steady state regime

To evaluate the steady states properties, we set the left lead potential V_L to V and the right lead potential V_R to 0. We measure the current $\langle I(t)\rangle$ once the steady state regime is settled. As in our situation, the retarded self-energy Σ^R is independent of the dressed Dyson equation, *i.e.* we are not considering a self-consistent approximation, the retarded Green function $G^R(t,t')$ does not depend on what happens before t'. Thus, it immediately reaches its steady state values. However, the kinetic component G^K that captures the particle distribution has a long memory. The full retarded dot Green function is independent of the applied voltage

$$G^R(t,t') = -i\Theta(t-t')e^{-\Gamma t}. \tag{6.34}$$

And the average current is given by [38]

$$I(V) = \frac{G_Q}{2}\int_0^{eV} T(E)\mathrm{d}E, \tag{6.35}$$

with $T(E)$ the junction transmission provided by

$$T(E) = \frac{\Gamma_L\Gamma_R}{((E-\varepsilon_0)/\hbar)^2 - ((\Gamma_L+\Gamma_R)/2)^2}, \tag{6.36}$$

and $G_Q = \frac{2e^2}{h}$. Thus, the differential conductance is provided by

$$\frac{\mathrm{d}I}{\mathrm{d}V} = \frac{G_Q e}{2}T(eV). \tag{6.37}$$

We can already observe in fig. 6.1 that the solver produces the expected outputs. To further evaluate the code performances, we measure the convergence rate, the average execution time and the averaged total allocated memory. This last quantity is an upper bound of the required memory, as it is the sum of the memory size of all the structures that have been allocated while the code was running and not all these structures coexisted in memory. To characterize the errors, we introduce the L_2 norm on matrix vectors defined as

$$||A||_2 \equiv \sqrt{\sum_{p,q=1}^{N} A_{p,q}^2}. \tag{6.38}$$

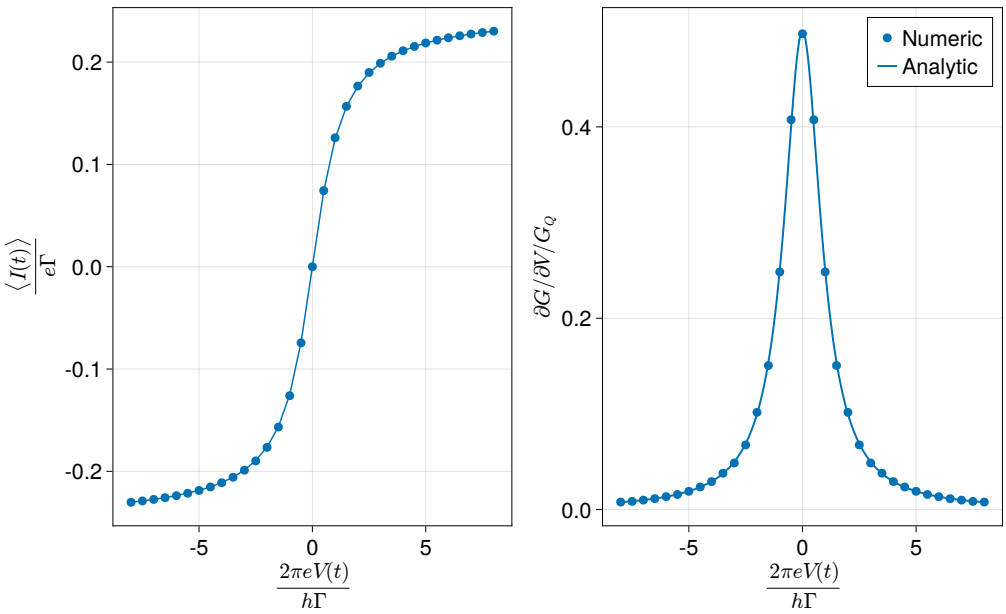

Figure 6.1: Average current flowing through a quantum dot junction at resonance. *Left panel*: IV characteristics. *Right panel*: differential conductance. We observe a perfect agreement between the analytical result and the simulation output.

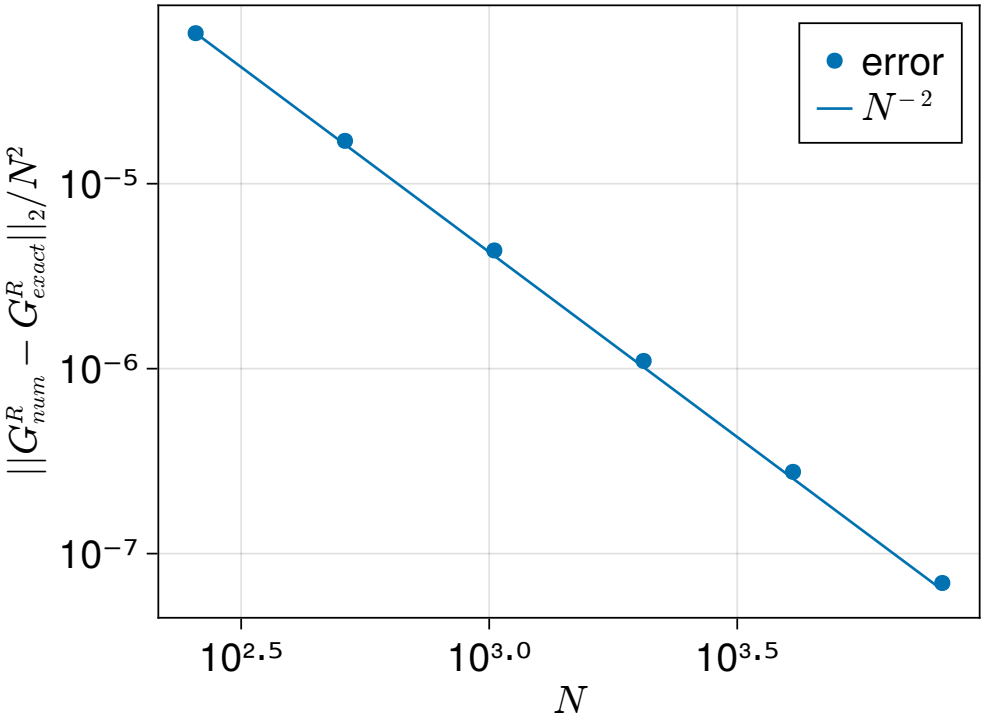

Figure 6.2: Evolution of the average error with respect to the number of discretization points. We observe a quadratic convergence rate. The simulation window extends from 0 to $10/\Gamma$

The fig. 6.2 shows that the retarded Green function converges with an order 2 toward the exact solution. This is the expected convergence rate, as the quadrature is of degree 1 and the solution is smooth. Yet, the

convergence rate of the IV characteristics is 1, see fig. 6.3. This slow convergence is probably caused by the singular behaviour of the free kinetic Green function of the leads at $t = t'$. This rate can certainly be improved by developing suitable quadrature rules. However, we prefer to demonstrate the use of Richardson acceleration to cancel the contributions to the error of the form $\alpha N + \beta N^{-2} + \gamma N^{-3}$. The accuracy is then limited by the remains of the transient regime. It appears as a plateau in fig. 6.3.

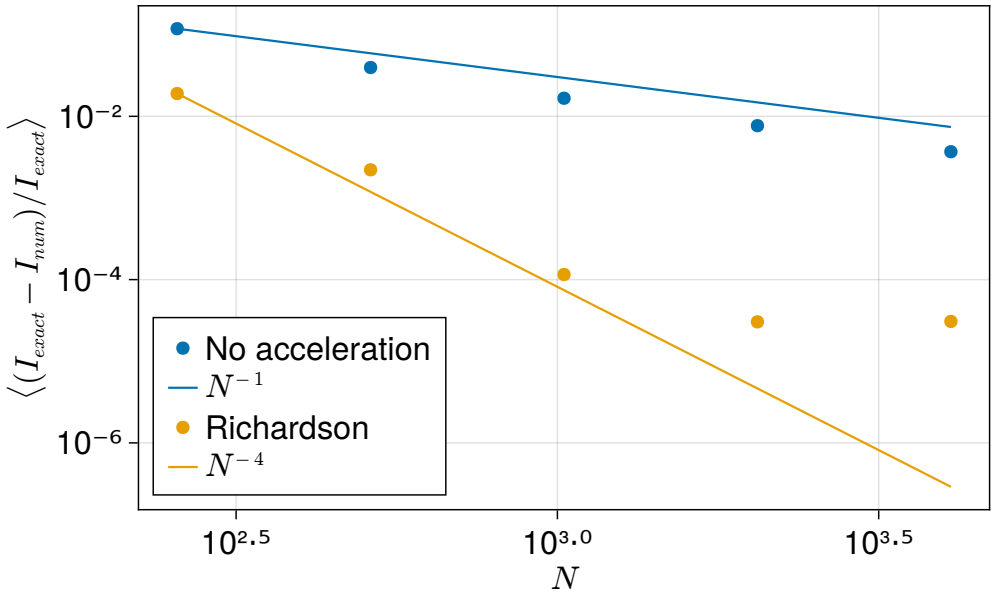

Figure 6.3: Convergence of the averaged steady state current toward the analytical results. The Richardson acceleration permits to increase the convergence order. The plateau, which is revealed by the order 4 method, is caused by the remains of the transient regime. The simulation length is set to $P = 100/\Gamma$.

Now that we have demonstrated the convergence of the solver, let's look at its performance. Once all the physical parameters are set, we vary the number of time steps N while keeping the simulation length P constant. We then monitor the total allocated memory and average runtime as shown in fig. 6.4. Both the memory and time complexity are in $\Theta(N \log N)$. This suggests that the resolution time is dominated by the construction of the stationary Green function that heavily uses the FFT, which has a $\Theta(N \log N)$ complexity.

The HSS representation of the matrix may not be exact, thus we have to set a parameter ε that controls the accuracy of this representation. Reducing its value increases the HSS rank of stored matrices, and thus it increases both runtime and memory cost. Hence, its values shall be chosen so that it does not limit the computation accuracy, while being large enough to ensure an efficient compression. In some case, the HSS representation is exact and thus independent of the set accuracy ε once it is below a certain threshold $\varepsilon < \epsilon_0$. The HSS rank may also depend on the other simulation parameters, such the simulation length P. Numerical results show that HSS rank of both the retarded and kinetic Green function to be independent of P. In fig. 6.5, we observe that the HSS rank of the retarded Green function G^R is even independent of the compression accuracy, this is not a surprise as $t \to G^R(t, t')$ is the solution of a differential equation that does not depend on t', see section 6.1.2. The kinetic Green function does not have the same regularity, hence its HSS representation is an approximation, that is why the corresponding HSS rank increases with the representation accuracy.

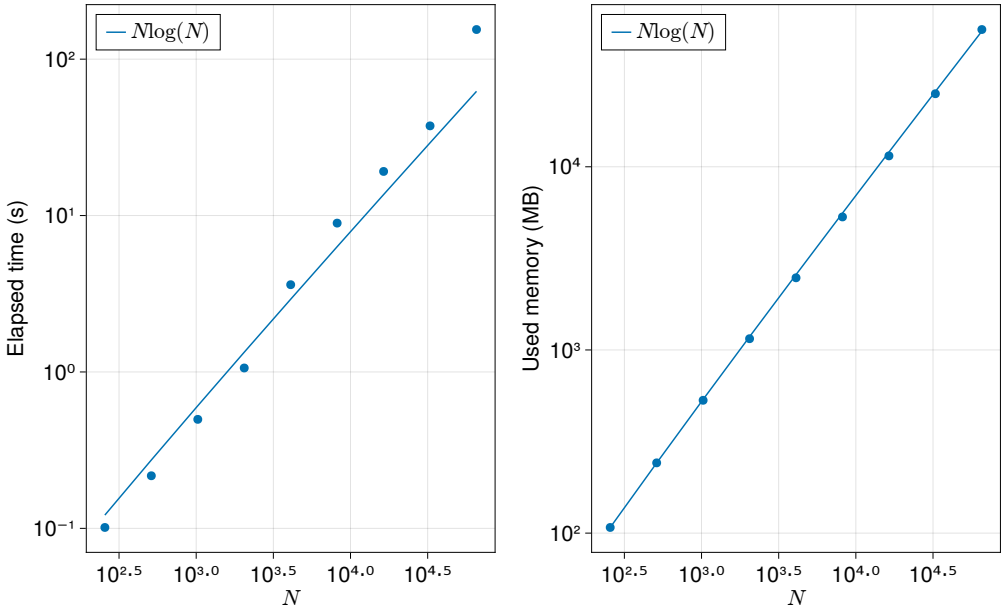

Figure 6.4: Average time and total allocated memory to solve the full Dyson equation for the NQDN junction biased by a constant voltage for a constant simulation length as a function of the number of time steps.

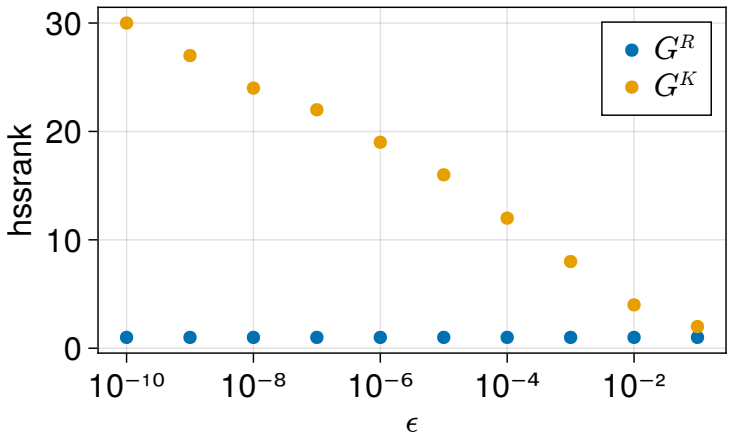

Figure 6.5: Evolution of the HSS rank when varying the accuracy parameter of the compressed matrix. The discretized Retarded Green function can be exactly represented in the HSS format, hence its HSS rank is independent of ϵ_0. While the HSS rank of the kinetic Green function depends on the representation accuracy.

By the way, in the stationary regime, the Fisher-Lee relation 2.65 can be used to evaluate the energy dependent junction transmission from the voltage independent retarded Green function. That is, one can evaluate the whole transmission and thus the IV relation by evaluating once the retarded Green function. While this approach would have been more efficient, the point here was to demonstrate the solver's behaviour.

6.4.1.2 Transition to the adiabatic regime

As our solver deals with general transient regime setups, we can simulate the response of the junction to a voltage ramp $V(t) = V_{\text{amp}}(2t/P - 1)$, where P is the simulation length, applied on the left lead. The right lead and the quantum dot potential are kept to 0. By increasing the simulation length P, thus reducing the voltage ramp slope, we retrieve the static IV characteristics. This is a quite demanding simulation in the sense that we have two very different time scales: the oscillation of the tunnel coupling phase at pulsation $\frac{eV}{\hbar}$ which must be kept larger than the time step, and the slow variation of the applied voltage. Yet, using our method, we can perform the simulation with a small amount of memory and time on a single core of a laptop, while the same calculation by the usual time stepping methods would have been extremely expensive. As we saw earlier that current converges slowly toward the exact value, we enforce order 2 convergence by using the Richardson acceleration, the procedure is applied to the current interpolation. The figure 6.6 shows the simulation output. We keep all the parameters constant, including the timestep size δ_t. In this second simulation, the HSS rank of the Kinetic Green function increases with the simulation

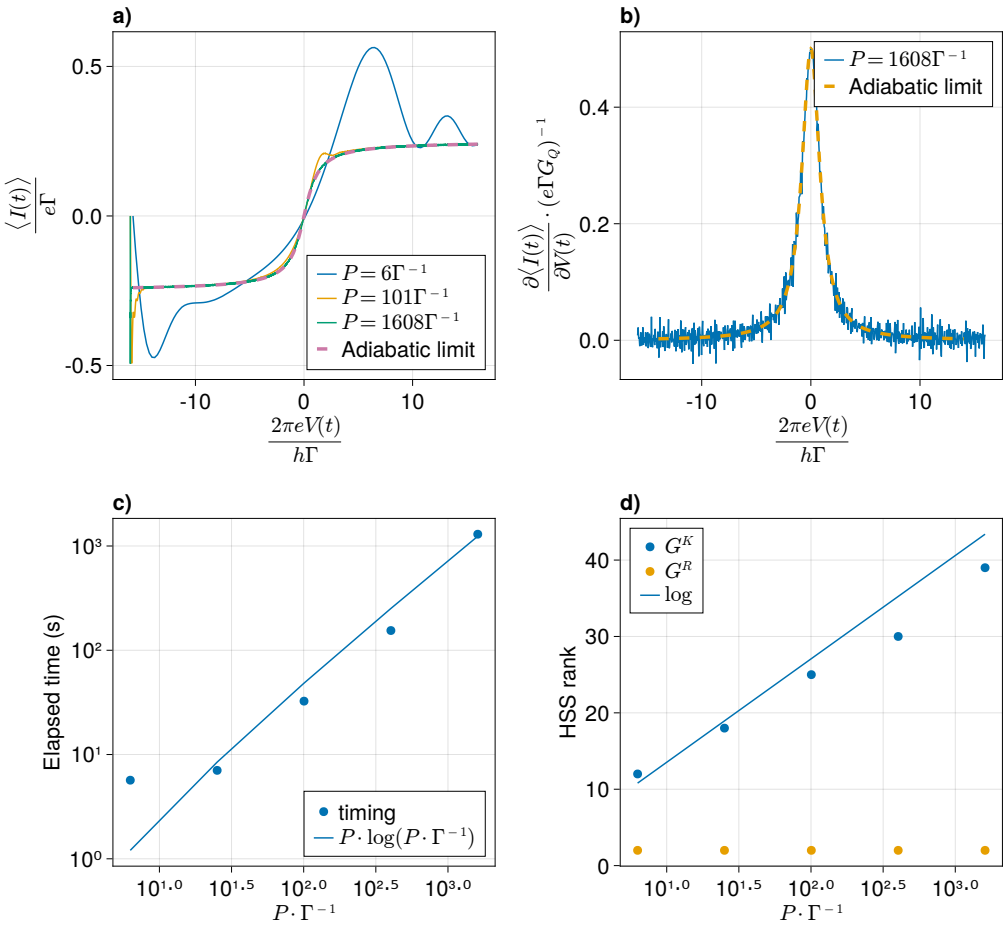

Figure 6.6: *a)* Response to a slow varying voltage ramp. The ramp amplitude is kept constant across the simulations, but the rising time P is changed. *b)* Differential conductance of a quantum dot junction at $\varepsilon = 0$ extracted from the current response of the system to a very slow voltage ramp. The numerical noise originates from finite-difference evaluation of the conductance derivative combined with the relative low accuracy used to evaluate the current. *c)* Wall-clock time for each simulation. *d)* Variation of the HSS rank of both the full retarded Green function and the full kinetic Green function. The HSS rank of G^K seems to increase as $\mathcal{O}(\log P/\Gamma)$.

length. Yet it appears to be slow enough to preserve the overall performance. In figure 6.7, we display the structure of the compressed Green function appearing in this simulation.

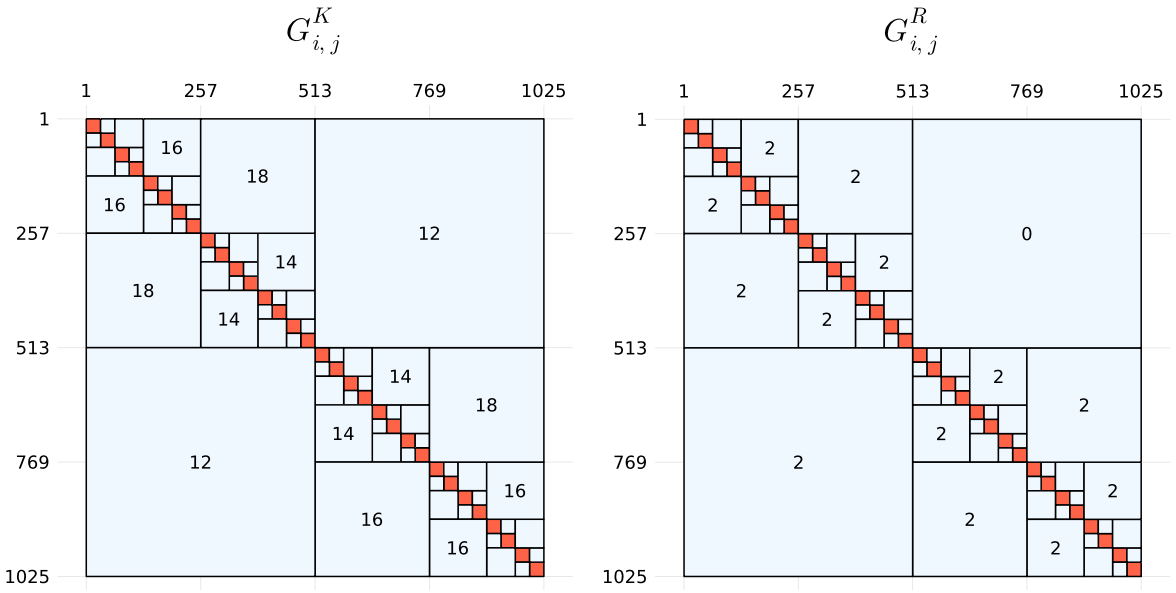

Figure 6.7: Structure of the HSS compressed full retarded and kinetic Green functions for $P = 25 \cdot \Gamma^{-1}$. The numbers indicate the rank of the off-diagonal blocks. The orange blocks are stored as dense matrices. We observe that the compression is much more efficient for G^R than for G^K. Yet, in both cases, the HSS compression reduces dramatically the memory required to store those matrices.

We demonstrate the proper convergence of the solver and its good scaling properties on non-interacting problems. This is a rather easy problem, namely the retarded Green function is extremely regular and quickly cancels. The superconductivity shall put more stress in our method.

6.4.2 Superconducting junction

As for the non-superconducting junction, we consider two different experiments. In the first one, we apply a phase bias $\varphi(t)$ across the junction and observe the resulting supercurrent $\langle I(t)\rangle$. By slowing down the phase variation, we observe the convergence to the adiabatic regime. In the second experiment, we apply a constant voltage bias across the junction in the limit $\Gamma_{L/R} \gg \Delta$. Thus, we effectively replace the quantum dot by a quantum point contact. By observing the DC current in the steady state, we reproduce the results of Ref. [25]. It appears that the solver diverges for long simulation time in presence of superconductivity. Early investigations suggest that the problem does not originate from the HSS approximation. We suspect that the conversion of the free Green functions from the energy domain to the time domain by FFT is inaccurate in the presence of the square root divergence near the gap edge. The simplest way to solve this issue is to set the dissipation rate η/h to a finite value. It appears in the expression of the leads Green functions, see eq. (4.97) and eq. (4.98).

6.4.2.1 Phase biased junction

Here we compare the results of two sets of simulation. First, we evaluate the thermal equilibrium current-phase characteristics $I(\phi)$ by performing a long enough simulations to observe the thermalization. Then we perform a set of simulation where the junction phase follows a linear profile from 0 to 4π: $\phi(t) = 4\pi t/P$ where P is the simulation length. Like previously, by increasing the simulation length, we observe the

convergence toward the adiabatic regime. The time-step δ_t is set to resolve the tunnel coupling timescale h/Γ which is the smallest one: here we set $\Gamma = 12.5\Delta$. The quantum dot junction is described by the effective transmission $T_\pi = 1$ and $T_0 = 0.7$. We set the lead relaxation rate to $\eta = 0.1\Delta$ and the compression accuracy to $5 \cdot 10^{-4}$.

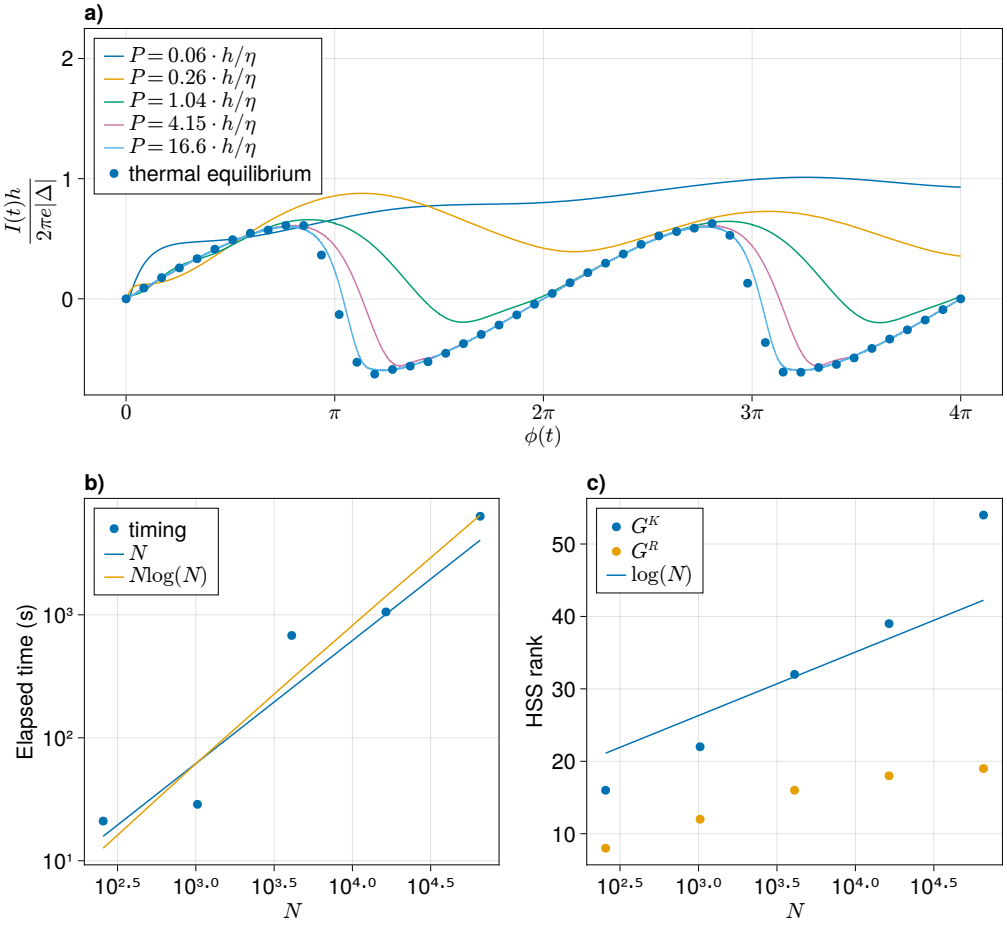

Figure 6.8: *a)* Response to a phase difference ramp. The ramp amplitude is kept constant across the simulation, but the rising time P is changed. *b)* Wall-clock time for each simulation. *c)* Variation of the HSS rank of both the full retarded Green function and the full kinetic Green function. Their HSS ranks increase slowly with N thus preserving the good scaling of the solver.

The results of this experiment appear in fig. 6.8, while fig. 6.9 shows the typical structure of the compressed HSS matrices. We effectively observe the convergence of the out-of-equilibrium response current toward the adiabatic one, as expected. The interesting point is that while storing only one of the kernel in double precision for the longest propagation time, meaning 2^{16} time steps, would require 137 GB of memories without compression and the simulation would need an indecent amount of CPU work, they were run within a few hours on an old laptop fitted with an i5-5200U CPU and 12 GB of RAM. Once again, we demonstrate a quasi-linear scaling of the computational cost with respect to the number of time steps, thus improving drastically over both the classical time stepping method and the results from [30].

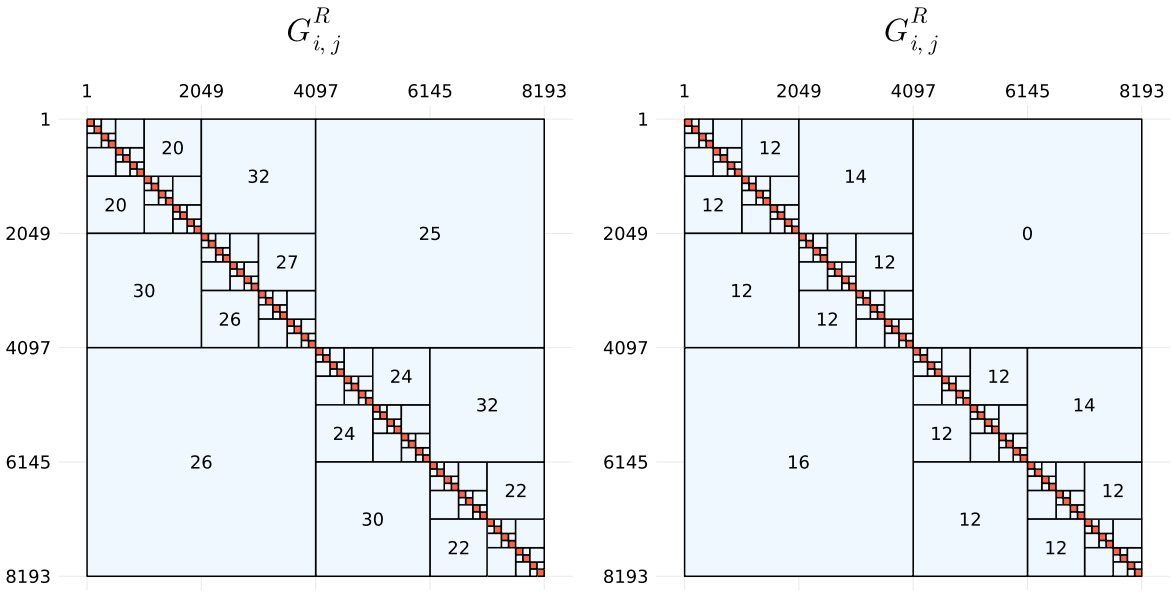

Figure 6.9: Structure of the HSS compressed full retarded and kinetic Green functions for the superconducting junction. The numbers indicate the rank of the off diagonal blocks. Similarly to in the non-superconducting experiment, the compression is more efficient for G^R than for G^K.

6.4.2.2 DC response of a SNS junction

Finally, we investigate the DC response of the superconducting junction in the limit where $\Gamma_{L/R} \gg \Delta$. This regime is extremely demanding for the solver as we have to resolve both the short timescale associated to the tunnel coupling and the oscillation of the phases associated to much larger timescales $\tau_J = \frac{\hbar\pi}{eV}$. A more efficient approach would be to model the quantum dot Green function by a Dirac distribution in time, but once again the point is to benchmark the solver. The simulation of figure 6.10 has *not* been performed on an old laptop, but on a Google cloud instance fitted with 12 CPU cores and 32 GO of RAM. Once the steady state is reached, we extract the DC component by applying a low-pass filter to the average current $\langle I(t)\rangle$. It reproduces the results from [25]. For the comfort of the reader, we reproduce the relevant figure of [25], see fig. 6.11.

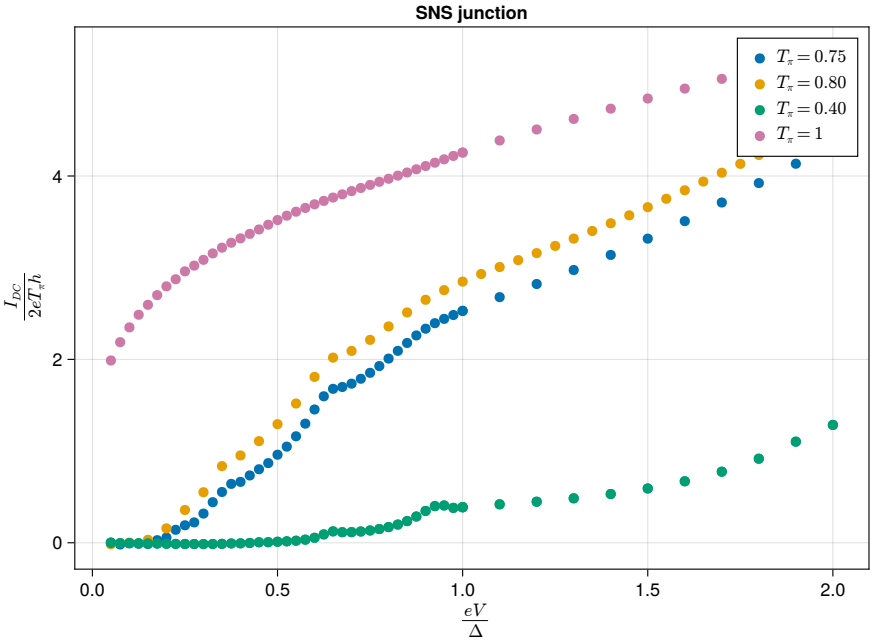

Figure 6.10: Current through a Josephson junction made of two superconducting leads connected to a quantum dot in the limit where $\Gamma_{L/R} \gg \Delta$. We retrieve similar results to [25] despite the effect of the finite relaxation rate η.

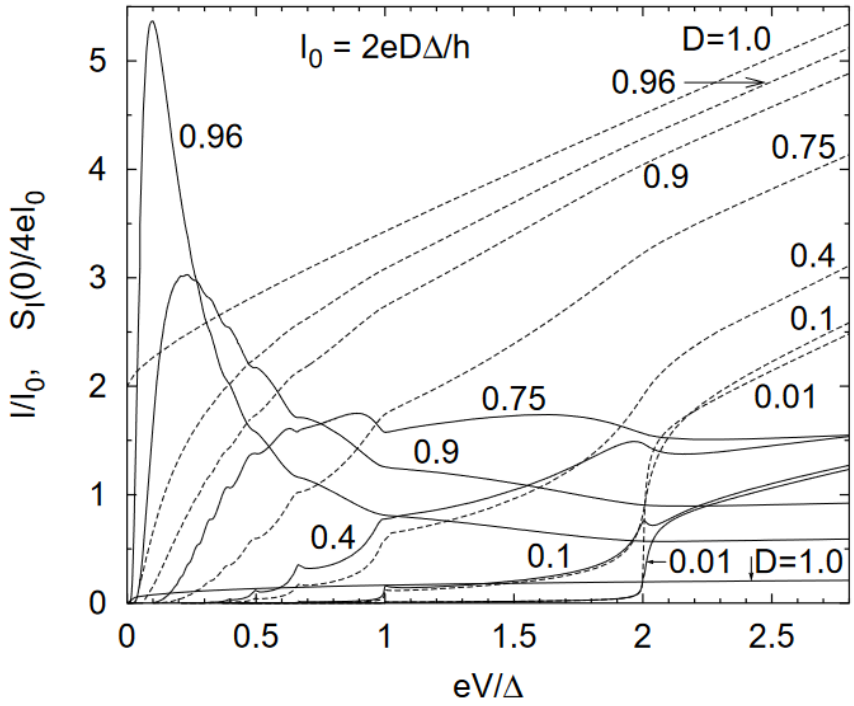

Figure 6.11: *Solid lines*: Zero-temperature spectral density of current fluctuations $S_I(0)$ as a function of the bias voltage V in single-mode junctions with different junction transparencies T_π. *Dashed lines*: the average DC current I_{DC}. *Figure and legend adapted from [25]*

Conclusion

We showed that under certain assumptions, the solution of the retarded Dyson equation can be represented as the set of solution for a linear differential equation. Thus, we provided a method to solve certain problems in linear complexity in both memory and time. This gave us a lesson about a kind of structure that might be exploited to speed up the resolution. Thus, we proposed to tackle the general problem by approximating the different kernels as semi-separable matrices. While this has already been done in [30], we went beyond their result by exploiting the regularities of certain quadrature to recast the Dyson equation discretized by the Nyström method into a compact matrix equation, thus leveraging the fast inversion algorithm of HSS matrices. By benchmarking our code on the metallic and superconducting junction problems, we demonstrated the quasilinear scaling in both memory and time, thus we drastically extended the size of problems that can be solved.

Conclusion and outlook

This PhD project started with the development of a stochastic description of a Josephson junction whose Andreev bound states are detached from the continuum. This phenomenological model predicted the existence of a parameter regime where the Josephson radiation would be fractional. To assess the validity of this result I turned to a microscopic description of the junction in the language of the field theory which required the resolution of the out-of-equilibrium Dyson equation. I developed a new method to solve this equation, which exploits carefully the mathematical structure of the underlying objects, and allows performing long-time simulations.

Chapter 3 gives the full description of our stochastic model. It permits to analyse the role of non-adiabatic transitions between Andreev states in the Josephson radiation of a superconductor quantum-dot superconductor junction. In such a junction, the Andreev bound states are completely detached from the continuum. Within a simplified model of the Andreev states' dynamics, we predicted that this kind of junction may display either conventional radiation or fractional radiation, thus mimicking a topological Josephson junction, depending on its parameters and on the bias voltage. Yet, we neglected the effect of the environment on the junction, and we worked under the *a priori* strong assumption that coherent effects are negligible, while another publication that focused on the average current [24] claims that they induce oscillations in $I_{DC}(V)$ when $\Gamma \sim \Delta$, that is when the ABSs are well detached from the continuum. This corresponds to the parameter regime where sharp features are expected in the finite frequency current noise. Finally, comparison to experimental data is made difficult by the absence of robust estimate of the transition rates. This encouraged the development of a microscopic model.

Chapter 6 introduces our new algorithm to solve the general out-of-equilibrium Dyson equation. It first showed that certain Dyson equations are equivalent to a differential equation. This suggested representing the Green functions and self-energies as semi-separable matrices. This has already been done in reference [30] to reduce the cost of solving the out-of-equilibrium Dyson equation. Yet, we went far beyond their results by harnessing the regularities of certain quadratures to recast the Dyson equation discretized by the Nyström method into a compact matrix equation. This new form of the equation permits to leverage the fast product and inversion algorithms for *hierarchical semi-separable matrices*. This results in a quasilinear complexity $\mathcal{O}(\tau \log(\tau))$ in memory and time with the simulation length τ. By contrast, the already fast method proposed by [30] requires $\mathcal{O}(\tau^2 \log(\tau))$ operations and $\mathcal{O}(\tau \log(\tau))$ bytes of memory. Our new method paves the way towards simulations of long transient regimes.

This PhD work could be first extended by extracting the current correlations of the quantum-dot junction from the full Green function. This only requires to track down the last bugs present in this part of the code and eventual errors in the expanded expression of the observable given by eq. (4.67). A curious mind could also investigate on the connection between the microscopic model exposed in chapter 4 and the stochastic one. Formally deriving the latter from the first could set constraints on the validity of the stochastic approximation. Nevertheless, the more exciting perspectives come from the Dyson equation

solver. Right now it has some artificial limitations: it uses low-order quadratures, and it requires that the self-energy vanishes before the initial time of simulation, this prevents from direct evaluation of the steady state or to use a thermal distribution as initial conditions. While improving those points may require significant amount of work, they shall not present fundamental difficulties. To reduce even further the required computational resources, one may attempt to use an adaptative time step as would do a modern differential equation solver. However, the compact formulation of the discretized Dyson equation is an essential part of the trick , and it relies on the uniform time discretization. We have no clear road to bypass this. Finally, we did not propose any method to evaluate the self-energy in interacting problems. A very elegant approach would be to use our fast kernel product method, see section 6.3.4, to implement a real time *functional renormalization group* (FRG) scheme in the time domain [101, 102]. In the context of Josephson junction, this would permit to include many-body interactions within the junction [22], or the effect of the environment.

APPENDIX A

Gaussian integrals

The Gaussian integrals can be evaluated in all dimension including in the continuous field limit. These integration formulas permit to formally solve all non-interacting problems in the quantum field formalism. The 1D formula is the well known expression

$$\int_{-\infty}^{\infty} \frac{e^{-\frac{a}{2}x^2}}{\sqrt{2\pi}}\,\mathrm{d}x = \frac{1}{\sqrt{a}}, \quad \mathrm{Re}\{a\}>0 \tag{A.1}$$

which can be extended to the following integral

$$\int_{-\infty}^{\infty} \frac{e^{-\frac{a}{2}x^2+bx}}{\sqrt{2\pi}}\,\mathrm{d}x = \frac{1}{\sqrt{a}} e^{\frac{b^2}{2a}}, \quad \mathrm{Re}\{a\}>0 \tag{A.2}$$

Similar expressions exist for the integration over the whole complex plane

$$\int_{-\infty}^{\infty} \mathrm{d}(\bar{z},z) e^{-\bar{z}wz} = \frac{1}{w}, \quad \mathrm{Re}\{w\}>0 \tag{A.3}$$

$$\int_{-\infty}^{\infty} \mathrm{d}(\bar{z},z) e^{-\bar{z}wz+\bar{u}z+\bar{z}v} = \frac{e^{\frac{\bar{u}v}{w}}}{w}, \quad \mathrm{Re}\{w\}>0 \tag{A.4}$$

where the measure is defined by $\int_{-\infty}^{\infty}\mathrm{d}(\bar{z},z) \equiv \iint_{-\infty}^{\infty}\frac{\mathrm{d}x\mathrm{d}y}{\pi}$ with $z = x+iy$. u and v are independent complex numbers. Both the real and complex Gaussian integrals can be generalized to multidimensional cases.

Real case

For a positive definite real symmetric N-dimensional matrix $\mathbf{A}$ and for arbitrary vector $\mathbf{j}$,

$$\int_{x\in\mathbb{R}^N} \frac{e^{-\frac{1}{2}\mathbf{x}^T\mathbf{A}\mathbf{x}}}{\sqrt{2\pi}^N}\,\mathrm{d}\mathbf{x} = \frac{1}{\sqrt{\det\{\mathbf{A}\}}}, \tag{A.5}$$

$$\int_{x\in\mathbb{R}^N} \frac{e^{-\frac{1}{2}\mathbf{x}^T\mathbf{A}\mathbf{x}+\mathbf{j}^T\mathbf{v}}}{\sqrt{2\pi}^N}\,\mathrm{d}\mathbf{x} = \frac{e^{\frac{1}{2}\mathbf{j}^T\mathbf{A}^{-1}\mathbf{j}}}{\sqrt{\det\{\mathbf{A}\}}}, \tag{A.6}$$

Complex case

For a complex N-dimensional matrix $\mathbf{A}$ with positive definite Hermitian part and for arbitrary complex vectors $\mathbf{j}$ and $\mathbf{j}'$,

$$\int \mathrm{d}(\bar{\mathbf{z}},\mathbf{z}) e^{-\mathbf{z}^\dagger\mathbf{A}\mathbf{z}} = \frac{1}{\det\{\mathbf{A}\}}, \tag{A.7}$$

$$\int \mathrm{d}(\bar{\mathbf{z}},\mathbf{z}) e^{-\mathbf{z}^\dagger \mathbf{A}\mathbf{z}+\mathbf{j}^\dagger \mathbf{z}+\mathbf{z}^\dagger \mathbf{j}'} = \frac{e^{\mathbf{j}^\dagger \mathbf{A}^{-1}\mathbf{j}'}}{\det\{\mathbf{A}\}}\,, \tag{A.8}$$

Finally the Gaussian integrals can be extended to Grassmann numbers

Grassmann numbers

For a complex N-dimensional matrix $\mathbf{A}$ with positive definite Hermitian part and for arbitrary vectors $\mathbf{j}$ and $\mathbf{j}'$

$$\int \mathrm{d}(\bar{\psi},\psi) e^{-\psi^\dagger \mathbf{A}\psi} = \det\{\mathbf{A}\}\,, \tag{A.9}$$

$$\int \mathrm{d}(\bar{\psi},\psi) e^{-\psi^\dagger \mathbf{A}\psi+\mathbf{j}^\dagger \psi+\psi^\dagger \mathbf{j}'} = \det\{\mathbf{A}\} e^{\mathbf{j}^\dagger \mathbf{A}^{-1}\mathbf{j}'}\,, \tag{A.10}$$

Acknowledgements

Firstly, I want to thank all the members of the jury: Cristina Bena, Michael Wimmer, Meydi Ferrier, Franck Balestro, Regis Melin and Markus Holzmann. I am grateful for yours comments and questions that shed a new light on my understanding of my own work.

When I arrived in Grenoble in 2018 for an internship on the theory of out-of-equilibrium quantum transport, I knew more about experimental technics than theoretical methods for many-body quantum physics, more about optics than condensed matter physics. Despite this, Julia Meyer and Manuel Houzet gave me a chance as a PhD student. They let me explore my own ideas. This might have been stressful for them, as it was unclear until the end that I was not going towards a dead-end. I am also thankful for the numerous defense rehearsals we have done despite the time constrains.

My four years of PhD would not have been the same without Anthony, Antonio, Thomas B. and Yoan. We spent a lot of time discussing everything and anything. Some of the discussions about our equations led to substantial progress in my work. I must also thank Romuald that was in the lab for a master internship, I asked him so many questions about quantum field theory.

I also want to thank the people that welcomed me in the lab at the very beginning: Benoît, Corentin, Pacôme, Mathieu, Thomas K., Shuo, Pierre, Xavier, Christoph, Mike and Vladimir. As well the ones that pass by: Marjan, Sarath and Eleni. I wish the best for the new PhDs and permanent researchers that arrived in the group since I left. And I shall not forget the swift Marielle who can quickly solve any administrative issue.

When I arrived in Grenoble, I did not know anything about the mountains. Romain A. showed me how to trek. Romain M. lends me some gears for my very first bivouac. Florie has been an excellent ski touring buddy. Christoph gave me many nice tricks about road cycling. I must also thank all the other people with whom I have spent such a nice time in Grenoble or in the surrounding massifs. Martin showed me that one can love knives without being a maniac. Nicolas and its legendary bad-luck. Marion, Simon and Thomas J., we could start the broken knees club. Victor who tries to help everyone, and sometimes forgets himself. And also: Gonzalo, Claire, Estelle, Dorian, Florian V. and Florian B., Anthony A., Chotivut and many more.

I must also thank the friends from Paris that enlighten the long evening of the confinements: Alice, Antoine, Anaïs, Marc, Elise, Benjamin, Vincent, Laura, Solène, Paul, Coraline, Juliette, Quentin, Léonard, Manu, Louis, Théo et Marty.

These four years in Grenoble would not have been as wonderful without Cécile. Together, with our lovely and sneaky little dog Yuzu, we faced our PhDs, the mountains and the confinements. I hope that we will continue to have exciting adventures. Even if we are for now far from the mountains.

Finally, I want to thank my family, who supported me throughout my student years.

Bibliography

1. Arute, F. *et al.* Quantum supremacy using a programmable superconducting processor. *Nature* **574,** 505–510. ISSN: 14764687 (7779 Oct. 2019).
2. Madsen, L. S. *et al.* Quantum computational advantage with a programmable photonic processor. *Nature* **606,** 75–81. ISSN: 14764687 (7912 June 2022).
3. Zhong, H.-S. *et al. Quantum computational advantage using photons* (2020), 1460–1463.
4. Barredo, D., Lienhard, V., de Léséleuc, S., Lahaye, T. & Browaeys, A. Synthetic three-dimensional atomic structures assembled atom by atom. *Nature* **561,** 79–82. ISSN: 14764687 (7721 Sept. 2018).
5. Hendrickx, N. W. *et al.* A four-qubit germanium quantum processor. *Nature* **591,** 580–585. ISSN: 14764687 (7851 Mar. 2021).
6. Philips, S. G. J. *et al.* Universal control of a six-qubit quantum processor in silicon (Feb. 2022).
7. Pirandola, S., Bardhan, B. R., Gehring, T., Weedbrook, C. & Lloyd, S. Advances in Photonic Quantum Sensing (Nov. 2018).
8. Crawford, S. E. *et al. Quantum Sensing for Energy Applications: Review and Perspective* Aug. 2021.
9. Esposito, M., Ranadive, A., Planat, L. & Roch, N. Perspective on traveling wave microwave parametric amplifiers (July 2021).
10. Gisin, N., Ribordy, G., Tittel, W. & Zbinden, H. Quantum cryptography. *Rev. Mod. Phys.* **74,** 145–195 (1 2002).
11. Pirandola, S. *et al.* Advances in quantum cryptography. *Advances in Optics and Photonics* **12,** 1012. ISSN: 19438206 (4 Dec. 2020).
12. Badiane, D. M., Glazman, L. I., Houzet, M. & Meyer, J. S. Ac Josephson effect in topological Josephson junctions. *Comptes Rendus Physique* **14,** 840–856. ISSN: 16310705 (9-10 Nov. 2013).
13. Tinkham, M. *Introduction to Superconductivity* 2nd ed. ISBN: 0486435032 (Dover Publications, June 2004).
14. Yanson, I. K., Svistunov, V. M. & Dmitrenko, I. M. Experimental Observation of the Tunnel Effect for Cooper Pairs with the Emission of Photons. *Sov. Phys. JETP* **21,** 650 (1965).
15. Kitaev, A. Y. Unpaired Majorana fermions in quantum wires. *Phys. Uspekhi* **44,** 131–136. ISSN: 1468-4780 (2001).

16. Kwon, H. J., Sengupta, K. & Yakovenko, V. M. Fractional ac Josephson effect in p- and d-wave superconductors. *Eur. Phys. J. B* **37,** 349–361. ISSN: 14346028 (2004).

17. Deacon, R. S. *et al.* Josephson Radiation from Gapless Andreev Bound States in HgTe-Based Topological Junctions. *Phys. Rev. X* **7,** 21011. ISSN: 2160-3308 (2017).

18. Laroche, D. *et al.* Observation of the 4{π}-periodic Josephson effect in indium arsenide nanowires. *Nat. Commun.* **10,** 245. ISSN: 2041-1723 (2019).

19. Pikulin, D. I. & Nazarov, Y. V. Phenomenology and dynamics of a Majorana Josephson junction. *Phys. Rev. B* **86,** 140504(R). ISSN: 1098-0121 (2012).

20. Martín-Rodero, A. & Levy Yeyati, A. Josephson and Andreev transport through quantum dots. *Adv. Phys.* **60,** 899–958 (2011).

21. Žitko, R. Superconducting quantum dot and the sub-gap states. *Proc. SPIE* **10732** (eds Drouhin, H.-J., Wegrowe, J.-E., Razeghi, M. & Jaffrès, H.) 135–147 (2018).

22. Meden, V. The Anderson–Josephson quantum dot—a theory perspective. *J. Phys. Condens. Matter* **31,** 163001 (2019).

23. Zazunov, A., Plugge, S. & Egger, R. Fermi-Liquid Approach for Superconducting Kondo Problems. *Phys. Rev. Lett.* **121,** 207701. ISSN: 10797114 (2018).

24. Levy Yeyati, A., Martín-Rodero, A. & Vecino, E. Nonequilibrium dynamics of andreev states in the kondo regime. *Phys. Rev. Lett.* **91,** 266802. ISSN: 10797114 (2003).

25. Naveh, Y. & Averin, D. V. Nonequilibrium current noise in mesoscopic disordered superconductornormal-metalsuperconductor junctions. *Physical Review Letters* **82,** 4090–4093. ISSN: 10797114 (20 May 1999).

26. Martin Chauvin. *Les effets Josephson dans les contacts atomiques supraconducteurs* PhD thesis (Paris 6, 2005).

27. Badiane, D. M., Houzet, M. & Meyer, J. S. Nonequilibrium Josephson effect through helical edge states. *Phys. Rev. Lett.* **107,** 177002. ISSN: 00319007 (2011).

28. Rammer, J. *Quantum Field Theory of Non-Equilibrium States* 1–536. ISBN: 9780511618956 (Cambridge University Press, Cambridge, 2007).

29. Altland, A. & Simons, B. D. *Condensed Matter Field Theory* 1–478. ISBN: 9780511789984 (Cambridge University Press, Cambridge, 2010).

30. Kaye, J. & Golez, D. Low rank compression in the numerical solution of the nonequilibrium Dyson equation. *SciPost Physics* **10,** 091. ISSN: 2542-4653 (4 Apr. 2021).

31. David, F. *Théorie statistique des champs Tome 1: Tome 1* ISBN: 9782759821600 (EDP sciences, 2019).

32. Appel, W. *Mathematics for Physics and Physicists* 672. ISBN: 9780691131023 (Princeton University Press, 2007).

33. Van Delft, D. & Kes, P. The discovery of superconductivity. *Physics Today* **63,** 38–43. ISSN: 0031-9228 (2010).

34. Bardeen, J., Cooper, L. N. & Schrieffer, J. R. Theory of Superconductivity. *Physical Review* **108,** 1175–1204. ISSN: 0031-899X (1957).

35. Kopietz, P., Bartosch, L. & Schütz, F. *Introduction to the Functional Renormalization Group* 381–416. ISBN: 978-3-642-05093-0 (Springer Berlin Heidelberg, Berlin, Heidelberg, 2010).

36. Josephson, B. D. Possible new effects in superconductive tunnelling. *Physics letters* **1,** 251–253 (1962).

37. Josephson, B. D. Supercurrents through barriers. *Advances in Physics* **14,** 419–451 (1965).

38. Nazarov, Y. V. & Blanter, Y. M. *Quantum Transport: Introduction to Nanoscience* Cambridge. **5,** 46–47. ISBN: 9780511626906 (Cambridge University Press, New York, 2010).

39. Datta, S. *Electronic Transport in Mesoscopic Systems* ISBN: 9780521416047 (Cambridge University Press, 1995).

40. Groth, C. W., Wimmer, M., Akhmerov, A. R. & Waintal, X. Kwant: a software package for quantum transport. *New Journal of Physics* **16,** 063065. ISSN: 1367-2630 (6 June 2014).

41. Octavio, M., Tinkham, M., Blonder, G. E. & Klapwijk, T. M. Subharmonic energy-gap structure in superconducting constrictions. *Physical Review B* **27,** 6739–6746. ISSN: 0163-1829 (1983).

42. Cron, R. *Les contacts atomiques : un banc d'essai pour la physique mésoscopique* PhD thesis (University Paris 6, 2001).

43. Hata, T. *et al.* Enhanced Shot Noise of Multiple Andreev Reflections in a Carbon Nanotube Quantum Dot in SU(2) and SU(4) Kondo regimes. *Phys. Rev. Lett.* **121,** 247703. ISSN: 10797114 (2018).

44. Averin, D. & Imam, H. T. Supercurrent noise in quantum point contacts. *Phys. Rev. Lett.* **76,** 3814–3817. ISSN: 10797114 (1996).

45. Martín-Rodero, A., Yeyati, A. L. & García-Vidal, F. J. Thermal noise in superconducting quantum point contacts. *Physical Review B* **53,** R8891–R8894. ISSN: 0163-1829 (1996).

46. Beenakker, C. W. J. & van Houten, H. *Resonant Josephson Current Through a Quantum Dot* in *Single-Electron Tunneling and Mesoscopic Devices* (eds Koch, H. & Lübbig, H.) (Springer Berlin Heidelberg, Berlin, Heidelberg, 1992), 175–179. ISBN: 978-3-642-77274-0.

47. Vecino, E., Martín-Rodero, A. & Levy Yeyati, A. Josephson current through a correlated quantum level: Andreev states and π junction behavior. *Phys. Rev. B* **68,** 035105. ISSN: 1550235X (2003).

48. Matsuura, T. The Effects of Impurities on Superconductors with Kondo Effect. *Prog. Theor. Phys.* **57,** 1823–1835. ISSN: 0033-068X (1977).

49. Averin, D. & Bardas, A. ac Josephson effect in a single quantum channel. *Phys. Rev. Lett.* **75,** 1831–1834. ISSN: 00319007 (1995).

50. Houzet, M., Meyer, J. S., Badiane, D. M. & Glazman, L. I. Dynamics of majorana states in a topological josephson junction. *Phys. Rev. Lett.* **111,** 046401. ISSN: 00319007 (2013).

51. Zgirski, M *et al.* Evidence for Long-Lived Quasiparticles Trapped in Superconducting Point Contacts. *Phys. Rev. Lett.* **106,** 257003 (2011).

52. Lamic, B., Meyer, J. S. & Houzet, M. Josephson radiation in a superconductor-quantum dot-superconductor junction. *Physical Review Research* **2,** 33158. ISSN: 0031-899X (3 2020).

53. Yeyati, A. L., Cuevas, J., López-Dávalos, A. & Martín-Rodero, A. Resonant tunneling through a small quantum dot coupled to superconducting leads. *Physical Review B - Condensed Matter and Materials Physics* **55,** R6137–R6140. ISSN: 1550235X (1997).

54. Jacquet, R. *et al.* Theory of nonequilibrium noise in general multiterminal superconducting hybrid devices: Application to multiple Cooper pair resonances. *Physical Review B* **102.** ISSN: 24699969 (2020).

55. Rogovin, D. & Scalapino, D. J. Fluctuation phenomena in tunnel junctions. *Annals of Physics* **86,** 1–90. ISSN: 1096035X (1974).

56. Chevallier, D, Rech, J, Jonckheere, T & Martin, T. Current and noise correlations in a double-dot Cooper-pair beam splitter. *Phys. Rev. B* **83,** 125421 (2011).

57. Clerk, A. A., Devoret, M. H., Girvin, S. M., Marquardt, F. & Schoelkopf, R. J. Introduction to quantum noise, measurement, and amplification. *Reviews of Modern Physics* **82,** 1155–1208. ISSN: 0034-6861. arXiv: 0810.4729 (2010).

58. Cormen, T. H., Leiserson, C. E., Rivest, R. L. & Stein, C. *Introduction to Algorithms, Third Edition* 3rd. ISBN: 0262033844 (The MIT Press, 2009).

59. Press, W. H., Teukolsky, S. A., Vetterling, W. T. & Flannery, B. P. *Numerical Recipes 3rd Edition: The Art of Scientific Computing* 3rd ed. ISBN: 0521880688 (Cambridge University Press, 2007).

60. Alappat, C. *et al.* A Recursive Algebraic Coloring Technique for Hardware-Efficient Symmetric Sparse Matrix-Vector Multiplication. *ACM Trans. Parallel Comput.* **7.** ISSN: 2329-4949 (June 2020).

61. Bollhöfer, M., Schenk, O., Janalik, R., Hamm, S. & Gullapalli, K. State-of-the-Art Sparse Direct Solvers (eds Grama, A. & Sameh, A. H.) 3–33 (2020).

62. Bollhöfer, M., Eftekhari, A., Scheidegger, S. & Schenk, O. Large-scale Sparse Inverse Covariance Matrix Estimation. *SIAM Journal on Scientific Computing* **41,** A380–A401. eprint: https://doi.org/10.1137/17M1147615 (2019).

63. Amestoy, P., Duff, I. S., Koster, J. & L'Excellent, J.-Y. A Fully Asynchronous Multifrontal Solver Using Distributed Dynamic Scheduling. *SIAM Journal on Matrix Analysis and Applications* **23,** 15–41 (2001).

64. Amestoy, P., Buttari, A., L'Excellent, J.-Y. & Mary, T. Performance and Scalability of the Block Low-Rank Multifrontal Factorization on Multicore Architectures. *ACM Transactions on Mathematical Software* **45,** 2:1–2:26 (1 2019).

65. Foster, L. V. & Davis, T. A. Algorithm 933. *ACM Transactions on Mathematical Software* **40,** 1–23. ISSN: 0098-3500 (2013).

66. Pais, M. J., Yeralan, S. N., Davis, T. A. & Kim, N. H. An exact reanalysis algorithm using incremental Cholesky factorization and its application to crack growth modeling. *International Journal for Numerical Methods in Engineering* **91,** 1358–1364. ISSN: 00295981 (2012).

67. Rennich, S. C., Stosic, D. & Davis, T. A. Accelerating sparse Cholesky factorization on GPUs. *Parallel Computing* **59,** 140–150. ISSN: 01678191 (2016).

68. Boyd, J. P. *Chebyshev and Fourier Spectral Methods: Second Revised Edition* Second, 690 (Dover, 2000).

69. Huybrechs, D. Stable high-order quadrature rules with equidistant points. *Journal of Computational and Applied Mathematics* **231,** 933–947. ISSN: 03770427 (2 Sept. 2009).

70. Trefethen, L. N. & Weideman, J. A. C. The Exponentially Convergent Trapezoidal Rule. *SIAM Review* **56,** 385–458. ISSN: 0036-1445 (2014).

71. Fornberg, B. & Reeger, J. A. An improved Gregory-like method for 1-D quadrature. *Numerische Mathematik* **141,** 1–19. ISSN: 0029599X (2019).

72. Dong, X., Zgid, D., Gull, E. & Strand, H. U. Legendre-spectral Dyson equation solver with super-exponential convergence. *Journal of Chemical Physics* **152.** ISSN: 00219606. arXiv: 2001.11603 (2020).

73. Floquet, G. Sur les équations différentielles linéaires à coefficients périodiques. fr. *Annales scientifiques de l'École Normale Supérieure* **2e série, 12,** 47–88 (1883).

74. Honeychurch, T. D. & Kosov, D. S. Full counting statistics for electron transport in periodically driven quantum dots. *Physical Review B* **102,** 1–8. ISSN: 24699969. arXiv: 2008.12652 (2020).

75. Martinez, D. F. FloquetGreen function formalism for harmonically driven Hamiltonians. *Journal of Physics A: Mathematical and General* **36,** 9827–9842. ISSN: 0305-4470 (2003).

76. Brandes, T. Truncation method for Green's functions in time-dependent fields. *Physical Review B* **56,** 1213–1224. ISSN: 0163-1829. arXiv: 9704097 [cond-mat] (1997).

77. Tsuji, N., Oka, T. & Aoki, H. Correlated electron systems periodically driven out of equilibrium: Floquet+DMFT formalism. *Physical Review B - Condensed Matter and Materials Physics* **78,** 1–17. ISSN: 10980121. arXiv: 0808.0379 (2008).

78. Gutleb, T. S. & Olver, S. A Sparse Spectral Method for Volterra Integral Equations Using Orthogonal Polynomials on the Triangle. *SIAM Journal on Numerical Analysis* **58,** 1993–2018. ISSN: 0036-1429 (2020).

79. Gutleb, T. S. A fast sparse spectral method for nonlinear integro-differential Volterra equations with general kernels. *Advances in Computational Mathematics* **47,** 1–26 (2021).

80. John, F., Lasalle, J. P. & Sirovich, L. *Linear Integral Equations* Third. ISBN: 9781461495925 (Springer, 2014).

81. Schüler, M. *et al.* NESSi: The Non-Equilibrium Systems Simulation package. *Computer Physics Communications* **257,** 107484. ISSN: 00104655 (2020).

82. Nedaiasl, K., Bastani, A. F. & Rafiee, A. A product integration method for the approximation of the early exercise boundary in the American option pricing problem. *Mathematical Methods in the Applied Sciences* **42,** 2825–2841. ISSN: 10991476. arXiv: 1710.00161 (2019).

83. Unterreiter, A. Volterra integral equation models for semiconductor devices. *Mathematical Methods in the Applied Sciences* **19,** 425–450. ISSN: 01704214 (1996).

84. Krimer, D. O., Putz, S., Majer, J. & Rotter, S. Non-Markovian dynamics of a single-mode cavity strongly coupled to an inhomogeneously broadened spin ensemble. *Physical Review A* **90,** 043852. ISSN: 1050-2947 (2014).

85. Van Den Bosch, F., Metz, J. A. & Zadoks, J. C. Pandemics of focal plant disease, a model. *Phytopathology* **89,** 495–505. ISSN: 0031949X (1999).

86. Maleknejad, K. & Aghazadeh, N. Numerical solution of Volterra integral equations of the second kind with convolution kernel by using Taylor-series expansion method. *Applied Mathematics and Computation* **161,** 915–922. ISSN: 00963003 (2005).

87. Brunner, H. *Collocation Methods for Volterra Integral and Related Functional Differential Equations* ISBN: 9780521806152 (Cambridge University Press, 2004).

88. Babolian, E. & Masouri, Z. Direct method to solve Volterra integral equation of the first kind using operational matrix with block-pulse functions. *Journal of Computational and Applied Mathematics* **220,** 51–57. ISSN: 03770427 (2008).

89. Talarico, N. W., Maniscalco, S. & Lo Gullo, N. A Scalable Numerical Approach to the Solution of the Dyson Equation for the Non-Equilibrium Single-Particle Green's Function. *Physica Status Solidi (B) Basic Research* **256.** ISSN: 15213951. arXiv: 1809.10111 (2019).

90. Xia, J., Chandrasekaran, S., Gu, M. & Li, X. S. Fast algorithms for hierarchically semiseparable matrices. *Numerical Linear Algebra with Applications* **17,** 953–976. ISSN: 10705325 (2010).

91. Martinsson, P. G. A fast randomized algorithm for computing a hierarchically semiseparable representation of a matrix. *SIAM Journal on Matrix Analysis and Applications* **32,** 1251–1274. ISSN: 08954798 (2011).

92. Chandrasekaran, S, Gu, M & Pals, T. A Fast *U LV* Decomposition Solver for Hierarchically Semiseparable Representations. *SIAM Journal on Matrix Analysis and Applications* **28,** 603–622. ISSN: 0895-4798 (2006).

93. Massei, S., Robol, L. & Kressner, D. Hm-toolbox: Matlab software for hodlr and HSS matrices. *SIAM Journal on Scientific Computing* **42,** C43–C68. ISSN: 10957197. arXiv: 1909.07909 (2020).

94. Jiménez-Pastor, A. & Pillwein, V. A computable extension for D-finite functions: DD-finite functions. *Journal of Symbolic Computation* **94,** 90–104. ISSN: 07477171 (2019).

95. Stanley, R. P. Differentiably Finite Power Series. *European Journal of Combinatorics* **1,** 175–188. ISSN: 01956698 (1980).

96. Vandebril, R., Barel, M. V., Golub, G. & Mastronardi, N. A bibliography on semiseparable matrices. *Calcolo* **42,** 249–270. ISSN: 0008-0624 (2005).

97. Bonev, B. *HssMatrices.jl* 2021.

98. Lamic, B. *Fork HssMatrices.jl* 2022.

99. Guo, L. *et al. STRUMPACK*

100. Dolgov, S. & Savostyanov, D. Parallel cross interpolation for high-precision calculation of high-dimensional integrals. *Computer Physics Communications* **246,** 1–28. ISSN: 00104655. arXiv: 1903.11554 (2020).

101. Gasenzer, T. & Pawlowski, J. M. Towards far-from-equilibrium quantum field dynamics: A functional renormalisation-group approach. *Physics Letters, Section B: Nuclear, Elementary Particle and High-Energy Physics* **670,** 135–140. ISSN: 03702693 (2 2008).

102. Kennes, D. M., Jakobs, S. G., Karrasch, C. & Meden, V. Renormalization group approach to time-dependent transport through correlated quantum dots. *Physical Review B - Condensed Matter and Materials Physics* **85.** ISSN: 10980121 (8 Feb. 2012).